Fragmentation and lateral scattering of 120 and 200 MeV/u ^{4}He ions in water targets

Fragmentierung und laterale Streuung von 120 und 200 MeV/u ^{4}He-Strahlen in Wassertargets
Zur Erlangung des Grades eines Doktors der Naturwissenschaften (Dr. rer. nat.)
vom Fachbereich Physik genehmigte Dissertation von Marta Rovituso aus Caltanissetta, Italien
Tag der Einreichung: 25.April 2016, Tag der Prüfung: 2.Juni 2016
Darmstadt 2016 — D 17

1. Gutachten: Prof. PhD Marco Durante
2. Gutachten: Prof. Dr. Thomas Aumann

TECHNISCHE
UNIVERSITÄT
DARMSTADT

GSI

Fragmentation and lateral scattering of 120 and 200 MeV/u ^{4}He ions in water targets
Fragmentierung und laterale Streuung von 120 und 200 MeV/u ^{4}He-Strahlen in Wassertargets

Vom Fachbereich Physik genehmigte Dissertation von Marta Rovituso aus Caltanissetta, Italien

1. Gutachten: Prof. PhD Marco Durante
2. Gutachten: Prof. Dr. Thomas Aumann

Tag der Einreichung: 25.April 2016
Tag der Prüfung: 2.Juni 2016

Darmstadt 2016— D 17

Abstract

Along with an increased popularity of heavy ions in cancer therapy, ^{4}He ions have regained the interest of the medical community as a compromise between protons and ^{12}C ions. Although 2054 patients have been treated with ^{4}He beams at Lawrence Berkeley Laboratory (LBL) (Berkeley CA, US) between 1975 and 1992, a comprehensive database of biological and physics measurements in the therapeutic energy range is still missing.

One of the first steps necessary for introducing ^{4}He ions in particle therapy, is the development of a dedicated treatment planning system, for which basic physics information such as the characterization of the beam lateral scattering and fragmentation cross sections describing the loss of primary particles and the build up of secondary fragments are required. Examination of data found in the literature reveals a gap in the therapeutic energy range. These measurements are essential for benchmarking not only the new model developed for the in-house treatment planning code TRiP98 (Treatment Planning for Particles) [1], but also for already existing beam algorithms [2, 3] and for Monte Carlo codes like Geant4 [4] and Fluka [5]. The aim of this work is to provide fragmentation cross sections of ^{4}He ions in the therapeutic energy range.

The experimental data presented here were measured at Heidelberg Ion Beam Therapy Center (HIT) (Heidelberg, Germany) using 120 MeV/u and 200 MeV/u ^{4}He beams. The attenuation of 200 MeV/u ^{4}He beam in water was studied together with the build up of the secondary fragments produced by nuclear fragmentation processes. Target thicknesses between 1 and 25 cm H_2O were chosen to investigate nuclear fragmentation also beyond the maximum penetration depth of the ^{4}He ions.

The mixed radiation field produced by the interaction of 120 and 200 ^{4}He ions with water targets (4.28 and 13.96 cm thick, respectively) has also been investigated in this work by measuring double differential cross sections. A combination of energy deposition and Time of Flight (TOF) acquired with a ΔE-E telescope system provided yields and kinetic energy spectra of all particle species emitted between 0° and 23° with respect to the primary beam direction. Coupling the angular distributions and the kinetic energy spectra gave an estimate of the dose contribution from all particles types. A direct measurement of the beam dose profile was performed independently. For this purpose, a two dimensional (2D) Ionization Chamber (IC) array and radiographic films were used to get information not only on the core of the radial dose distribution but also on its halo. The two datasets have been compared and showed consistent results. As a good parametrization of the beam lateral dose profile is a crucial element in a

treatment planning systems, a fit of the measured distribution was performed and compared to the simple Gaussian approach still used by some treatment planning systems.

The gap of experimental data in the energy range between 100 and 300 MeV/u proves the significance of this work not only for therapeutic applications but also for any other applications where the benchmark of Monte Carlo codes in simulating ^{4}He fragmentation is required.

Zusammenfassung

Mit der zunehmenden Verbreitung von Ionenstrahlen in der Krebstherapie ist auch das Interesse speziell für Heliumionenstrahlen gestiegen. ^{4}He-Ionenstrahlen könnten einen guten Kompromiss zwischen Protonen und Kohlenstoffionen darstellen. Obwohl am Lawrence Berkeley Laboratory (USA) in den Jahren von 1975 bis 1992 mehr als 2000 Patienten behandelt wurden, gibt es nach heutigen Gesichtspunkten immer noch keine ausreichende Datenbasis von biologischen und physikalischen Messungen.

Einer der ersten Schritte, um ^{4}He-Ionen wieder in die Partikeltherapie einzuführen, ist die Entwicklung eines geeigneten Bestrahlungsplanungssystems. Dort müssen grundlegende physikalische Basisdaten wie z.B. die Charakterisierung der lateralen Aufstreuung und die Fragmentierungsquerschnitte für die Abschwächung der Primärteilchen und für den Aufbau der sekundären Fragmente implementiert werden. Tatsächlich gibt es in den Literaturdaten für ^{4}He aber eine Lücke, die sich ausgerechnet über den für die Ionenstrahltherapie relevanten Energiebereich erstreckt. Messdaten in diesem Bereich sind jedoch essentiell für ein Benchmarking mit dem Inhaus-entwickelten Bestrahlungsplanungssystem TRiP98 (Treatment Planning for Particles) [1], sowie mit bestehenden Strahltransportmodellen [2, 3] und Monte-Carlo-Programmen wie GEANT4 [4] und FLUKA [5]. Das Hauptziel dieser Arbeit war entsprechend die Messung und Bereitstellung von Fragmentierungsquerschnitten für ^{4}He-Ionen in dem therapeutischen Energiebereich.

Die hier vorgestellten Daten wurden an der HIT-Anlage (Heidelberg) mit 120 MeV/u und 200 MeV/u ^{4}He-Strahlen gemessen. Bei 200 MeV/u wurden Messungen zur Abschwächung des Heliumstrahls in Wasser und zu den entsprechenden Produktionsquerschnitten der Sekundärteilchen durchgeführt. Die Targetdicken wurden zwischen 1 und 25 cm wasseräquivalenter Dicke variiert, um auch Daten hinter dem Bragg-Peak zu erfassen.

Für die Strahlenfelder der Heliumstrahlen nach Durchdringen von Wassertargets mit Dicken von 4,28 und 13,96 cm (für 120 bzw. 200 MeV/u) wurden auch die doppeldifferentiellen Wirkungsquerschnitte gemessen. Dazu wurden über eine kombinierte ΔE-E und time-of-flight-Messung mit einem sogenannten Teleskop die Energiespektren in Abhängigkeit vom Winkel zwischen 0° und 23° (relativ zur Strahlrichtung) erfasst. Durch Kombination der Winkelverteilungen und der Energiespektren konnte eine winkelabhängige Dosisverteilung - separiert nach den Fragmentsorten - berechnet werden. Auch eine direkte Dosismessung des lateralen Strahlprofils wurde durchgeführt. Dazu wurden ein 2D-Ionisationskammer-Array und Röntgenfilme benutzt. Die Dosis wurde nicht nur bei kleinen Winkeln sondern auch im sogenannten Halo-Bereich bis 23° gemessen. Der Vergleich der Dosismessungen zwischen den Einzelteilchenmessungen und

den integralen Messungen zeigt ein gute Übereinstimmung. Verschiedene Kombinationen von mathematischen Funktionen wurden an die gemessenen lateralen Dosisverteilungen angepasst. Es zeigte sich, dass eine einfache Gaußfunktion, die üblicherweise verwendet wird, für eine klinische Bestrahlungsplanung mit Heliumionen ungeeignet ist.

Der klinische Nutzen der vorliegenden Arbeit liegt zum einen darin, dass die Lücke der experimentellen Messdaten zwischen 100 und 300 MeV/u nun gefüllt wurde und zum anderen genaue Daten zum Benchmarking von Monte-Carlo-Programmen bereitgestellt werden konnten.

Contents

Introduction

External beam radiation therapy is one of the key features in modern multi-modal cancer treatments [6]. Around 50% of all patients with localized malignant tumors undergo treatments using ionizing radiation, mostly in combination with tumor resection and/or chemotherapy [6]. High energy photon irradiation represents by far the most used radiation quality in this respect. However, in the past decades the application of accelerated particles, especially protons and carbon ions, in cancer therapy has gained popularity. Of all particle therapy treatments between 1954 and 2014, 86% of the patients have been treated with protons, 11% have been treated with carbon (^{12}C) ions and the remaining 3% have been treated with helium (^{4}He) ions, pions and other ions [7].

The application of particle beams in cancer therapy was first considered in 1946 when Robert R. Wilson published a paper entitled “Radiological use of fast protons” [8]. He presumed potential benefit, originating from the sharp peak in dose deposition at the end of the ion’s maximum range and consequentially started a detailed study on proton therapy. Particle therapy begun in the 1950’s at the Bevelac facility at LBL in the United States of America [9]. However, the concept of fractionated particle therapy started when volumetric Computed Tomography (CT) scans became more and more available, enabling accurate dose determination within a patients body [10].

During the late 1960s, in particular, ^{4}He ions have been introduced at LBL for the treatment of patients with metastatic carcinoma [11]. Starting from 1975, a more systematic usage of ^{4}He ions was implemented in order to study the advantage of improved dose localization [12]. Until 1992, a total of 2487 [7] patients have been treated with ^{4}He-, ^{12}C- and neon (^{20}N) ions in the LBL. Clinical results of the 2054 patients which have been treated with ^{4}He ions were promising in treatments of skull base tumor and uveal melanoma [13, 14, 15, 10]. In 1994 the Heavy Ion Medical Accelerator (HIMAC) started patient treatment using carbon ions at National Institute of Radiological Sciences (NIRS) Chiba (Japan) [16]. At the same time a new technical solution, the scanning technique, which differs significantly from the previous design used at the LBL and HIMAC, was developed almost in parallel at Paul Scherrer Institut (PSI) in Switzerland [17] using protons and GSI Helmholtz Center for Heavy Ion Research (GSI) in Germany [18] using ^{12}C ions.

In the last years ^{4}He ions have been re-discovered as they potentially represent a good compromise between protons and ^{12}C ions under several aspects, especially for the treatments of pediatric patients [19]. These patients are usually treated with protons, rather than photons, to reduce the integral out of field dose, and thereby reduce the risk of inducing secondary cancer in later years. Carbon ions which feature reduced lateral scattering and a pronounced Bragg peak, however, are not used for these cases, due to their large elevated biological effect and the considerable dose contribution of the generated lighter fragments, beyond the targets distal edge. Energy straggling as well as lateral scattering for ^{4}He ions are reduced compared to protons, and are elevated compared to ^{12}C. Hence, particle therapy using ^{4}He beams could offer an improved dose deposition compared to protons while drastically reducing the dose contribution due to lighter fragments and keeping the elevation of the biological effect at a moderate and safe level concerning uncertainties in treatment delivery. Facilities like HIT, Marburg Ion beam Therapy center (MIT) and National Center of Oncological Hadronterapy (CNAO) have the possibility to provide not only protons and ^{12}C ions but also ^{4}He and oxygen (^{16}O) ions which facilitates a revival of helium in cancer therapy.

To enable the use of ^{4}He ions, a new beam model has been developed and implemented into the in-house treatment planning code TRiP98 (Treatment Planning for Particles) [1]. The performance of the new implementation had to be verified against the relevant physical characteristics of ^{4}He ions, such as scattering of the primary beam in tissue-equivalent, energy loss for all participating primary and secondary ions and nuclear cross sections describing the loss of the primary beam particles and the build up of secondary fragments. A detailed literature study concerning total reaction cross sections revealed a “gap” of data in the therapeutic energy range for particle therapy. Total nuclear reaction cross sections for ^{4}He on protons, ^{12}C and ^{16}O were found in low energy range (between 20 and 50 MeV/u) as well as in the high energy range (above 500 MeV/u), only.

The aim of this work was to provide cross sections data of ^{4}He ions in the therapeutic energy range (120 and 200 MeV/u ^{4}He beams) interacting with H_2O target by measuring the attenuation of the primary beam flux, build up of secondary fragments and their kinetic energy spectra. Radial dose distribution were measured for both beam energies in order to get informations not only on the core of the distribution but also on the halo, caused by secondary fragments.

These data have been compared with predictions of the new TRiP98 beam model [1] and they will provide necessary data to improve pencil beam algorithms [2, 3] and benchmark Monte Carlo codes like Geant4 [4] and Fluka [5].

The work is presented in three chapters. Chapter 1 gives an overview of the important physical aspects, relevant in particle therapy. A short biological description is provided and a comparison between protons, ^{4}He- and ^{12}C ions is made. Chapter 2 describes the experimental setup used for the measurements and discusses the data analysis methods. The final results are then presented and evaluated in Chapter 3. The work closes with a conclusion which recapitulates the main findings and work efforts, and gives a brief summary of necessary future steps.

1 Research Background

1.1 Ion beam therapy

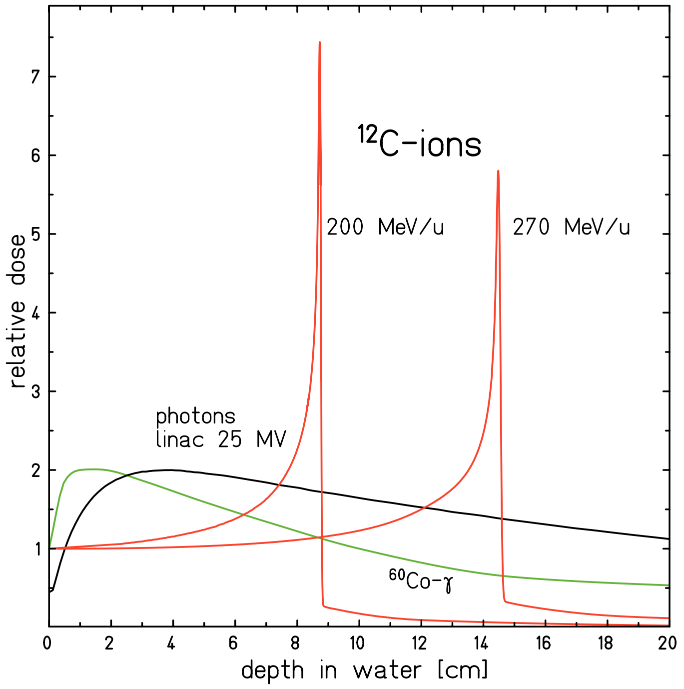

Figure 1.1.: Depth dose profile of electromagnetic radiation (^{60}Co and linear accelerator (linac) spectrum) and Carbon (^{12}C) ions in water. Figure from Schardt et al. [20]

The rational of using ions in radiation therapy lies mainly in their favorable depth-dose profile (Fig. 1.1). While electromagnetic radiation (X-rays and megavolt photon beams) shows an exponential decrease in energy deposition with increasing depth, charged particles exhibit a flat plateau and a distinct peak (Bragg Peak) at the end of their range. The position of this peak can be precisely adjusted to the desired depth in tissue by changing the kinetic energy of the incident ions. This behavior can be exploited for optimizing the conformity of the dose in such a way that ideally the planned target volume receives 100% of the prescribed dose, while the surrounding healthy tissue is maximally spared. In practice, however, dose deposition outside the target is unavoidable and usually limits the target dose due to normal tissue complications. Here ions feature a great reduction of the total out of target dose as the dose deposition in the entrance channel as well the dose deposition exceeding the targets distal boundaries, are smaller compared to photons. Nevertheless dose deposition originating from secondary fragments, produced within the beam-line and the patients body is unavoidable.

1.2 Physics of therapeutic ion beams

When a pencil beam passes through the beam line components and the body's patient two main types of physical interactions have to be considered:

- Electromagnetic interactions, which rule the energy deposition in matter of the primary beam and its lateral spread.
- Nuclear interactions, which cause loss of the primary ions and production of secondary radiation.

One of the most important unit in radiation therapy is the energy deposited in tissue, which is defined by the International Commission on Radiation Units and Measurements (ICRU) with the term $absorbed\ dose$ carrying the unit Gray[Gy] [20]:

$$D = \frac{d\epsilon}{dm}\,[1Gy = 1J/Kg] \tag{1.1}$$

where $d\epsilon$ is the energy deposited by ionizing radiation in the mass element dm.

As reported by Schardt et al. [20], the dose deposited by a parallel and monoenergetic beam is described by the following relation between fluence and dose [20]:

$$D[Gy] = 1.6 \cdot 10^{-9} \cdot F[cm^{-2}] \cdot \frac{dE}{dx}\left[\frac{KeV}{\mu m}\right] \cdot \frac{1}{\rho}\left[\frac{1}{gcm^{-3}}\right] \tag{1.2}$$

where F is the particle fluence, dE/dx the specific energy loss of the particle in the target and ρ the density of the target.

In this section, in particular, the physical aspects concerning the interaction of ^{4}He ions with matter will be presented.

1.2.1 Energy deposition in matter

Charged particles of several hundred MeV which pass through matter are affected by electromagnetic interactions. At these energies, in fact, the ions interact inelastically with shell electrons of the atom and elastically with the atoms nuclei of the medium, resulting in an energy loss dE/dx well described by the Bethe-Bloch formula [21, 22]:

$$\frac{dE}{dx} = \frac{4\pi e^4 Z_t Z_p^2}{m_e v^2}\left[ln\frac{2m_e v^2}{<I>} - ln(1-\beta^2) - \beta^2 - \frac{C}{Z_t} - \frac{\delta}{2}\right] \tag{1.3}$$

where Z_p and Z_t denote the nuclear charge of the projectile and the target respectively, m_e and e are the mass and the charge of the electron and $< I >$ is the mean ionization energy of the target atom or molecule [21, 22]. The formula includes the relativistic corrections by Fano et al. [23] with a dependence from β^2 and two additional terms for the shell (C/Z_t) and the density effect correction ($\delta/2$). The former accounts for the effects which aris when the velocity of the incident particle is comparable or smaller than the orbital velocity of the bound electrons and effects the stopping power up to 6%. The density term corrects for polarization effects in the target. The mean ionization $< I >$, instead, corrects for the quantum mechanical energy levels available for the transfer of energy to the target electrons. For liquid water accurate Bragg curve measurements for protons and different heavier ions show a values of 78 eV [24].

In Fig. 1.2 the Bethe-Bloch formula is solved for different projectile in water. The maximum energy transfer is shifted to higher energies for increasing Nuclear charge (Z). Generally the energy transfer increases with decreasing particle kinetic energy.

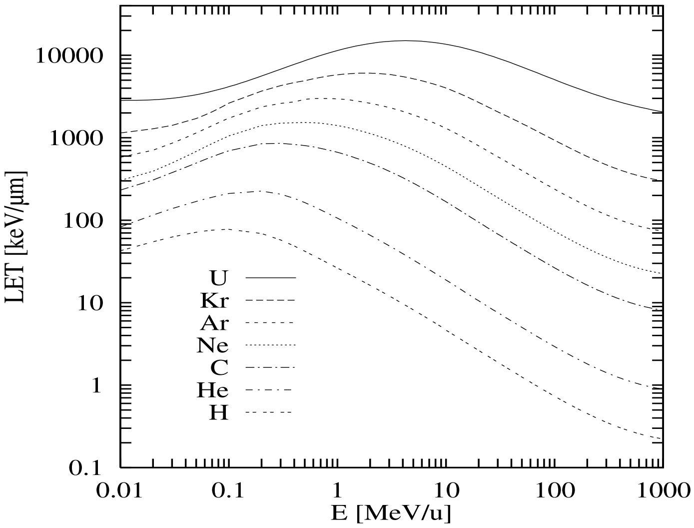

Figure 1.2.: Bethe-Bloch formula solved for different projectile beam in water target. The nomenclature LET stands for linear energy transfer (dE/dx). Courtesy of U. Weber, GSI, Darmstadt.

A further correction to the Bethe-Bloch formula takes the dependence of the projectile effective charge on its velocity into account. At high velocities, the atomic electrons are completely stripped off and the ion effective charge is equal to its atomic charge number Z_p. At lower velocities, the mean charge state decreases due to the interplay of ionization and recombination process and Z_p has to be replaced by the effective charge Z_{eff} described by the Barka's empirical formula [25]:

$$Z_{eff} = Z_p \left[1 - exp\left(-125\beta Z_p^{\frac{2}{3}} \right) \right] \tag{1.4}$$

The maximum energy transfer, corresponding to the Bragg peak, is reached at a projectile velocity of

$$v_p \approx Z_p^{-\frac{2}{3}} v_0 \tag{1.5}$$

where $v_0 = e^2\hbar$ is the Bohr velocity and the corresponding β value is $e^2/\hbar c = 1/137$ that corresponds to the fine-structure constant.

When a charged particle traverses matter, it loses small fractions of its kinetic energy by ionization in the entrance channel. Towards the end of its range, the Bragg peak region, the energy transfer increases drastically before showing a sharp fall-off, indicating the maximum particle range in the respective material. For this reason the position of this peak can be precisely adjusted to the desired depth in tissue by changing the kinetic energy of the incident ions. This behavior (see ^{12}C in Fig. 1.1) is referred to as physical depth-dose distribution of the charged particles.

1.2.2 Mean range and energy straggling

The mean range R for a charged particle is defined as the mean thickness of material traversed before it comes to rest [20]. It can be assumed to be the same as the total path length of the particle trajectory in an absorber given by Eq. 1.6:

$$R(E) = \int_0^E \left(\frac{dE'}{dx} \right)^{-1} dE' \tag{1.6}$$

The range of ions in an absorber medium rescales with A/Z^2 for ions with the same initial kinetic energy, as shown in Fig. 1.3 for protons, ^{12}C, ^{16}O and ^{20}N in water.

According to Eq. 1.3 the energy loss of a single ion plotted as a function of penetration depth would result in a very sharp peak near the stopping point. However, a monoenergetic beam of particles is affected by statistical fluctuations occurring in the energy-loss processes resulting in a broadening of the Bragg peak [26] (see Fig. 1.4).

These fluctuations result in the so called “energy-loss straggling”, well described for thin absorbers by the Vavilov distribution [27]. In the limit of many collisions (or a thick absorber), the Vavilov distribution approaches a Gaussian form [28] with a σ expressed as

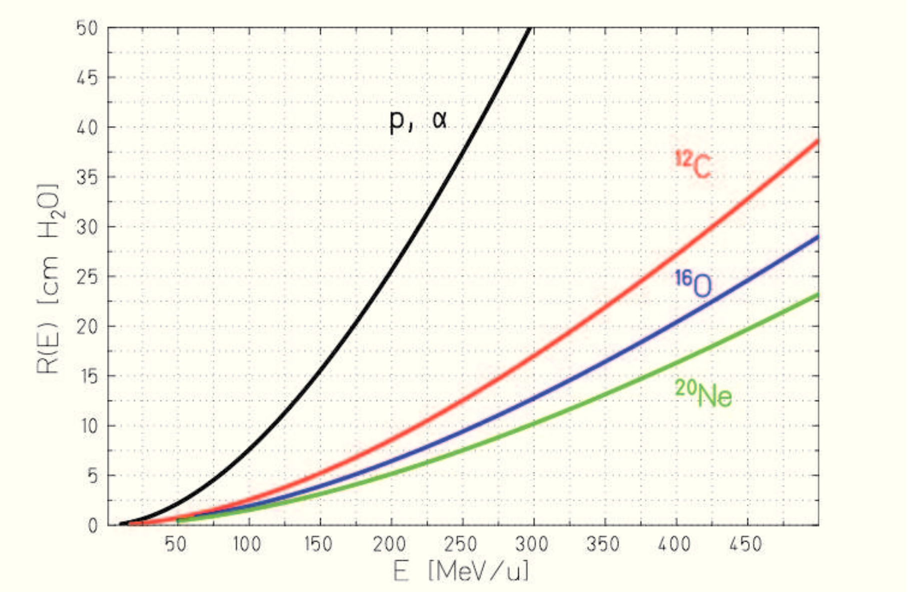

Figure 1.3.: Mean range of several ion species in water. Figure from Schardt et al. [20]

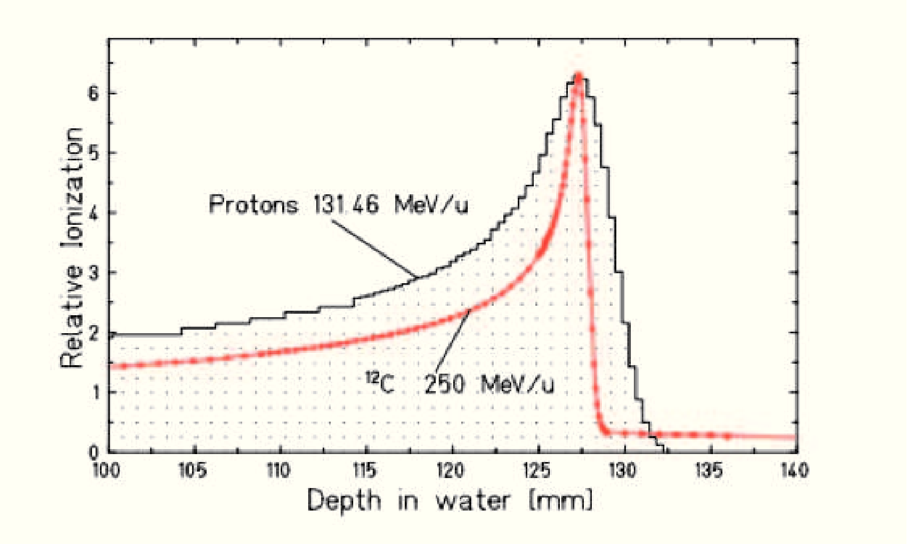

Figure 1.4.: Measured Bragg peaks of protons and ^{12}C ions having the same mean range in water. Figure from Schardt et al. [24].

$$\sigma_E = 4\pi Z_{eff} Z_t e^4 N \Delta x \left[\frac{1-\beta^2/2}{1-\beta^2} \right] \tag{1.7}$$

The variance σ_E^2 is related to σ_R^2 of the energy straggling and the ratio between σ_R^2 and the mean range R is proportional to $1/\sqrt{M}$, with M being the mass of the particle. Due to this dependency the range straggling gets smaller for heavier ions, being maximum for protons, i.e. a factor 3.5 larger when comparing protons and ^{12}C ions [20].

1.2.3 Lateral beam spread

The lateral beam spread of charged particles is caused by elastic Coulomb interaction of the particles with target nuclei. The so called "multiple scattering" theory was described by many scientist between the 1940s and the early 1950s, with similar mathematical approach [29]. In 1948 G. Molière proposed a theory that differed substantially from the others [30]. The Molière approach, in fact, was independent of the exact form of the single scattering law, but contained the atomic screening, the so called "screening angular parameter" coming from the approach of the Thomas-Fermi potential [29].

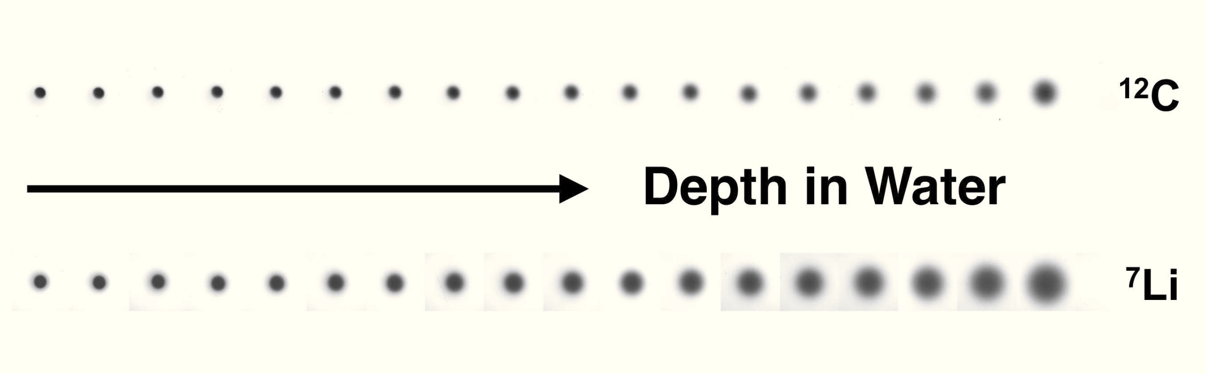

Figure 1.5.: Lateral scattering measurements of 181 MeV/u ^{7}Li and 300 MeV/u ^{12}C ions in water. The beam profiles at increasing water depth were characterized with GaF$_2$ chromic films placed at 1 cm distance from each other. Courtesy of C. La Tessa.

For a small scattering angles the angular distribution given by Molière can be approximated by a Gaussian function with standard deviation given by the Highland approximation [20]

$$\sigma_\theta [rad] = \frac{14.1 MeV}{\beta\ p\ c} Z_p \sqrt{\frac{d}{L_{rad}}} \left[1 + \frac{1}{9} \log\left(\frac{d}{L_{rad}} \right) \right] \tag{1.8}$$

where Z_p and p are the charge and the momentum of the projectile, respectively. The absorber material is characterize by its thickness d and radiation length L_{rad}, which, at equivalent thicknesses, give a larger angular spread for materials containing heavier elements (g/cm^2).

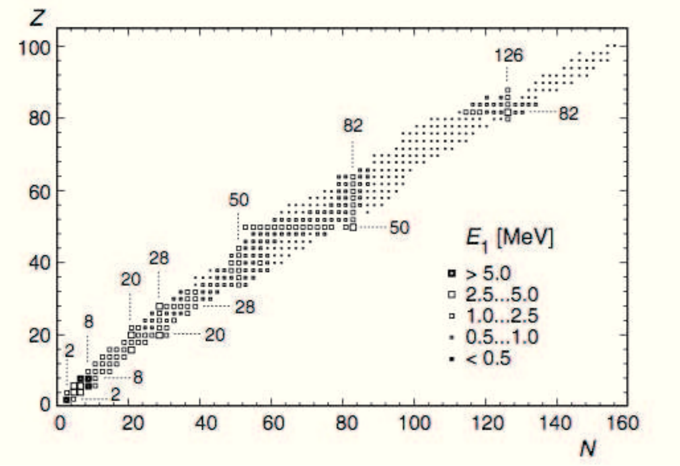

Figure 1.6.: The figure represents the energy E_1 of the first excited state of even-even nuclei. It is particularly high for the nuclei with a magic number of protons and neutrons. E_1 becomes smaller for the "non-magic" number nuclei and it is small for heavier nuclei. The figure was adapted from [31].

Derived from Eq. 1.8 the lateral spread at the same penetration depth is smaller for heavy ions than for protons, coming from the factor $\beta\ p\ c$. The effect of the particles mass can be clearly seen in the example given in Fig. 1.5 showing the measured lateral beam spread of lithium ion beam compared to Carbon ions.

1.2.4 Nuclear interactions

The ^{4}He is a strongly bound system of two neutrons and two protons. It is a double magic number that leads to a high binding energy to extract a proton or a neutron. Moreover, if one adds a neutron or a proton the separation energy would be really small [31]. It is also possible to observe that a high amount of energy is needed to bring one of its nucleons to an excited state (see Fig. 1.6). The energy of its first excited state is, in fact, around 20 MeV, that is much higher compared to all the other nuclei, where the first excited state ranks around only a few MeV. Moreover, the ^{4}He nucleus is a really compact nucleus compared to lighter nuclei. It has a charge radius of 1.67 fm and a mass radius of 1.33 fm, much smaller than the one of deuterons or ^{3}He of 2.1 fm and 1.88 fm for the charge radius, and 1.71 fm and 1.45 fm for the mass radius, respectively [32].

For its unique structure, the development of the nuclear interactions of ^{4}He projectiles is different than the one used for heavy ions, like ^{12}C ions. The abrasion-ablation model used for describing heavy ion nuclear fragmentation is replaced by a one-step process of direct reactions [32]. The direct nuclear processes occur at the surface of the nuclei with a large impact parameter. The projectile may lose energy or have one or more nucleons transferred to or removed from it. The angular distributions are forward peaked as the projectile continues to travel in forward direction [33].

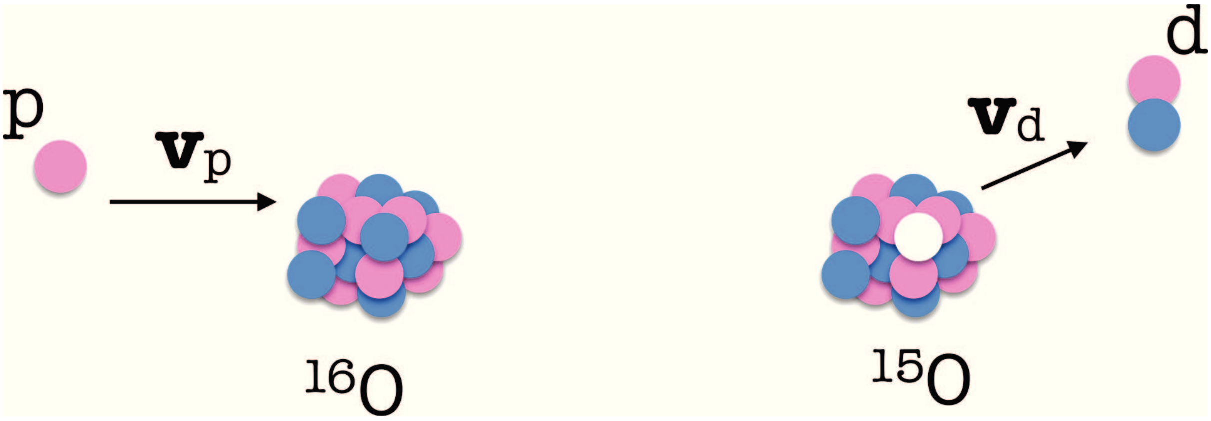

Figure 1.7.: Illustration of the absorption nuclear process of ^{16}O (p,d)^{15}O.

The interaction cross sections of ^{4}He ions at high energies are the elastic channel, nuclear absorption, compound nucleus reactions and fragmentation processes.

The elastic channel and the nuclear absorption

The most common reactions are binary processes, what means: a two-particle collision leads to the formation of two particles. One considers the nuclear reaction :

$$a + A \rightarrow a + A \tag{1.9}$$

where a is a particle with mass m_a and velocity v_a in the laboratory frame, and particle A has mass m_A and it is at rest in the laboratory frame. In the elastic scattering there is no intrinsic change of the states of the particle, the nucleus a does not transfer any energy to the nucleus A of the target into excitation energy and both momentum and kinetic energy of the system are conserved.

All the other processes are inelastic. An example of the latter is the nuclear absorption. In this process a nucleon of the target is "caught" by the projectile. An example of this process is the reaction ^{16}O (p,d)^{15}O, where the proton becomes a deuteron by catching a neutron from the ^{16}O target. A figurative example is shown in Fig. 1.7.

Following the study of Cucinotta et al. [32], the evaluation of the nuclear absorption cross section follows from the elastic scattering amplitude and the optical model theorem. The total cross section can be given by:

$$\sigma_{TOT} = \sigma_{ABS} + \sigma_{EL} \tag{1.10}$$

where σ_{ABS} is the absorption cross section and σ_{EL} is the elastic cross section. The full mathematical development can be found elsewhere [32].

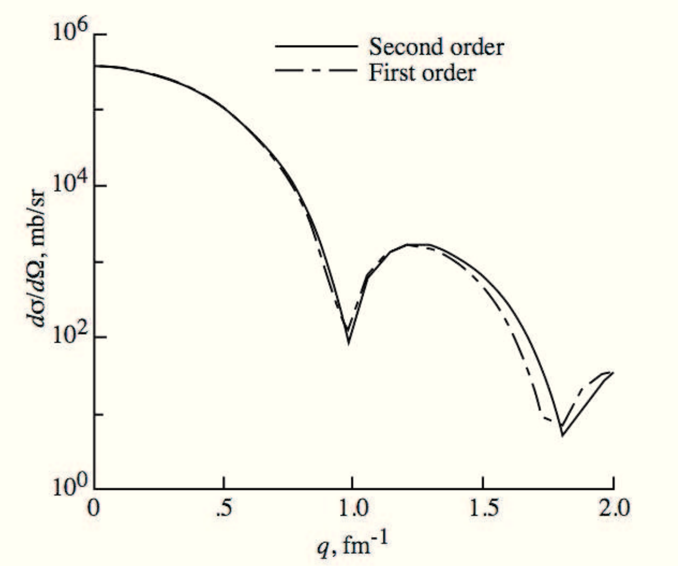

Figure 1.8.: Elastic scattering calculation of ^{4}He on ^{16}O at 1 A GeV. The Figure is taken from Cucinotta et al. [32].

	σ_{TOT} (mb)		σ_{ABS} (mb)	
	Model	Experiment	Model	Experiment
E_{beam}	^{4}He + p			
870	140	143 ± 1.6	101	120±6.2
E_{beam}	^{4}He + ^{12}C			
870	829	790 ± 7	528	542±16

Table 1.1.: Results of nuclear absorption and total cross section from Cucinotta et al. versus the experimental ones. The E_{beam} refers to the beam energy in the laboratory frame and it is expressed in A MeV. The values were taken from Cucinotta et al. [32]

An example of elastic cross section calculation with the Cucinotta approach of ^{4}He on ^{16}O is shown in Fig. 1.8. Table 1.1 shows the calculation of the total and absorption cross section with this model in comparison with the experimental data.

The high separation between the ground state and the first excited state of the ^{4}He nucleus could lead to a significant quasi-elastic cross section. In this reaction the ^{4}He nucleus loses energy and gains momentum transfer without any change in mass and at the same time the target nucleus fragments. In the quasi-elastic process the projectile does not produce any projectile fragment. An illustration is shown in Fig. 1.9.

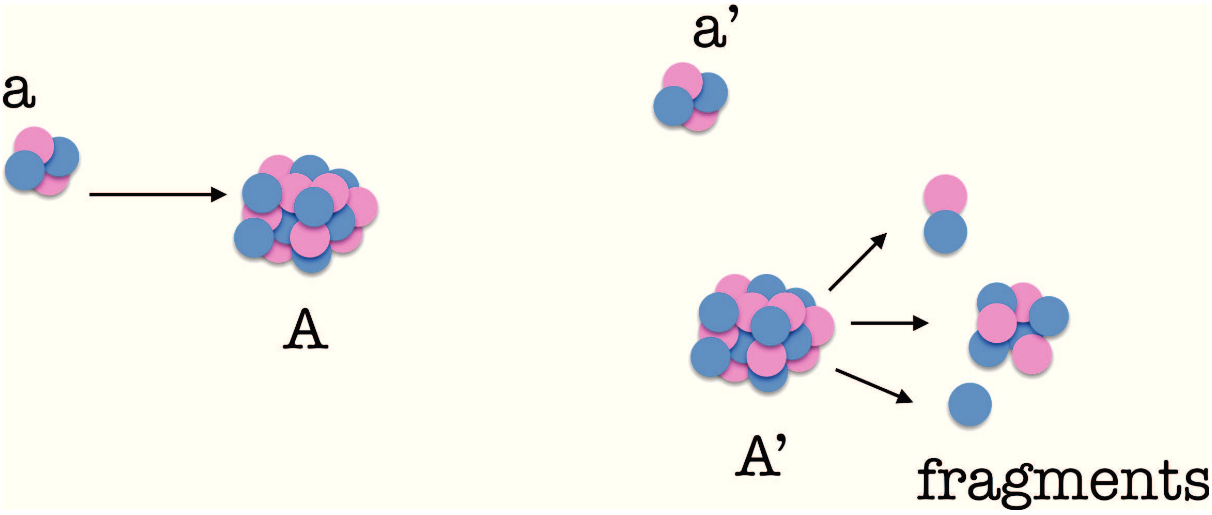

Figure 1.9.: Illustration of the quasi-elastic process of a projectile a on a target A.

The compound nucleus reaction

The compound nucleus reaction can be expressed as:

$$a + A \rightarrow C^* \rightarrow b + B \tag{1.11}$$

where a nucleus a of mass m_a interact with a nucleus A of mass m_A at a certain incident energy. In an easier case, one can consider a as a nucleon and A as a nucleus. The reaction mechanism depends on the incident energy and the probability changes with it. It can happen that the nucleon is absorbed by the target nucleus, the energy is distributed on the constituent nucleons of A and before any of them escape there is the formation of an intermediate excited nucleus $C = a + A$. This nucleus is referred as compound nucleus and this process produces a really excited system. The life time of the compound nucleus is generally short but long enough to be detected with experimental setup. Nevertheless, the compound nucleus will lose its excitation energy through γ emission, or emission of nucleons which will received a certain amount of energy. Following the reaction scheme 1.11 the compound nucleus C can decay emitting the particle b and the formation of the final nucleus B [33]. The cross section of the process 1.11 may be written as the product:

$$\sigma(a, b) = \sigma_C(a) G_C(b) \tag{1.12}$$

where $\sigma_C(a)$ is the formation cross section of the compound nucleus C, the particle a being absorbed by the target A; $G_C(b)$ is the probability of the compound nucleus decay resulting in the emission of the particle b and the formation of the final nucleus B [33]. The compound nucleus C will have an excitation energy equal to $E_C = S + E$, where S is the energy required for separating the absorbed particle from the compound nucleus, and E is the incident projectile energy.

In nature there are many examples of nuclei with a cluster-structure of ^{4}He particles, commonly named as cluster α. One of the most common is the double structure of 2 α in the ^{8}Be. An example of triple cluster α is represented by the ^{12}C. When the projectile energy corresponds to a resonance of the compound system, the cross section of the elastic scattering increases drastically, so that a specific energy resonance peak appears in the excitation energy spectrum.

Light-ion fragmentation processes

The fragments production of the ^{4}He on a target nucleus T can be simpler in respect to heavier ions due to the limited amount of final states which can occur. The reactions are

$$^4He + A \rightarrow \begin{cases} ^3He + n + X \\ t + p + X \\ d + d + X \\ d + n + p + X \\ n + n + p + p + X \end{cases} \tag{1.13}$$

where X is the final target stage [32].

In this approach the fragmentation channels are produced by one-step direct reaction processes, like stripping, pickup and knock out. A stripping reactions can be written as

$$(b + x)_a + A \rightarrow b + (A + x)_B \tag{1.14}$$

where a constituent of the projectile combines with the target nucleus to form the final nucleus state B. The rest of the projectile proceeds with almost the same momentum and original direction. The stripping processes have been studied using (d, p) and (d, n) reactions because the cross section of deuteron-induced reactions are larger than those induced by other charged particle [33].

The reaction of a projectile capturing one nucleon from the target, instead, is called pickup. An example is given in the following reaction

$$p + {}^4He \rightarrow d + {}^3He \tag{1.15}$$

where the projectile proton takes a neutron from the ^{4}He target and it becomes a deuteron leaving a residual ^{3}He nucleus.

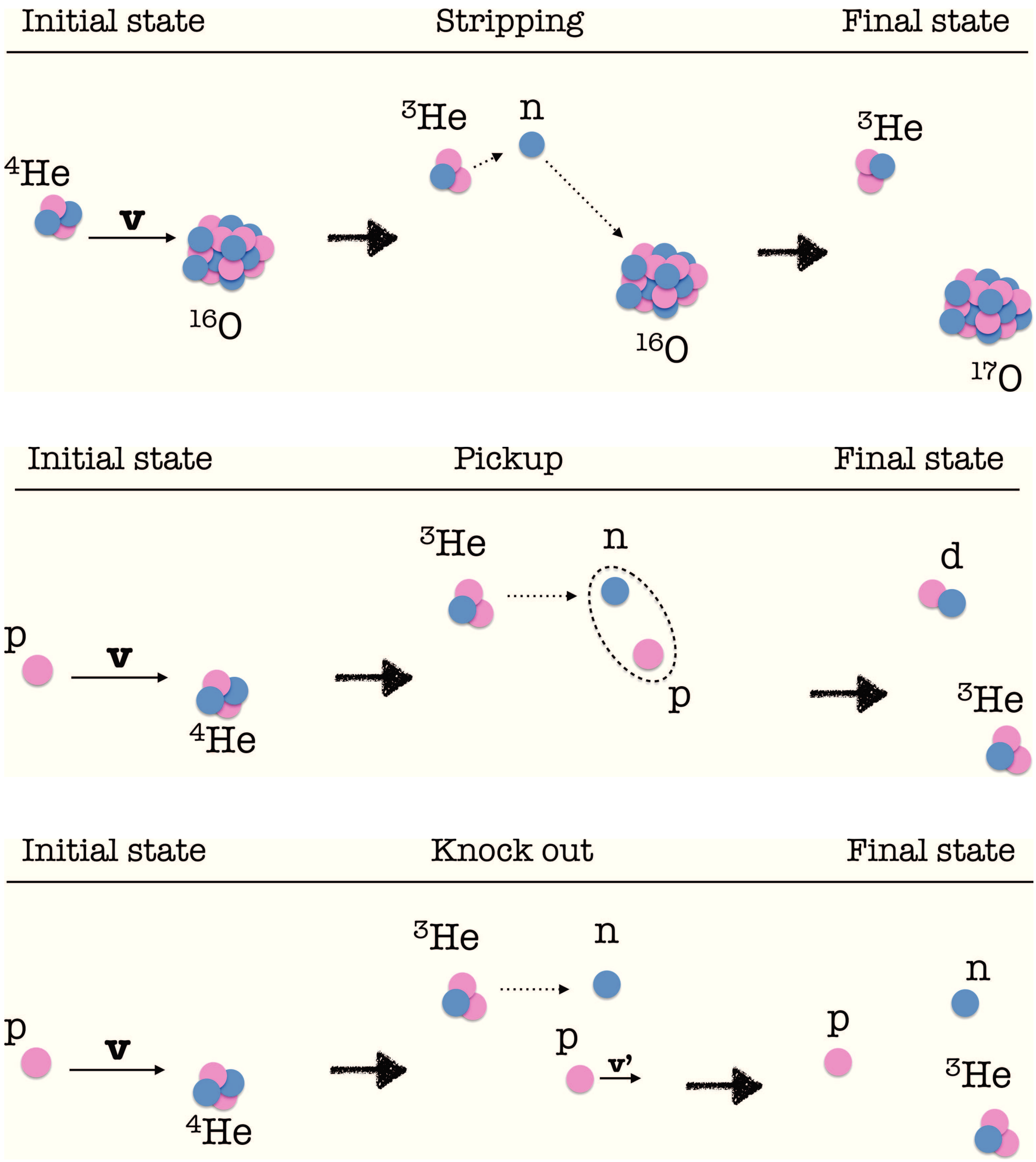

Figure 1.10.: Illustration of the direct process of stripping, pickup and knock out.

In the knock-out reaction a nucleon is knocked out from the projectile and the residual nucleus is left in an excited state. This kind of process may result in more than two final reaction products. An example is given in the following reaction

$$p + {}^4He \rightarrow p + {}^3He^* + n \tag{1.16}$$

An illustration of these mechanisms of reaction are represented in Fig. 1.10.

At sufficiently high energies a complete break up of the ^{4}He nucleus becomes possible. This reaction will lead to the formation of five reaction products. An example of this case is given by the following reaction

$$p + {}^4He \rightarrow p + p + p + n + n \tag{1.17}$$

1.3 Biology of therapeutic ion beams

The goal of curative cancer therapy treatments is to inactivate all malignant tumor cells while keeping the normal tissue complications, caused by unavoidable out of target dose, at an acceptable level.

In order to cure the patient, the tumor cells have to be sterilized so that they cannot transfer their genetic defects to daughter cells. An effective way to sterilize cells is to invoke damage to cells DeoxyriboNucleic Acid (DNA), that contains all the entire set of genetic information. However, the DNA has multiple ways to repair itself and the potential to repair is typical of each cell type. Under the assumption that unrepaired DNA damage leads to cell death, the cell repair potential can be described by the survival probability S after an exposure to the dose D. S is described by a linear-quadratic model (LQ-model) [20]

$$S(D) = exp(-\alpha D - \beta D^2) \tag{1.18}$$

The parameters α and β are cell type specific factors. The repair capacities (i.e. the radio sensitivity) of individual tissue types are reflected in the quadratic term β. Tissue characteristics are commonly reported using the ratio α/β. Hence, cells with a large α/β ratio show small repair capacities and vice versa.

The most common radiation damage induced DNA damages, single strand break, double strand break and loss of a base are shown in Fig 1.11.

The effect of radiation induced damage depends on the deposited dose as well as radiation quality. As illustrated in Fig. 1.2 the deposited dose from ions depends on the stopping power,

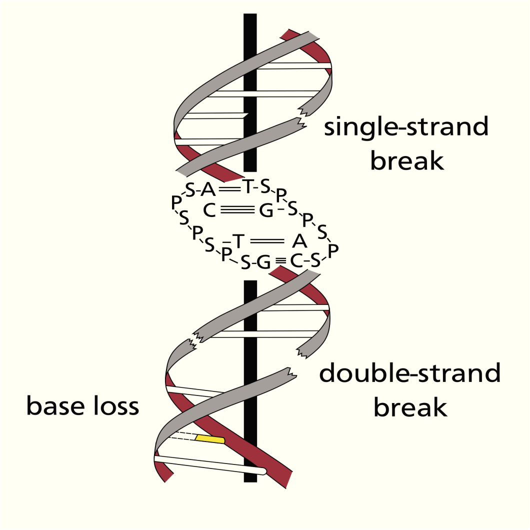

Figure 1.11.: The backbone of a DNA molecule is composed of two phosphate - sugar strands in opposite direction. A series of pairwise compatible nucleo-bases connects to each strand. Between compatible bases hydrogen bounds establish which keep two strands together, giving the typical double helix shape. Radiation induced damage on the DNA are mainly single or double strand breaks. Figure from D. Richter [34].

that is equivalent to the LET in this context. Heavy ions, oppositely to photons, are considered as high-LET radiation because of their dense energy deposition along the track that results in a more complex and compressed DNA lesion (see Fig. 1.3).

Heavy ions interact with the atom or molecule of the medium through Coulomb interaction and production of electrons (δ electrons), which scatter elastically and inelastically in the medium. For electrons with an energy lower than 50 eV inelastic scattering of the electrons causes an excitation of the medium. For higher energies instead, electron scattering causes ionizations that create additional electrons [20]. Moreover, the maximum of the ionization cross section in water is arouns 100 eV, which relates to a mean free path of a few nanometers (nm) [20]. These dense ionization events result in high local damge probability on the DNA through double strand break [20].

One can distinguish between direct DNA damage and indirect DNA damage. The former refers to ionizations on the DNA, induced by the primary ion or its produced secondary electrons. The latter indicates the damage provoked by so called radicals produced from the incident radiation. However, the probability of direct damage induced by ions is higher than the one of indirect damage [20].

One way to describe the elevated effectiveness of dose administered by heavy ions is the concept of the Relative Biological Effectiveness (RBE). The RBE is defined as the ratio of the physically absorbed heavy ion dose to the physically absorbed photon dose (reference radiation) yielding the same biological effect:

$$RBE_{isoeffect} = \frac{D_{ref}}{D_{ion}} \tag{1.19}$$

The RBE is the most relevant quantity in heavy ion therapy for describing cell killing and normal tissue complications [20].

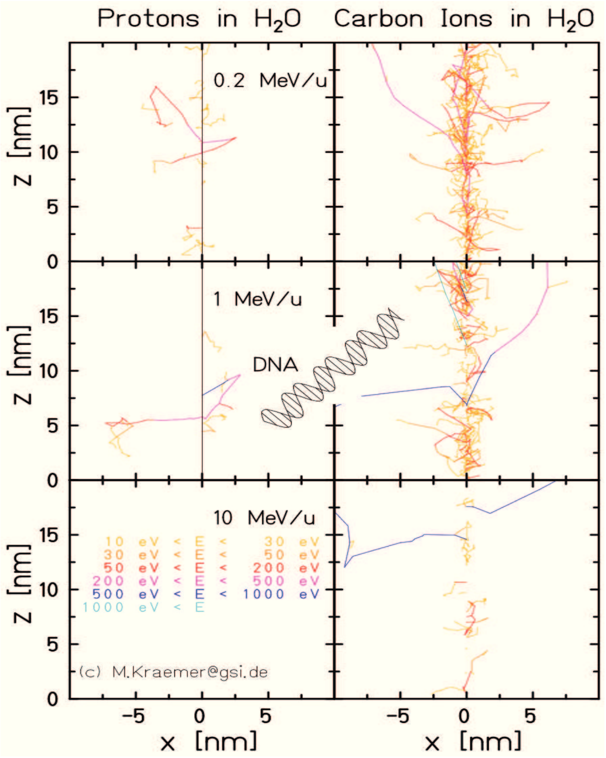

Figure 1.12.: Track structure of protons and ^{12}C ions in water. Simulation of secondary electrons at different energies. The symbolic molecule relates the size of the track to the DNA. Figure courtesy of M. Krämer GSI, Darmstadt, Germany

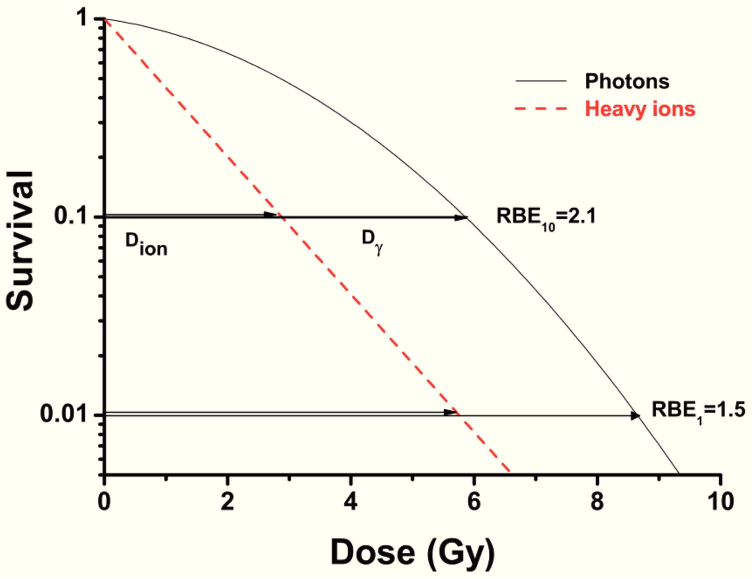

Figure 1.13.: Illustration of two cell survival curves after photon and ion irradiation. The higher effect of ion radiation is expressed as the RBE, which, amongst others, depends on the absolute dose level and refers to the same end point (iso-effect). Figure from Schardt et al. [20].

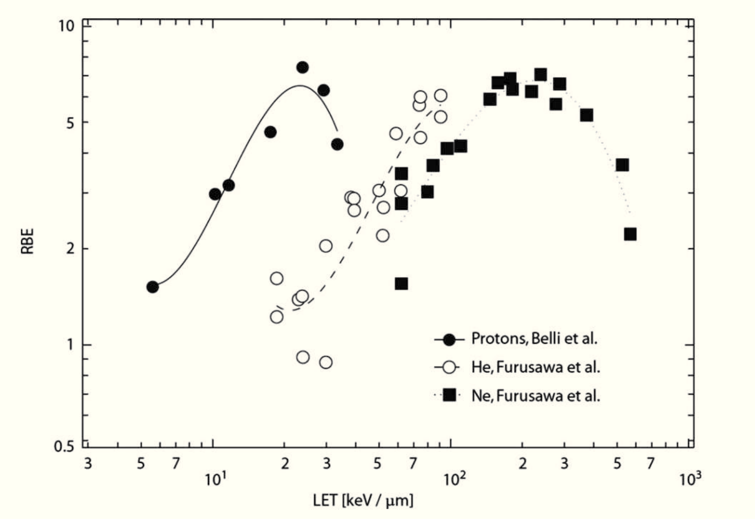

Figure 1.14.: Dependence of the RBE on LET for protons, Carbon and neon ions. It presents a compilation of different cell survival experiments with V79 hamster cell, commonly used in radiobiology laboratory. Figure and explanation are taken from Schardt et al. [20].

In Fig. 1.13 an illustration of the determination of the RBE by typical cell survival curves for photons and heavy ions is shown. To get the same cell survival the dose contribution required from the ions is lower than the one from photons, what translates to a higher cell killing for ions respect to photons for the same physical dose.

The RBE depends on the cell type and the particle type. Fig.1.14 illustrates the dependence of the RBE on the LET for different ion types. The RBE increases for increasing LET up to a maximum which is specific for the individual particle type. For particles with high LETs the ionization density is higher, and hence they induce more severe damage, due to their increased RBE [20]. However, at certain LET values the dose deposition is so high that the RBE decreases due to hit-statistics and the cell survival probability is reduced. The additional LET is then wasted and no difference in the RBE is expected. Looking at Fig.1.14 one can also observe that in the region before the RBE maximum, for the same LET protons have an higher RBE than Helium ions. This is because for this LET Helium ions are faster than the protons with a broader track that reduces the ionization density within the track core. Therefore, at the same LET the cell killing of Helium is lower than for protons.

1.4 Comparison of protons, ^{4}He and ^{12}C ions

Each ion type offers different physical and biological advantages and draw backs for therapy applications [35]. Protons and ^{12}C ions are the most used radiation in therapy applications, but the interest in using ^{4}He ions is growing. The ^{4}He ions seem, in fact, a good compromise between p and ^{12}C ions.

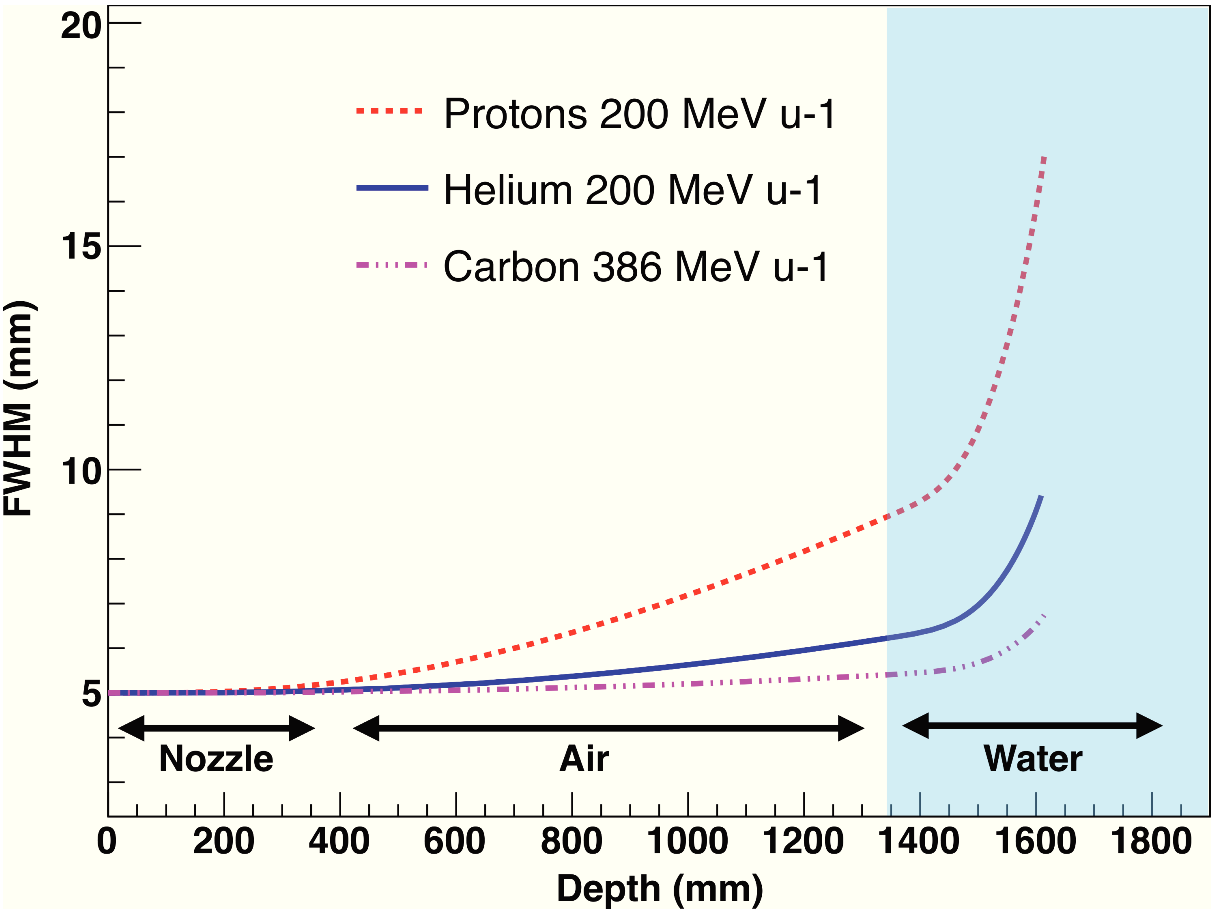

Figure 1.15.: Calculated spread-out of pencil beams for p, He, C from a nozzle geometry compatible with the ion beam therapy setup at GSI [20] and with the ion-beam facilities of University Clinics of Marburg and Heidelberg. A parallel beam enters the water absorber (blue area) at ca. 1 m distance from the nozzle exit has been simulated.

From the physical point of view the energy straggling for Helium ions is less than for protons, even though the width of the Bragg peak is larger than for Carbon ions. A pencil beam that passes through the exit window, a stack of beam monitoring devices and the patient's body is broadened by multiple scattering that is lower for Helium ions with respect to protons as shown in Fig. 1.15. At low energies the multiple scattering in the beam line elements is dominant because a small angular spread causes a large beam broadening due to the large distance between the nozzle and the patient. This effect is critical for protons. The factor of 4 in the mass of ^{4}He reduces this effect. Also ^{4}He beams when compared to ^{12}C beams show a reduced fragmentation tail due to the more limited fragment production, as shown in Fig. 1.16. From the biological point of view it has been shown by Grün et al. [35] that Helium ions have an RBE in the Bragg peak region in between protons and Carbon ions, higher in respect to the former and lower in respect to the latter for the same beam energy. Moreover, a planning study on pediatric patients from Knäusl et al. [19] showed the potential to reduce the volume of irradiated normal tissue without additional dose coming from the fragmentation tail when using ^{4}He instead of protons.

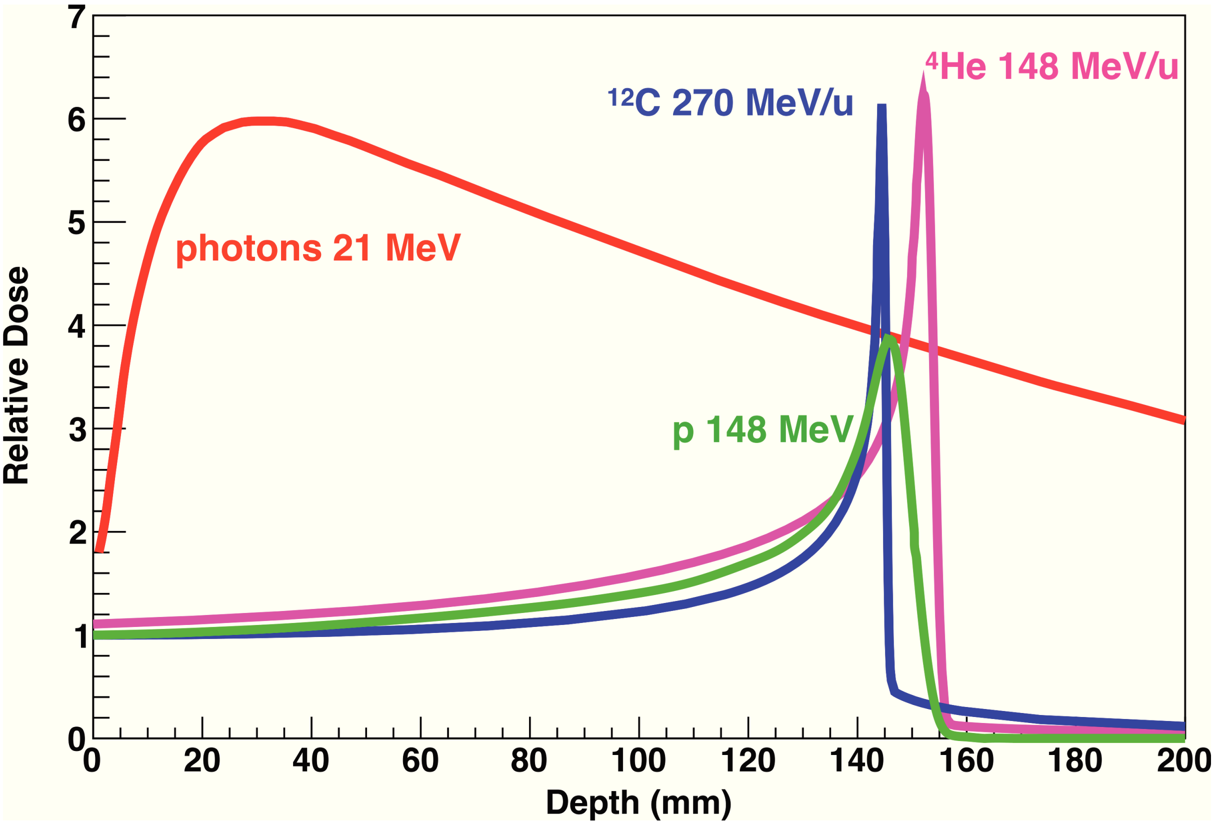

Figure 1.16.: Depth dose profile of photons, protons, ^{4}He and ^{12}C ions in water calculated with TRiP98. Courtesy of M. Krämer and E. Scifoni.

The reduced lateral beam spread, the more pronounced Bragg peak and a steeper dose fall-off behind the Bragg peak are indications for the achievement of a better conformity of the dose distribution and a better sparing of the healthy tissue compared to protons [19].

2 Material and Methods

2.1 Accelerator facility at HIT

All experiments were performed at the experimental beam line of HIT, Germany. The facility was designed to support the raster scanning dose delivery method by producing light ion pencil-beams with energies that allow the treatment of deep-seated tumors [36].

The layout of the accelerator facility is shown in Fig. 2.1. Protons, ^{4}He, ^{12}C and ^{16}O beams are produced with two ion sources and injected either in a compact linac for accelerating protons between $\sim$50 and 220 MeV/u or in a synchrotron capable to accelerate ^{4}He ions from $\sim$50 to 220 MeV/u and ^{12}C and ^{16}O between $\sim$80 and 430 MeV/u .

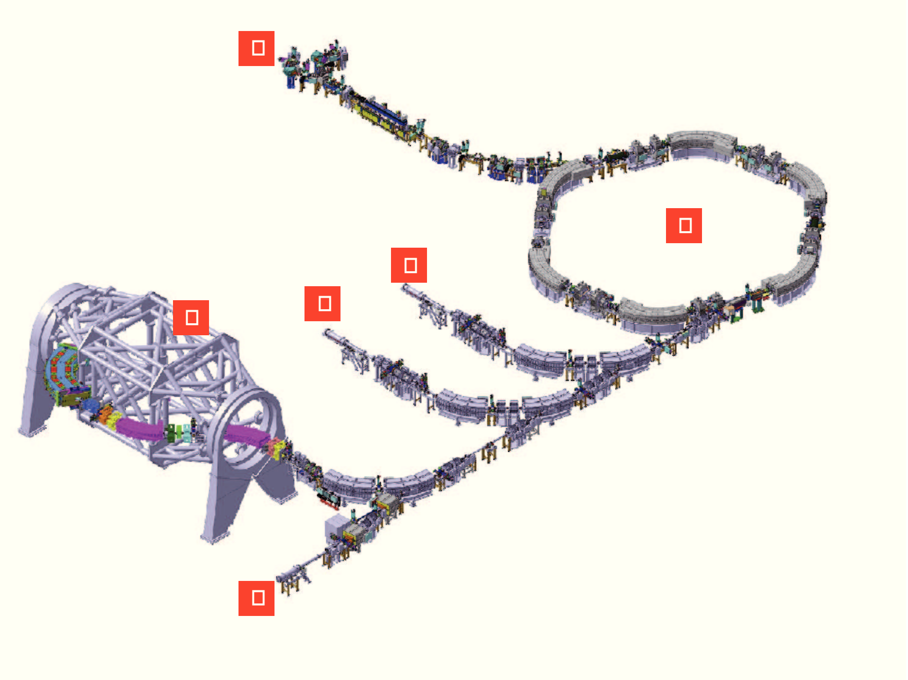

Figure 2.1.: Layout of the HIT accelerator facility. (1) Ions sources, where protons, ^{4}He, ^{12}C and ^{16}O are produced from three different gases. (2) Synchrotron accelerator of 65 m circumference. (3) Fix treatment rooms. (4) Gantry (a rotating beam delivery system that allows the irradiation of the patient from different angles) (5) Fix line for Quality Assurance (QA) and research experiments. The picture was adapted from [37].

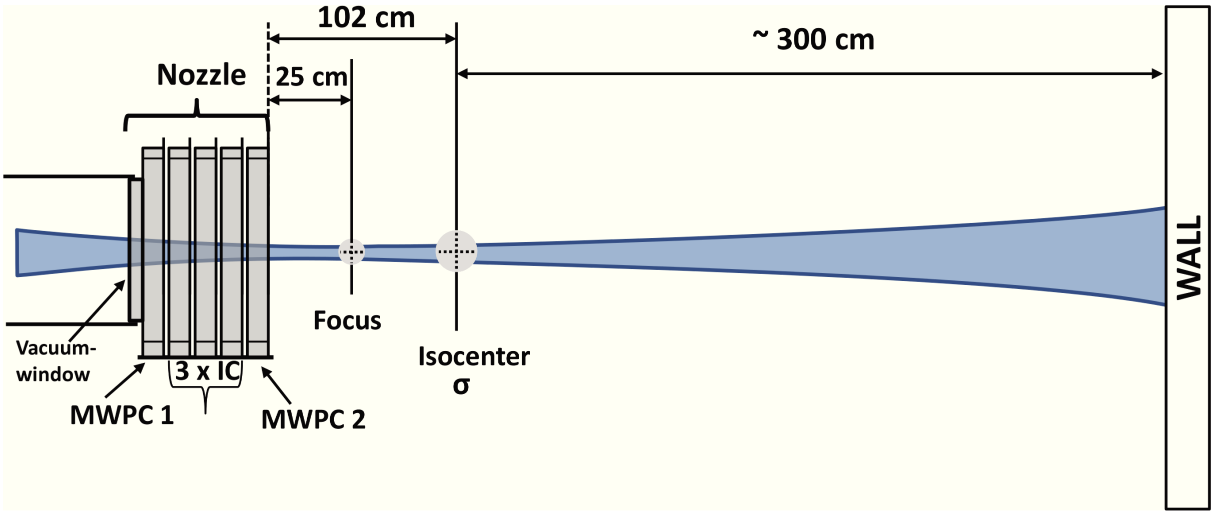

Figure 2.2.: Scheme of the nozzle in the experimental room (QA cave) at HIT. The vacuum exit window is composed of 2 Mylar foils each 100 μm thick and a 0.012 g/cm^2 Kevlar layer. The two Multi Wire Proportional Chamber (MWPC) and the three Ionization Chamber (IC) have a thickness of 4 cm each. The beam envelope is shown in blue. The focus point given by the two quadrupole magnets placed at ∼10 m upstream of the exit window was found to be approximately at 25 cm from the last **MWCP!**. The figure is not to scale.

2.2 Beam characterization of the QA-cave

For the experiments, 120 and 200 MeV/u ^{4}He beams were delivered in the experimental room (QA-cave) at HIT. The experimental beam line is equipped with a therapeutic beam monitoring nozzle, schematically represented in Fig. 2.2. The nozzle is composed of a vacuum exit window and 5 monitoring chambers, with a total Water Equivalent Path Length (WEPL) of 1.8 mm.

The beam profiles at both energies were measured in order to acquire information on the beam focus, ion optics, scattering in air and beam alignment with respect to the fixed laser system. The envelopes were measured with radiographic EDR2 films, which are frequently used for X-rays dose measurements (a technical description can be found in Appendix A.1). They were placed at five different distances from the nozzle perpendicularly to the beam (Fig. 2.3) .

The films irradiations were performed with a raster scanning plan that included information about the x and y coordinates of each beam spot and the corresponding number of particles delivered. Eight irradiation fields of 1x1 cm^2 area were scanned with different fluences for the calibration procedure. A frame and a beam spot were also drawn on the same films to extract information on the vertical and horizontal profiles. An example of the irradiated film after developing is shown in Fig. 2.4.

The films measurements included three steps: developing, scanning and analysis.

The processing was done immediately after irradiation, in a red-light chamber with the developing machine provided at the HIT facility. Afterwards, the films were scanned with the Vidar

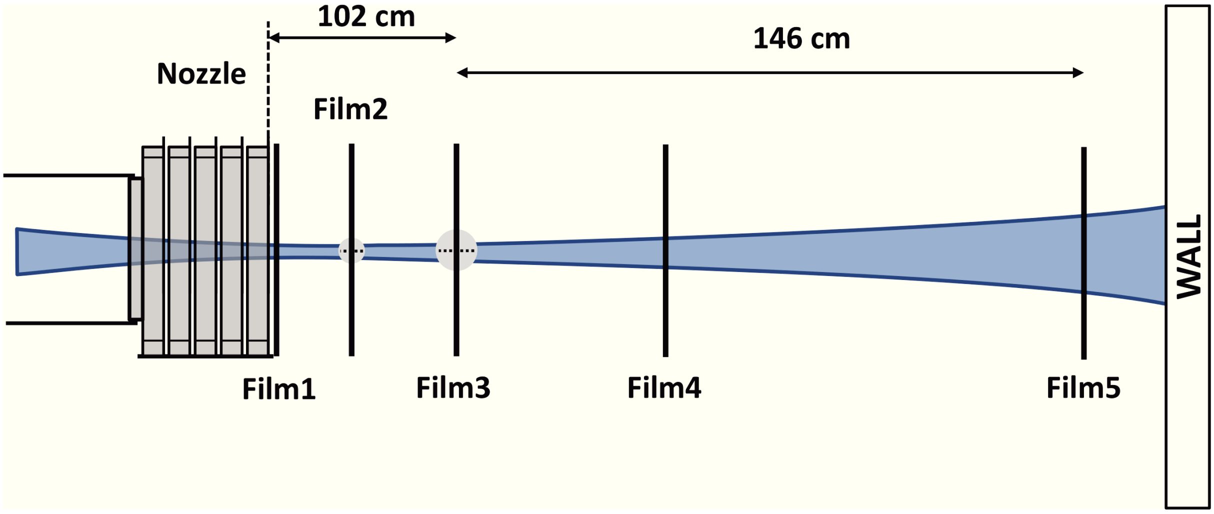

Figure 2.3.: Scheme of the experimental setup for the beam envelope measurements. The center of each film was aligned using the cave laser system and marked before and after its development process.

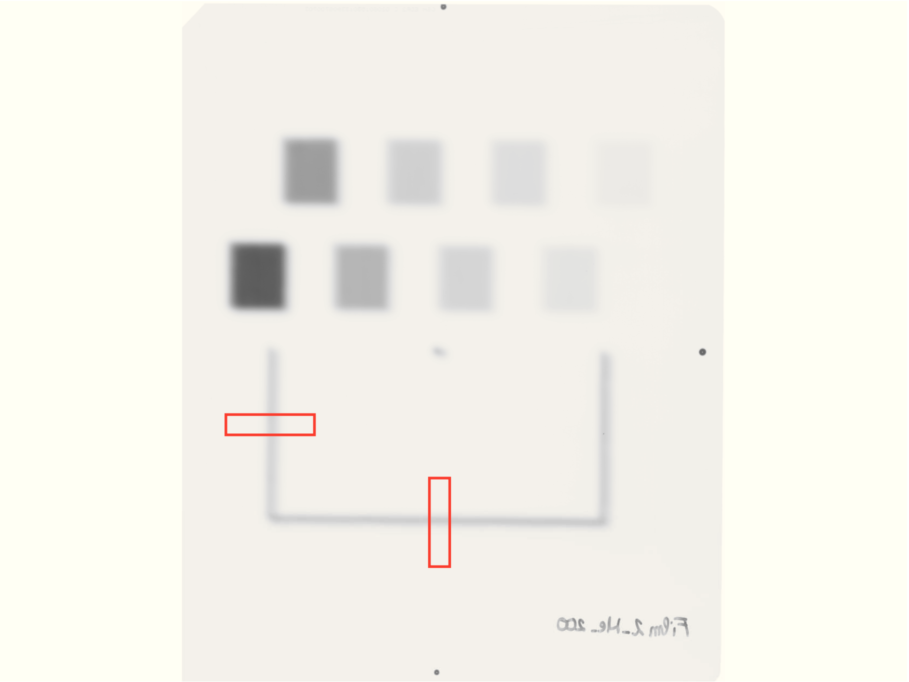

Figure 2.4.: Result of an irradiated film including the calibration fields, a frame and a beam spot. The red bars indicate the section used to analyze the vertical and horizontal profile.

Film Scanner DosimetryPro Advantage pro scanner, using a 150 dpi resolution, a 16 bit depth and a logarithmic translation table.

The analysis of every film was performed with the program ImageJ [38]. The analysis included the calibration procedure and the extraction of the vertical and horizontal beam profile. In the former, the measured gray value and the correspondent fluence from the raster scanning plan were correlated for each field. All fluence values were previously corrected for the beam divergence from the scanner magnets as follow:

$$F_{Corr} = F_{in} \cdot \frac{d_{scanner}}{d_0} \tag{2.1}$$

where $d_{scanner}$ and d_0 are the distances from the last focusing quadrupole to the vacuum exit window and to the isocenter, respectively. The calibration curve is shown in Fig. 2.5.

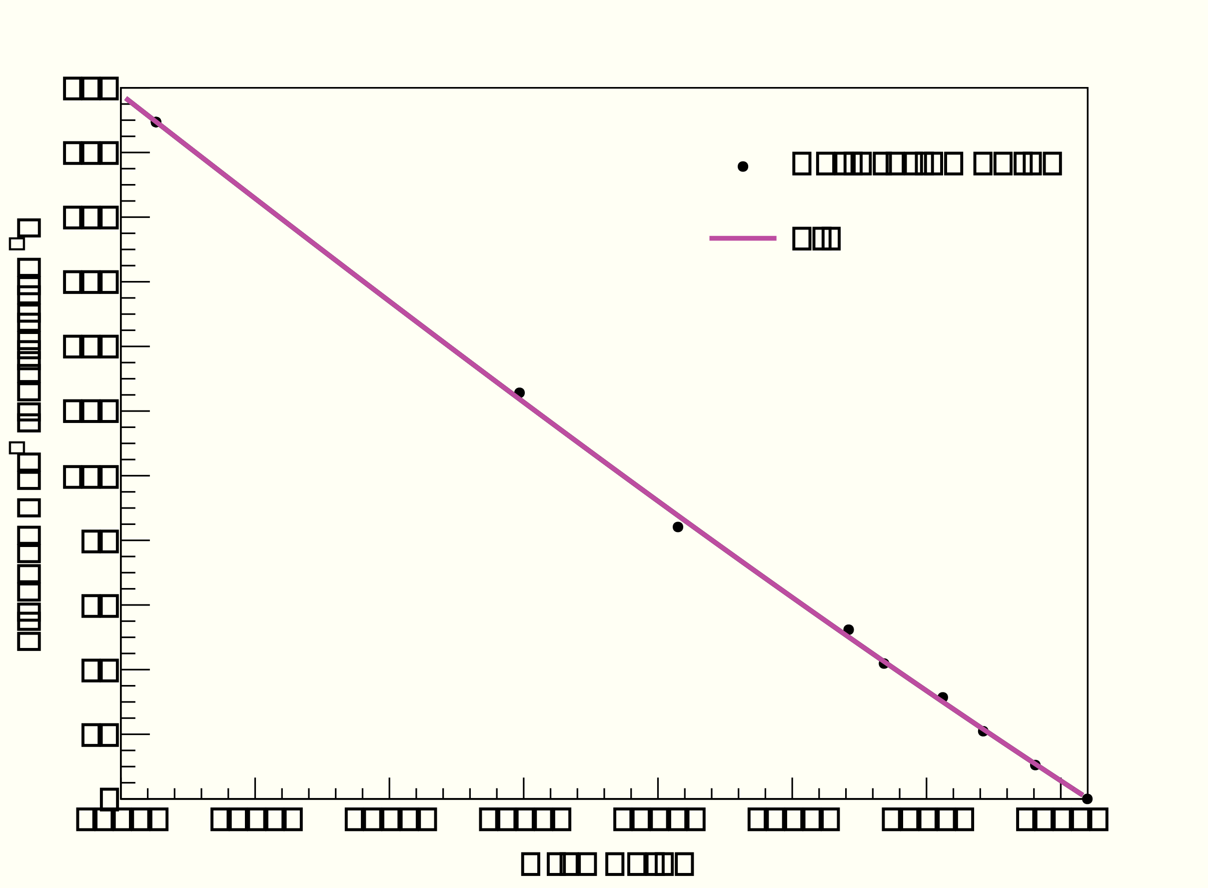

Figure 2.5.: Correlation between the grey value and the particle fluence obtained for the 200 MeV/u ^{4}He beam.

Once the films are calibrated and the conversion from pixel to millimeter applied, the broadening of the pencil beam with depth was studied evaluating the Full Width at Half Maximum (FWHM) (FWHM = 2.355 σ_{fit}) from the Gaussian fit of the measured x and y profiles of all frames (Fig. 2.4).

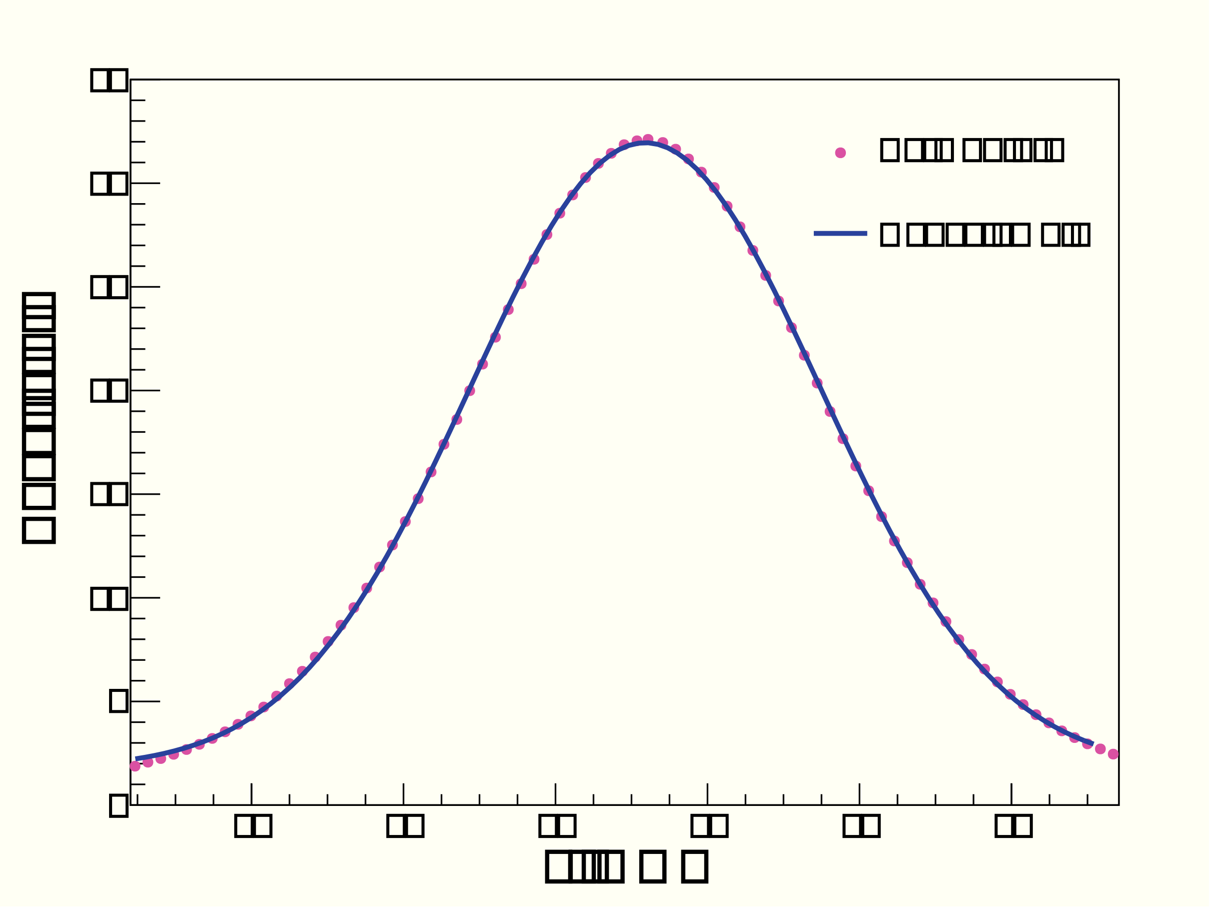

Figure 2.6.: Lateral profile of the 200 MeV/u ^{4}He beam at the isocenter. The experimental points can be described with a Gaussian function (line) with the following parameters: A = 1.78 (offset), B = 30.17 (constant), μ= 15.18 mm (mean value) and σ = 2.31 mm (distribution width).

The lateral profile measured with the films can be described with a single Gaussian function, as shown in Fig. 2.6, from which the FWHM at each position can be calculated. The results are reported in Table 2.1.

	120 MeV/u		200 MeV/u	
Position	FWHM_{ver}	FWHM_{hor}	FWHM_{ver}	FWHM_{hor}
1	2.7 ± 0.01	3.30±0.05	2.50±0.03	3.40±0.20
2	5.6±0.01	7.90±0.04	3.80±0.01	4.80 ± 0.07
3	8.9±0.02	9.30±0.02	5.70±0.01	6.10±0.01
4	13.7±0.04	13.40±0.05	8.60±0.02	8.30±0.02
5	22.0±0.03	21.80±0.08	13.80±0.03	13.90±0.06

Table 2.1.: Horizontal and vertical spreading evaluated from the Gaussian fit of the beam profiles at 120 and 200 MeV/u. The first column corresponds to the position of the films as shown in the scheme of Fig. 2.3.

The elliptical beam profiles observed at positions 1 and 2 are caused by the ion optics. The FWHM at the isocenter (position 3) were compared with the nominal focus sizes of the HIT libraries and agreements of 11% and 7% were found at 120 and 200 MeV/u, respectively. The measured values could be slightly higher because of the scattering in the films upstream of the isocenter (positions 1 and 2). These measurements have been repeated twice during different experiments and an agreement of 6% between the results was obtained.

The evolution of the beam profile along its path to the target can be also calculated with Scattmann, a program that transports a pencil beam through an arbitrary series of targets and calculates the beam width as a function of its position. For this tool, the basic multiple scattering calculations are performed with a Gaussian approximation of the Highland approach as described by Gottschalk et al. (see Sec. 1.2.3). Scattman can process an initial phase space of a beam that is parallel and has a certain divergence Θ angle and a focus point, as it is normally give by a real ion optical settings. These parameters were fitted to the film data.

The comparison between experimental and calculated FWHM values for the horizontal and vertical distributions at 120 and 200 MeV/u are shown in Fig. 2.7. The focus position (of the pure ion optical beam envelope without scattering) has been found at 25 cm after the nozzle (after the first MWPC as shown in Fig. 2.2) while the beam divergence is 3 mrad at 120 MeV/u and 2.5 mrad at 200 MeV/u.

The characteristics of the beams used in the experiments are reported in Table 2.2.

E_{beam} (MeV/u)	FWHM (cm)	Θ (mrad)
120.42 ± 0.01	9.50 ± 0.017	3.0
200.38 ± 0.01	5.60 ± 0.016	2.5

Table 2.2.: Nominal beam energy E_{beam} as given by the HIT libraries, FWHM at the isocenter and initial beam divergence Θ obtained from the comparison of the experimental FWHM with the prediction of the scattering simulation program Scattmann [20].

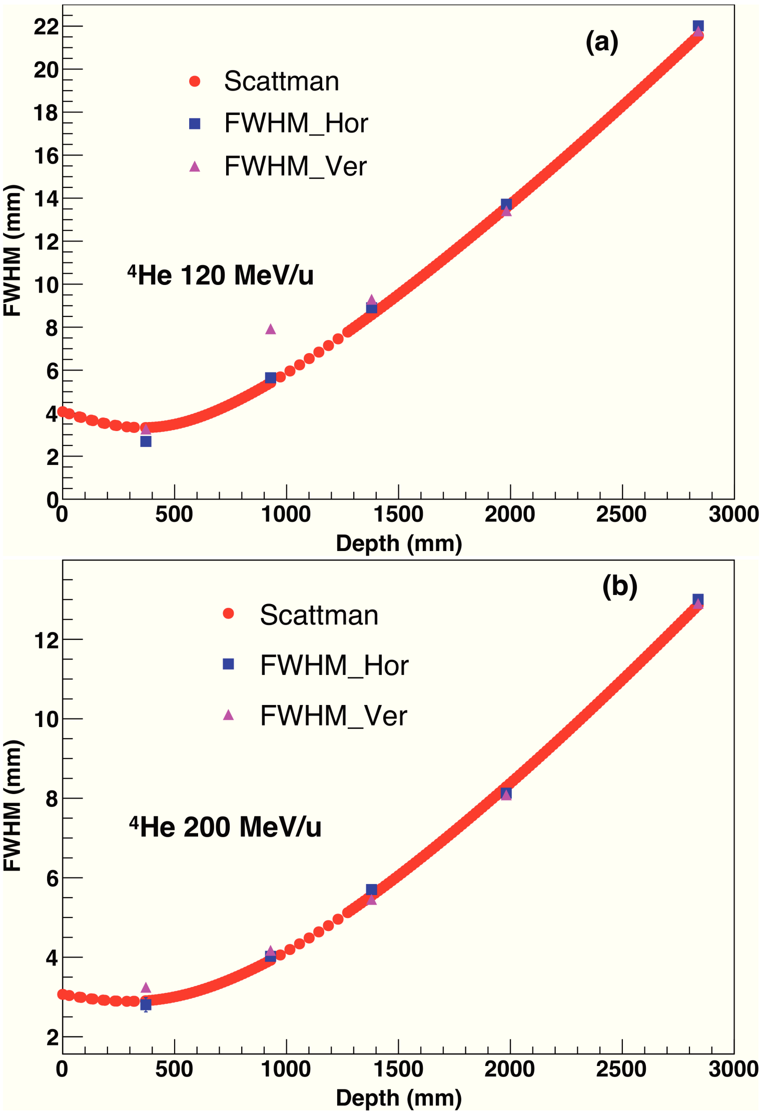

Figure 2.7.: Comparison between FWHM values given by Scattmann and the experimental data points. (a) is the envelope for 120 MeV/u ^{4}He and (b) the one for 200 MeV/u ^{4}He. z=0 is the position of the vacuum window.

2.3 Experimental setup

The experiments presented in this work aimed at obtaining the following results:

- Attenuation of the ^4He beam passing through different water and Polymethylmethacrylate (PMMA) depths;
- total yield of all secondary fragments produced by nuclear fragmentation at different water depths (fragments build up);
- angular distributions (later referred to as “differential yield”) of the remaining ^4He particles and secondary fragments between 0° and 23° with respect to the primary beam direction;
- kinetic energy spectra of all particle species;
- beam profile and lateral dose distribution after a scatter target with information on the beam halo.

Each type of measurement has a dedicated section where the experimental methodology and data analysis are described in detail.

2.3.1 Targets arrangements

For the fragmentation and scattering measurements three different targets have been used.

(i) Large and medium polystyrene flasks (manufactured by COSTAR), with outer dimensions 11.90 x 20.00 x 4.22 cm^3 and 8.33 x 9.01 x 3.48 cm^3, respectively. The total absorber traversed by the beam was 3.81 cm of water and 0.42 cm of polystyrene for the large flask and 3.16 cm of water and 0.32 cm of polystyrene for the medium flask. The total WEPL, measured with the PTW peak finder [39], was found to be 4.28 ± 0.01 cm H_2O for the large flask and 3.49 ± 0.01 cm H_2O for the medium flask.

(ii) A set of water targets designed and produced at the Nasa Space Radiation Laboratory (NSRL), Brookhaven National Laboratory, Upton NY, USA. All absorbers were circular with a 5.2 cm diameter and thicknesses of 1, 3 and 3.5 cm H_2O.

(iii) PMMA blocks of 5 cm thickness and 20 x 20 cm^2 area with a corresponding water equivalent thickness of 5.78 ± 0.01.

The different target thicknesses required for the beam attenuation measurements in water and PMMA have been realized using NSRL targets (1.0 - 3.5 cm H_2O), stacks of multiple large flasks or PMMA blocks. For the angular distribution measurements, 4.28 and 13.96 cm H_2O

thick targets were chosen to match half of the maximum penetration depth of the 120 and 200 MeV/u beams, respectively.

2.3.2 Attenuation of ^{4}He ions and build up of secondary fragments

The investigation of the primary beam attenuation in combination with the fragments build up gives information on the nuclear fragmentation of the ions passing through matter. A direct measurement of the projectiles Survival Fraction (S.f.) provides an estimate of total charge-changing or fragmentation cross section and of the correspondent mean free path λ.

The S.f. of 200 MeV/u ^{4}He ions together with the total yield of secondary fragments have been measured at different water and PMMA depths.

The attenuation measurements are used to validate the theoretical model implemented in TRiP98 for predicting the nuclear interactions of Helium in various materials and thus to calculate the correct amount of particles that need to be delivered at the tumor site. The build up of secondary fragments, instead, is required to evaluate the fragmentation tail in the dose profile.

Detector arrangement and electronics setup

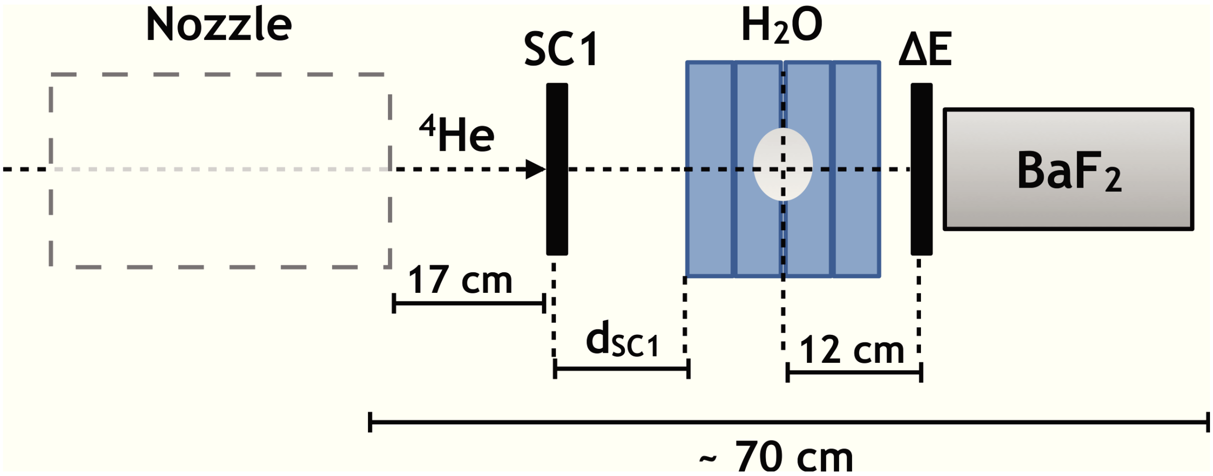

Figure 2.8.: Experimental setup used to study the attenuation of 200 MeV/u primary ^{4}He beam.

Three kinds of detectors were used for this experiment.

(i) A plastic scintillator (BC400 type) of 1 mm thickness coupled to an Hammamtsu R6427 photomultiplier (further referred to as SC1).

(ii) A plastic scintillator (BC400 type) of 5 mm thickness hexagonally shaped and with an inscribed radius of 5 cm coupled to an Hammamtsu R6427 photomultiplier (further referred to as ΔE).

(iii) A BaF_2 detector hexagonally shaped and with an inscribed radius of 4.37 cm. The crystal is surrounded in a 1 mm Al case and coupled to a Thorn EMI 9821 QB photomultiplier (further referred to as *E*).

A detailed description of the detectors characteristics is reported in Appendix B.1 B.2.

The detector arrangement is shown in Fig. 2.8. Particles exiting the beam line were monitored and counted with the SC1 detector placed downstream of the nozzle. The number of incident primary ions was compared to the number of fragments Helium (He) and Hydrogen (H) exiting the target, which were identified by a combination of the ΔE and the *E* detectors (also referred to as telescope system [40]). The latter allowed charge identification using the basic principle of energy loss described by the Bethe-Bloch formula (Eq. (1.3)). A particle incident on the telescope loses a small fraction of its energy in the ΔE and then fully stops inside the *E* detector up to a certain energy depending on its species. Therefore, the energy loss and residual energy are related to the charge and the mass of the ion, which can be identified by the signals measured by the ΔE and the *E* detectors. A ΔE-*E* Two dimensional (2D)-plot acquired during the experiment is shown in Fig. 2.9 as an example. In this kind of experiment it is important to maximize the detector solid angle to avoid any loss of primary ions and to detect as many fragments as possible. The maximum angular coverage achieved with the telescope system in this measurement was ±20°.

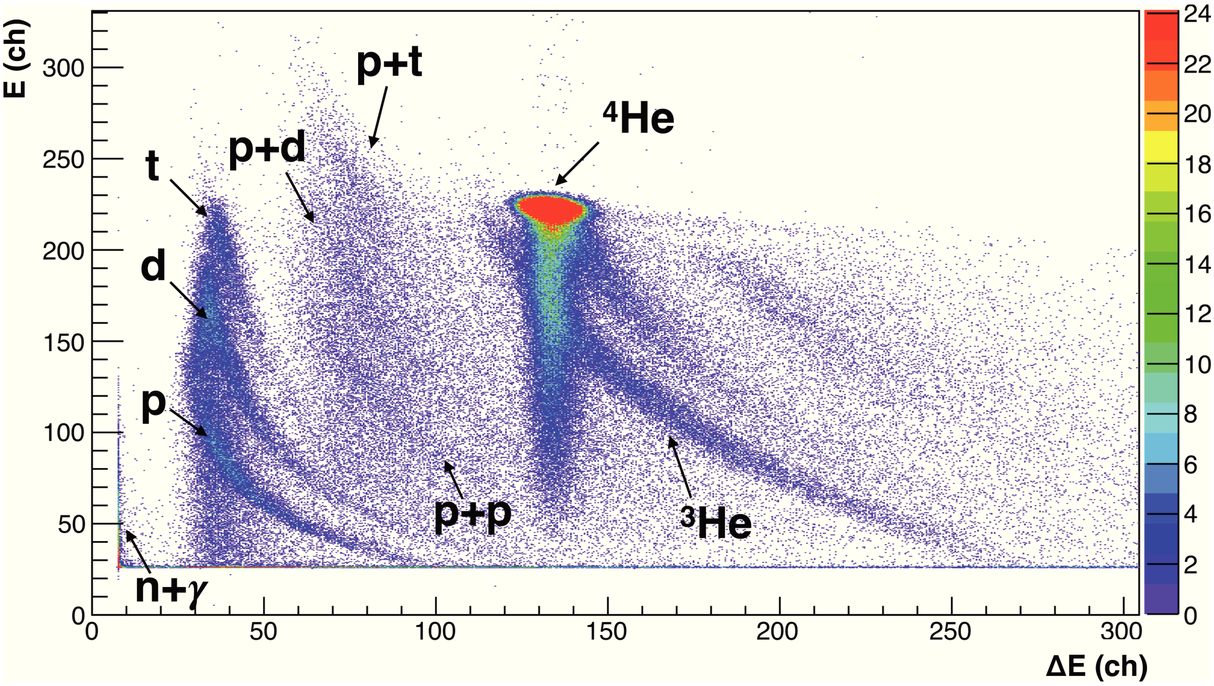

Figure 2.9.: ΔE-E spectrum of 200 MeV/u ^{4}He impinging on 17 cm water target. The labels indicate all the different particle species populations including the non-charged ones.

The data were recorded event-by-event using a VME (VERSA-Module Euro) based data acquisition system [41]. The electronic scheme of the setup in shown in Fig. 2.10.

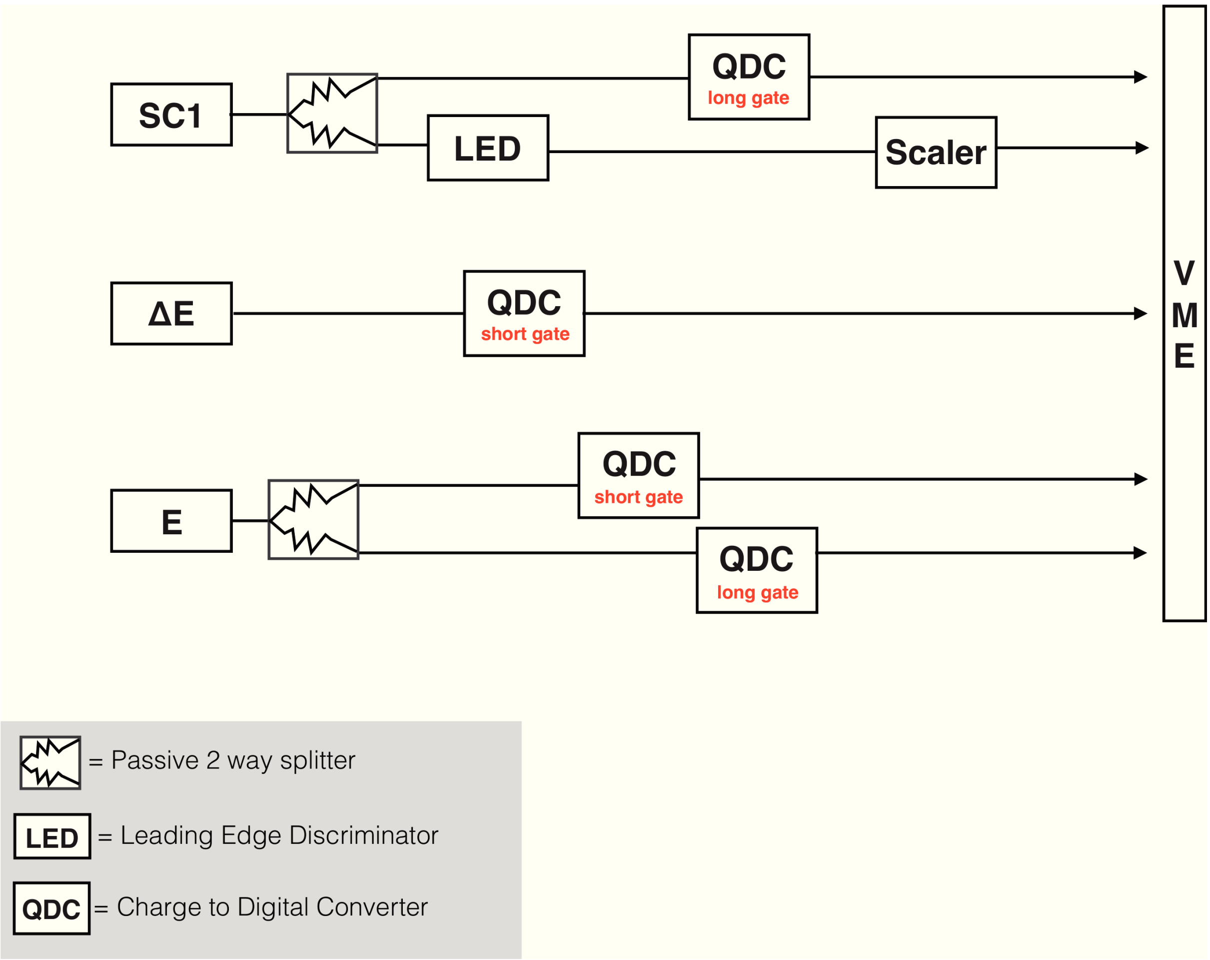

Figure 2.10.: Scheme of the electronics setup used for the primary ion attenuation and fragments build up measurements.

The data acquisition trigger was the discriminated signal of SC1. The analog signals of SC1, ΔE and the *E* detectors were sent to a Charge to Digital Converter (QDC) (CAEN V792N), where they were integrated over the selected gates. In particular, a short and a long gate were formed in order to integrate the short and long components of signal produced by the BaF_2 (*E*) detector [*]. The SC1 signal was integrated over the long gate and the ΔE signal over the short one. A scaler (CAEN V560) recorded the number of primary ions, corresponding to the number of trigger events, processed events and a pulse clock. The scaler information provided a constant check on the DAQ dead time, that was kept below 20% setting a beam rate always below 1000 particle/s. Runs without target were acquired in order to get information on the beam fragmentation in the experimental setup itself.

Data analysis

In the off-line analysis, the number of primary particles incident on the target was assessed from the SC1 energy spectrum by selecting events within ±3 standard deviations from the ^{4}He peak. For those events that met this requirement, particle identification in Z and Nuclear mass (A) was accomplished with a hand-drawn graphical contour in the 2D scatter plot ΔE-*E* as shown in Fig. 2.11.

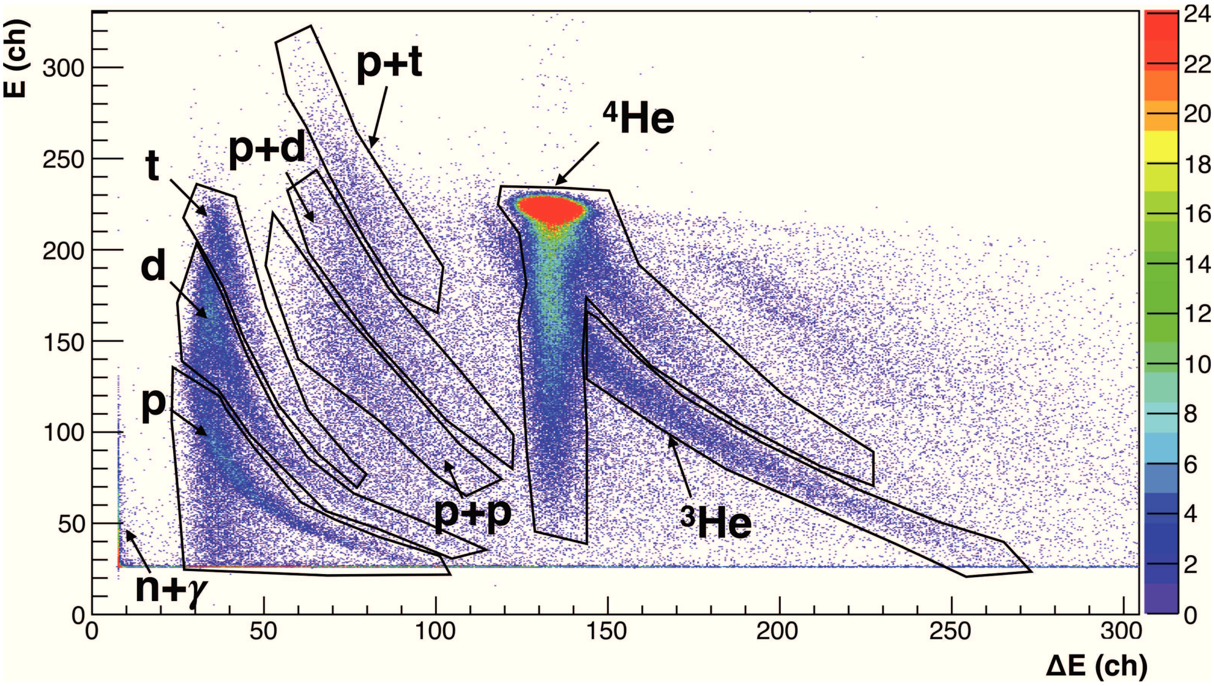

Figure 2.11.: ΔE-*E* spectrum of 200 MeV/u ^{4}He impinging on 17 cm water target. The contours around all the different species were drawn as an example of the graphical method applied for particle identification.

---

[*] The combination of the BaF_2 long and the short component is known as pulse shaping technique and can be used for particle identification

In this way, the amount of fragments per species were evaluated and directly normalized to the number of selected ^{4}He ions impinging on the target.

States like proton plus protons (p+p), proton plus deuteron (p+d) and protons plus triton (p+t) were also detected [†], as shown in Fig. 2.11. They were selected with the graphical contour approach and estimated as follow:

- each event of the p+p line is counted as two protons;
- each event of the p+d line is counted as one proton and one deuteron;
- each event of the p+t line is counted as one proton and one triton.

The total yield of all H isotopes was then calculated by the sum of these multiple events and the single events.

The dominant uncertainty of the method explained above is the systematic error stemming from the mis-identification of events in the graphical selection. To evaluate that, different contours were drawn including or excluding events of ambiguous identification [42]. An alternative analysis procedure for obtaining the number of surviving He particles and H fragments was performed by using only the ΔE spectrum (an example is shown in Fig. 2.12). As a first step, the whole spectrum was fitted with the sum of four combinations of a Gaussian and a Landau function (one for each peak) as shown in Fig. 2.13. The integral of each single peak, calculated using the parameters from the full-spectrum fit, provided an estimate of all particle species yield.

The comparison between the results obtained with the 1D fit method and the 2D graphical approach provides an estimate of the efficiency for the latter, especially for counting low-energy particles, as well as an error evaluation of the tail contribution in the ΔE detector. All these components were taken into account in the evaluation of the systematic error.

Fig. 2.14 shows the superposition of the 1-dimensional projections of the hand-drawn graphical cut and the full ΔE spectrum. It is possible to observe that the ^{3}He ions contributes to the tail above channel 150 more in respect to the ^{4}He ions.

Table 2.3 shows the systematic error in % for the different particle species. These values are calculated considering the average of the systematic error in all the different runs, in order to give a feeling of the systematic error on the particle yields. Moreover, a comparison between the yield calculated with the hand-drawn graphical contour and the 1D analysis method was made and the difference in % is shown in Table 2.3.

[†] These types of events are referred to as "multiplicity" states because they indicates that two particles hit the detector at the same time.

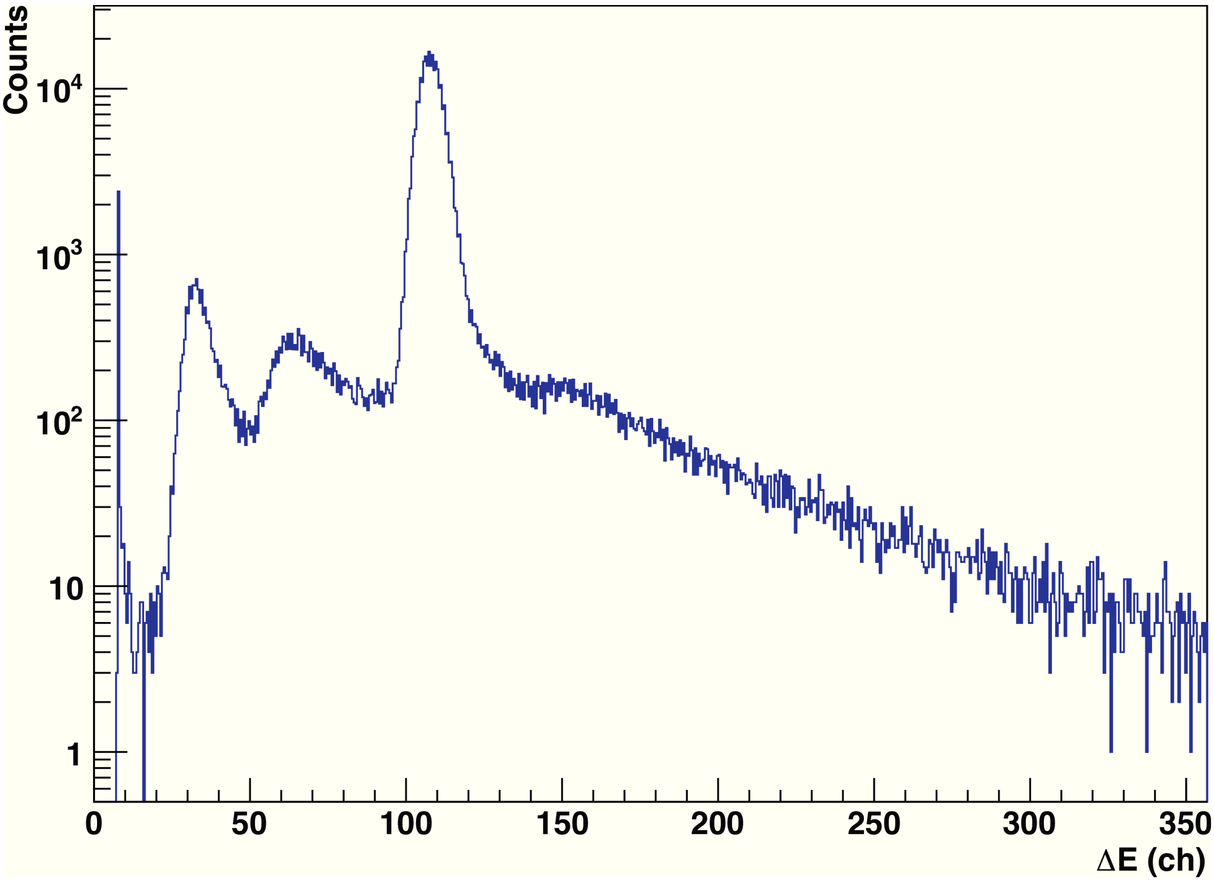

Figure 2.12.: ΔE spectrum acquired for 200 MeV/u ^{4}He ions impinging on 8.6 cm water target. Starting from the left, the first peak represents the pedestals which includes events who missed the detectors as well as uncharged particles (neutrons and gammas), the second peak contains H isotopes, the third peak all multiplicity states and the fourth peak the He isotopes.

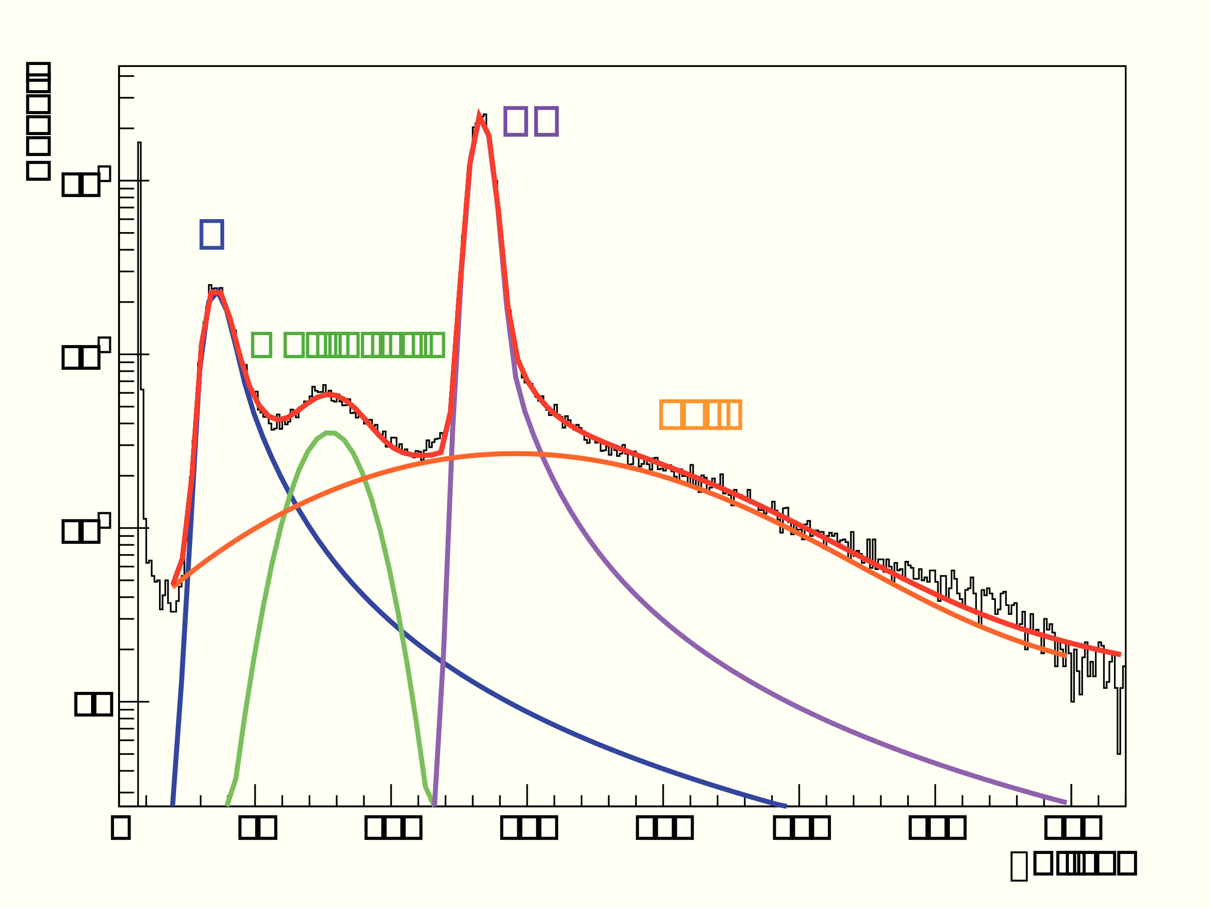

Figure 2.13.: $\triangle$E spectrum of the 200 MeV/u ^{4}He beam impinging on on 8.6 cm water target. The color lines represent the fit functions chosen for describing each peak (sum of a Gaussian and Landau distribution) and the whole spectrum (sum of all single-peak functions).

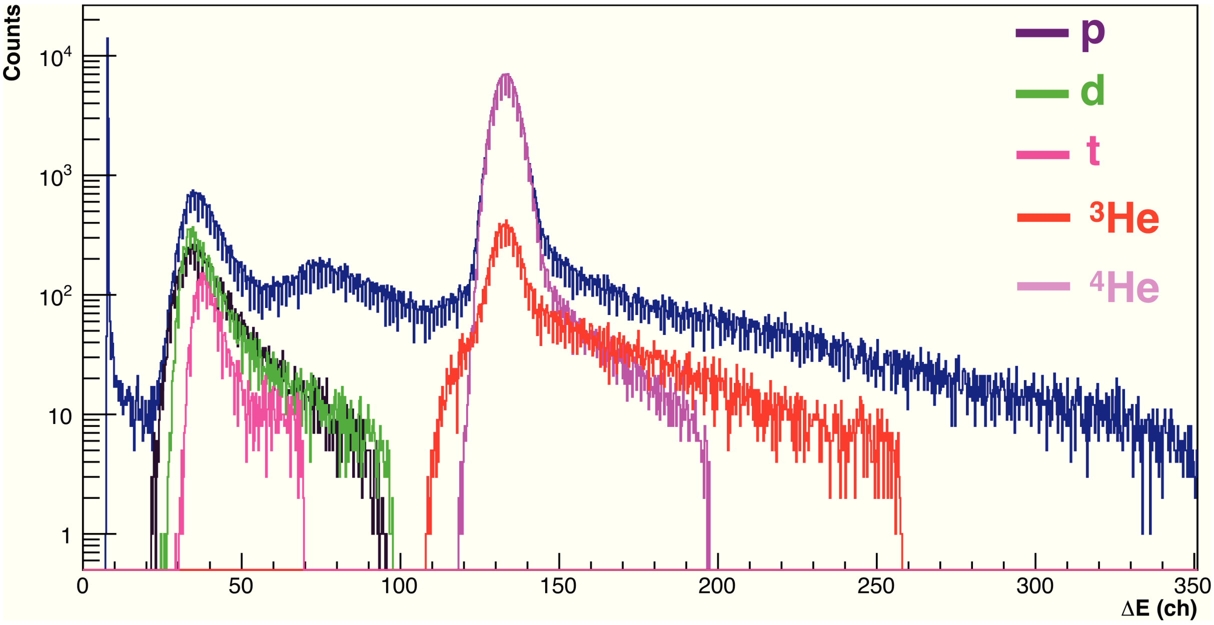

Figure 2.14.: Overlap between the total spectrum of the ΔE (line in dark blue) and the ΔE spectrum obtained from the application of the graphical cut of p, d, t, ^{3}He and ^{4}He.

	^{4}He	^{3}He	p	d	t
Graphical contour	6%	56%	31%	14%	11%
	Tot. He		Tot. H		
1D analysis	4%		23%		

Table 2.3.: For every measurement run the error estimation coming from the hand-drawn graphical contour was estimated. The values in the line "1D Analysis" report the difference between the yields calculated from the graphical contour and the 1D analysis procedure.

2.3.3 Angular distributions and kinetic energy spectra

Differential yield and energy spectra of all particles kinds at 0°, 2°, 4°, 6°, 8°, 12° and 23° with respect to the primary beam direction were measured for 120 and 200 MeV/u ^{4}He particles impinging on 4.28 and 13.96 cm thick water targets.

The angular distributions give information on fragmentation, multiple and nuclear scattering processes. The combination of differential yield and kinetic energy spectra provide double differential cross sections.

All detectors listed in section 2.3.2 for the attenuation experiment were also used in this experiment. The scheme of the setup is shown in Fig. 2.15.

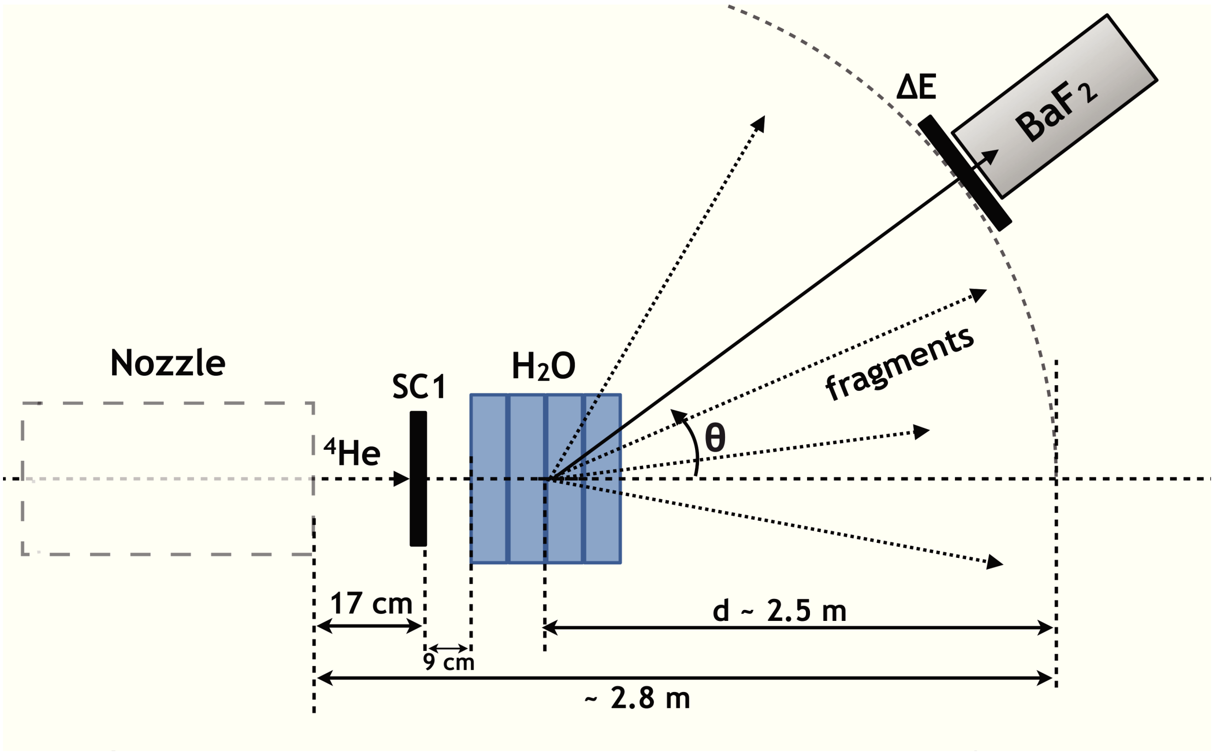

Figure 2.15.: Scheme of the experimental setup used for acquiring angular distributions and kinetic energy spectra.

Particles exiting the beam line were monitored and counted with the SC1 detector placed downstream of the nozzle. The targets were placed at 9 cm from the SC1. The surviving ^{4}He ions together with the secondary particles emerging from the target were detected with the telescope system ΔE-E (see section 2.3.2 - Data Analysis) placed at ~2.5 m from the target center (see Fig. 2.15). The Time of Flight of each fragment was measured considering the travel distance d. From the time measurement it is possible to calculate the kinetic energy of each particle species. The total energy E_{tot} of a relativistic particle is

$$E_{tot} = \gamma m_0 c^2 \qquad E_{tot} = m_0 c^2 + E_{kin} \tag{2.2}$$

where $\gamma = 1/\sqrt{(1-\beta^2)}$ is the relativistic factor, m_0c^2 is the mass at rest of the particle and E_{kin} its kinetic energy. If $\beta = d/tc$, the kinetic energy can be calculated as follow

$$E_{kin} = \left(\frac{1}{\sqrt{1-\left(\frac{d}{tc}\right)^2}} - 1 \right) \cdot m_0c^2 \tag{2.3}$$

where t is the time-of-flight required by the particle to travel the distance d. However, the measured TOF is $t_{TOF} = t_{prim} + t$, where t_{prim} is the time interval between the detection of a primary ion in the SC1 detector and the occurrence of the fragmentation reaction in the target, instead t is the time needed for a fragment to travel from the reaction point till the detector E. The time t_{prim} was calculated assuming that all reactions occur at the center of the target and taking into account that the primary ions looses energy between SC1 and the reaction point and thus slow down. The energy loss was calculated with the program LISE++ [43].

The data were recorded event-by-event using a VME (VERSA-Module Euro) based data acquisition system [41]. The scheme of the electronic setup is shown in Fig. 2.16.

In the analog branch the signals of SC1, ΔE and E detector were feed first into an Amplifier (AMP) (CANBERRA 2026) and then into the Analog to Digital Converter (ADC) (CAEN - V785N) that recorded the energy spectra.

The logic branch, instead, is more complex. The raw signals of SC1 and the E detector were sent to a Leading Edge Discriminator (LED), whose outputs were cabled into two hardware coincidence units: one for providing the data acquisition trigger and one for creating one of the signals to measure the TOF.

To acquire only relevant events, the trigger is created only when there is a coincidence between a signal from the primary beam in SC1 and a surviving primary ion or fragment reaching the E detector. The time signals fed into the coincidence unit are shown in Fig 2.17.

The SC1 signal was delayed so that its minimum time difference with the E signal was slightly bigger than the time needed by the fastest particles (photons) to cover the entire TOF distance. Moreover, the width of the SC1 signal was made larger than the TOF of the slower particles. The output of this coincidence was sent to a Dual Timer (DT) which produced the data acquisition trigger as well as the signal to create the ADC gates with a Gate Generator (GG). For this experiment, the short gate was set to 20 ns and the long gate to 1 μs.

A start and a stop signal are required as inputs of the Time to Digital Converter (TDC) to measure the TOF. In the present experiment, the so-called inverse logic method (use of the beam monitor SC1 as a stop rather than a start) was used. The trigger signal was sent to the TDC as a start while an additional coincidence was formed to produce the stop signal. The time scheme of signals to create the new coincidence is shown in Fig 2.18.

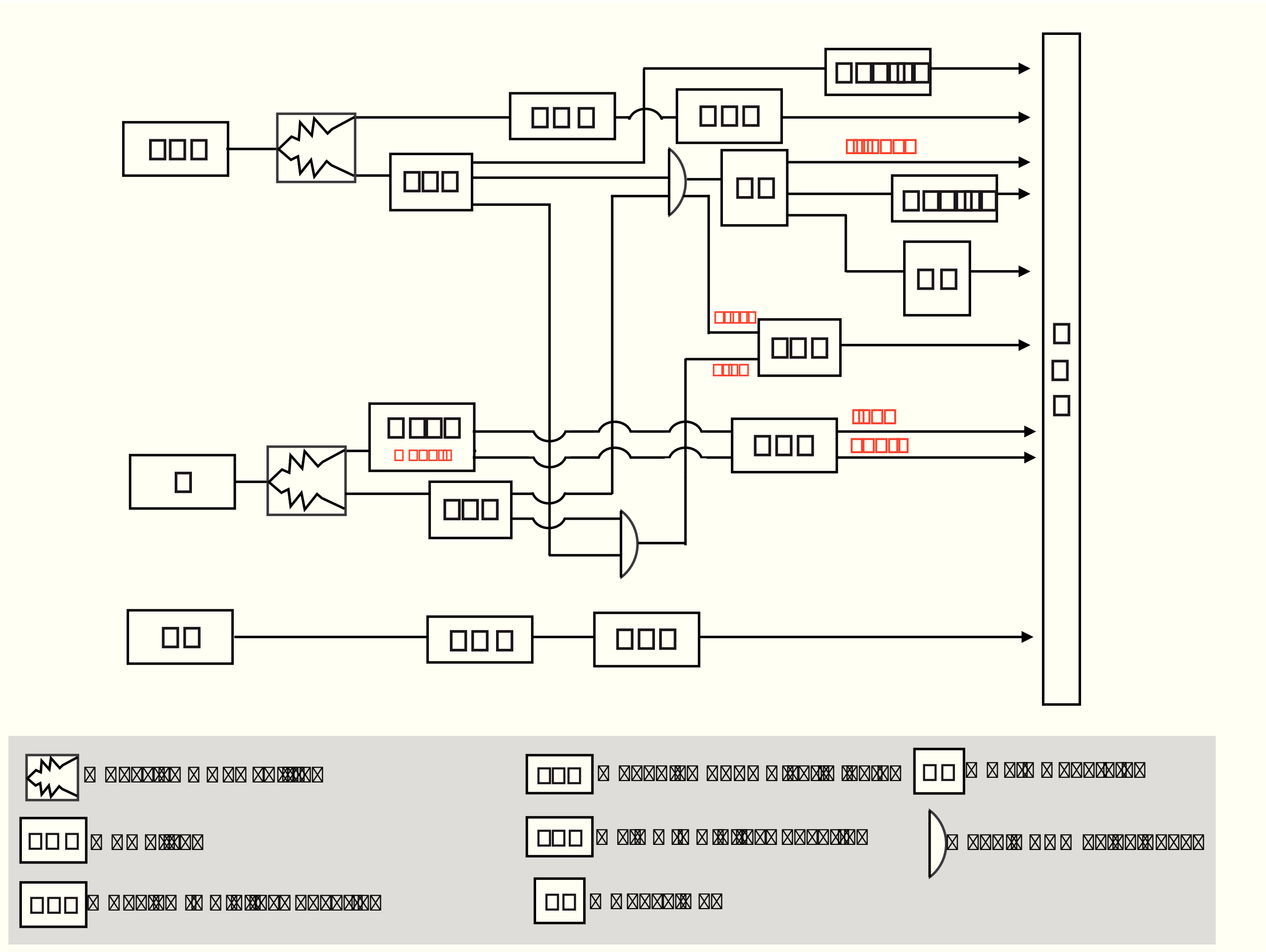

Figure 2.16.: Scheme of the electronic setup used for acquiring angular distributions and kinetic energy spectra.

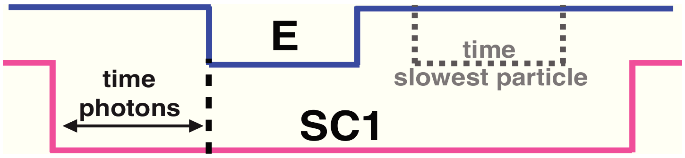

Figure 2.17.: Time scheme of the logic signals sent to the coincidence module to produce the data acquisition trigger.

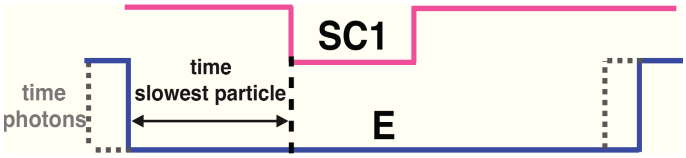

Figure 2.18.: Time scheme of the logic signals sent to the coincidence module to produce the TDC stop.

In this case the leading signal of the coincidence, i.e. the signal opening the coincidence, is the SC1 signal. The latter was delayed in a way that the minimum distance with the E signal is the time needed to the slowest particle to travel the TOF distance. Furthermore, the digital E signal had to be wide enough to get a valid TDC output for the fastest particles (photons).

The reason for choosing the inverse logic methodology are mainly two: i) to be sure that the signal of the E detector is correlated to the signal of a primary beam in the SC1; ii) avoiding a lot of start signals without a stop decreasing the efficiency of the TDC.

In order to get the total number of incident ions, the discriminated SC1 signal was sent to a scaler (CAEN V560) together with the output of the DT for the free triggers (number of triggers formed and send to the dat acquisition system) and a pulse clock. The free triggers together with the events recorded by the data acquisition (accepted triggers) are used to estimate the dead time:

$$dead\ time = 1 - \frac{Accepted\ triggers}{Free\ triggers} \tag{2.4}$$

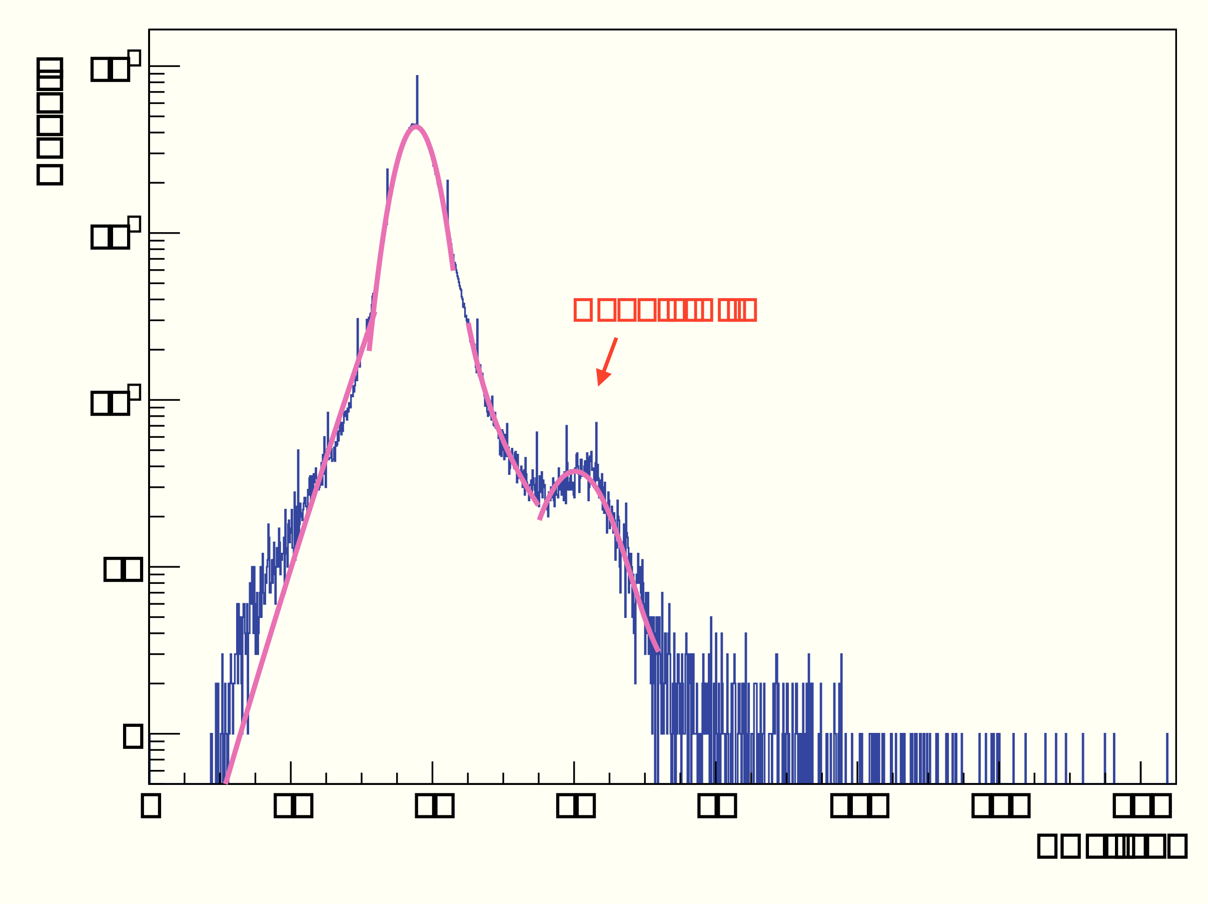

Figure 2.19.: SC1 raw energy spectrum of 200 MeV/u ^{4}He beam. The single and double hits contributions were estimated from the integrals of the fitting functions shown in magenta.

The beam rate was always set below $6{\cdot}10^5$ particle/s keeping the dead time lower than 5%. Intensity oscillations were observed during the runs, causing an increase of the multiple hits in the SC1 detectors [‡] At the selected beam rate the number of observed double hits was on average ~10%. An example of a raw SC1 spectrum with double hits is shown in Fig. 2.19.

Data Analysis

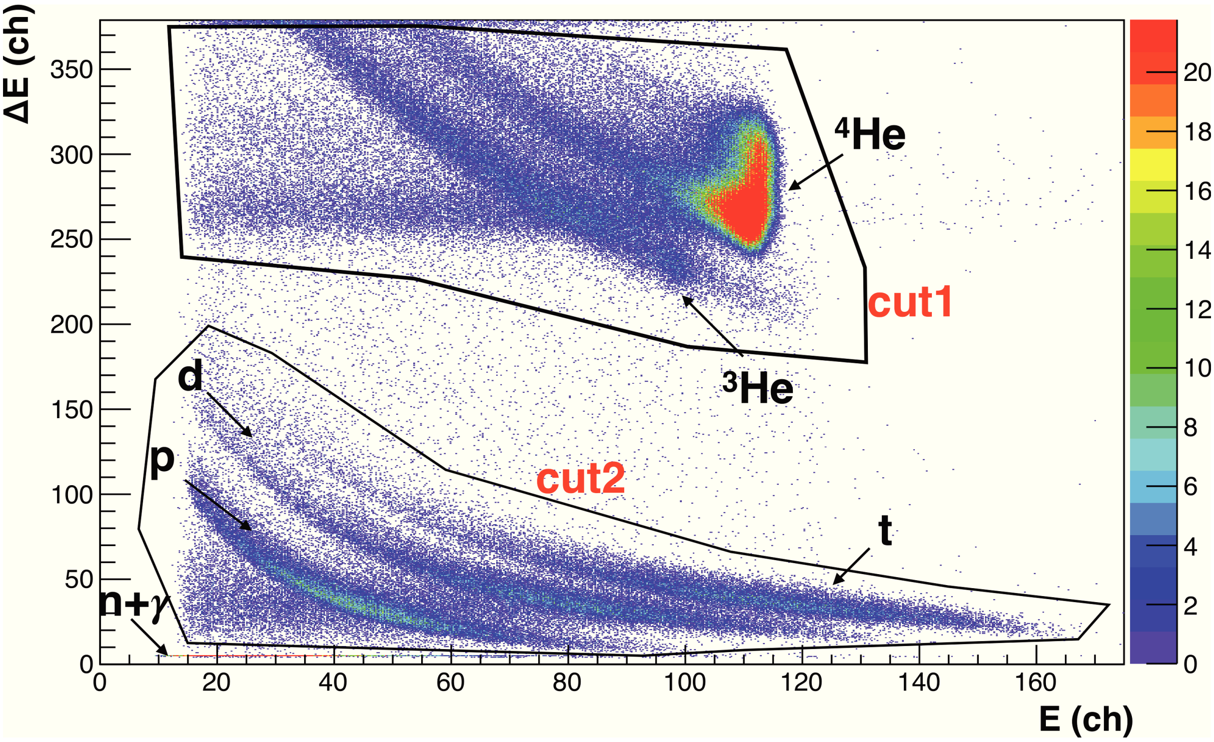

Figure 2.20.: ΔE-E 2D-plot of 200 MeV/u ^{4}He impinging on a 13.96 cm thick water target. The graphical contours labelled as "cut1" and "cut2" are example of the particle identification method used in this analysis.

The data analysis for extracting the angular distributions and the kinetic energy spectra requires two steps:

1. particle identification with the 2D-spectrum ΔE-E and isotope discrimination with the 2D-spectrum E-TOF;
2. calibration of the TDC spectrum in TOF values and translation of the time spectrum in kinetic energy.

The particle identification method is based on the same concept explained in Sec. 2.3.2. Every particle species was selected graphically in the 2D-scatter plot ΔE-E as shown in Fig. 2.20. Each

---

[‡] Multiples hits occur when at least two primary ions arrive simultaneously on the SC1 detector depositing double the energy of a single ion.

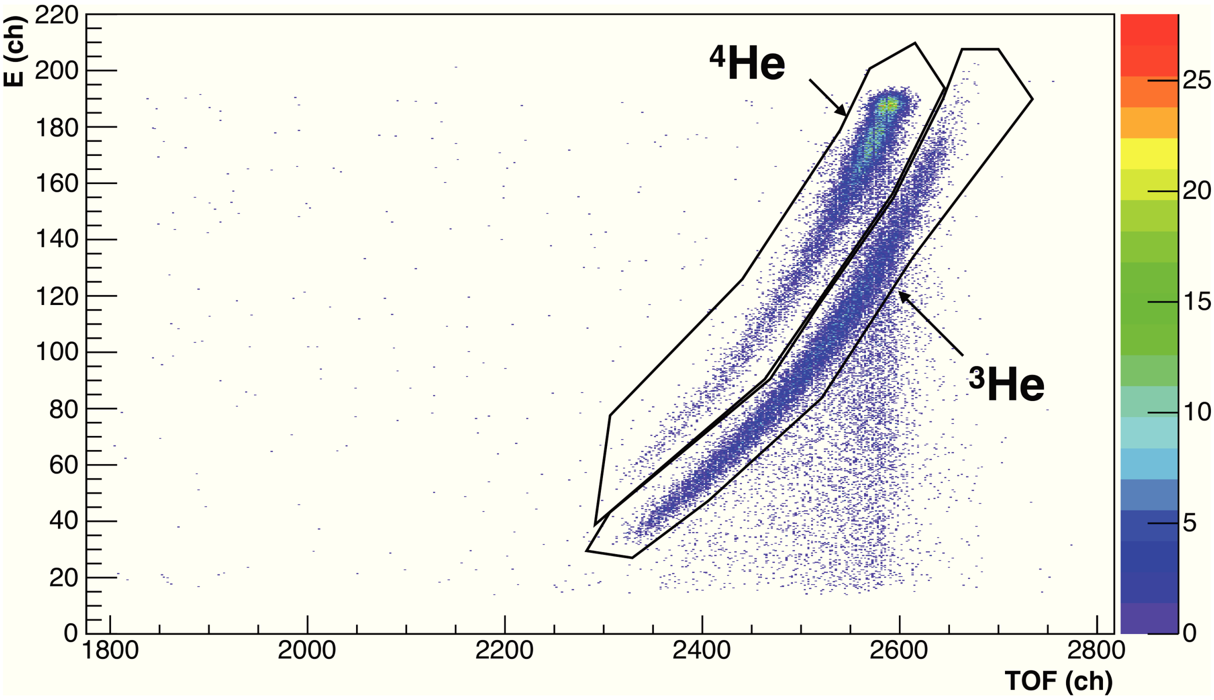

Figure 2.21.: E-TOF 2D-plot after the selection "cut1" is applied. The ^{4}He and ^{3}He ions can be separated graphically.

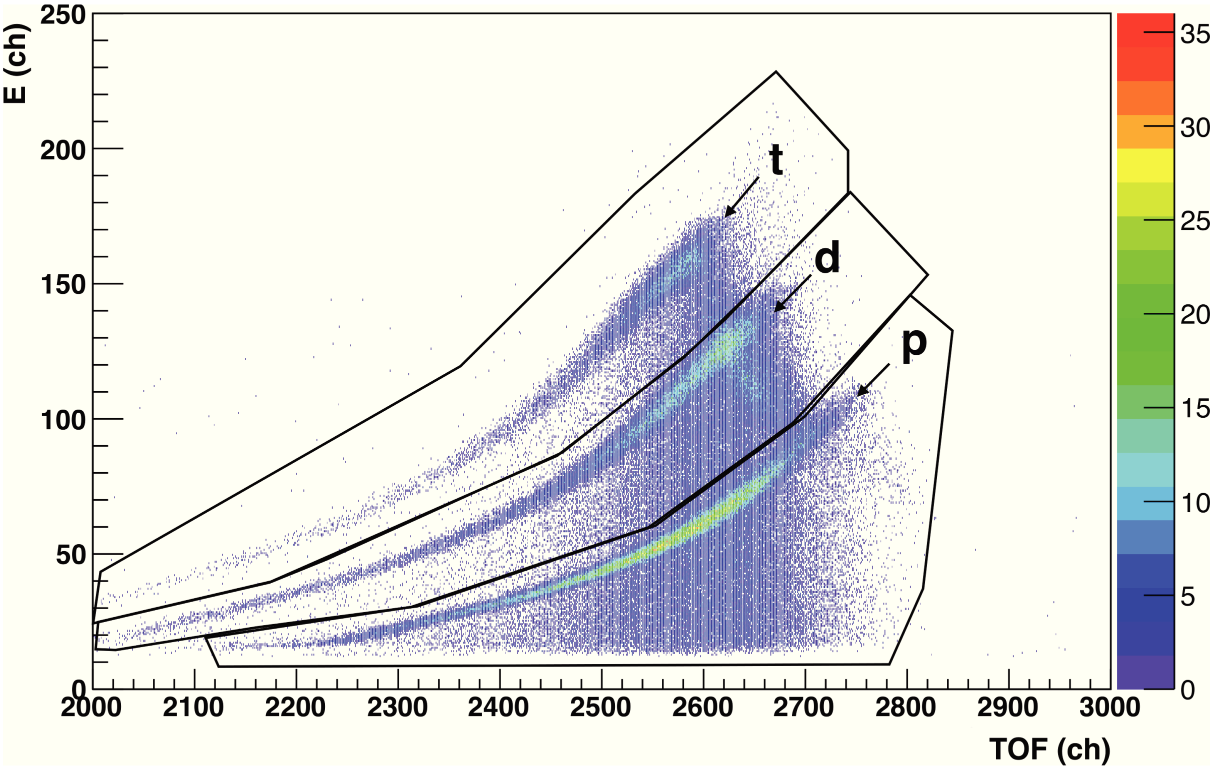

Figure 2.22.: E-TOF 2D-plot after the selection "cut2" is applied. Protons, deuterons and tritons can be separated graphically.

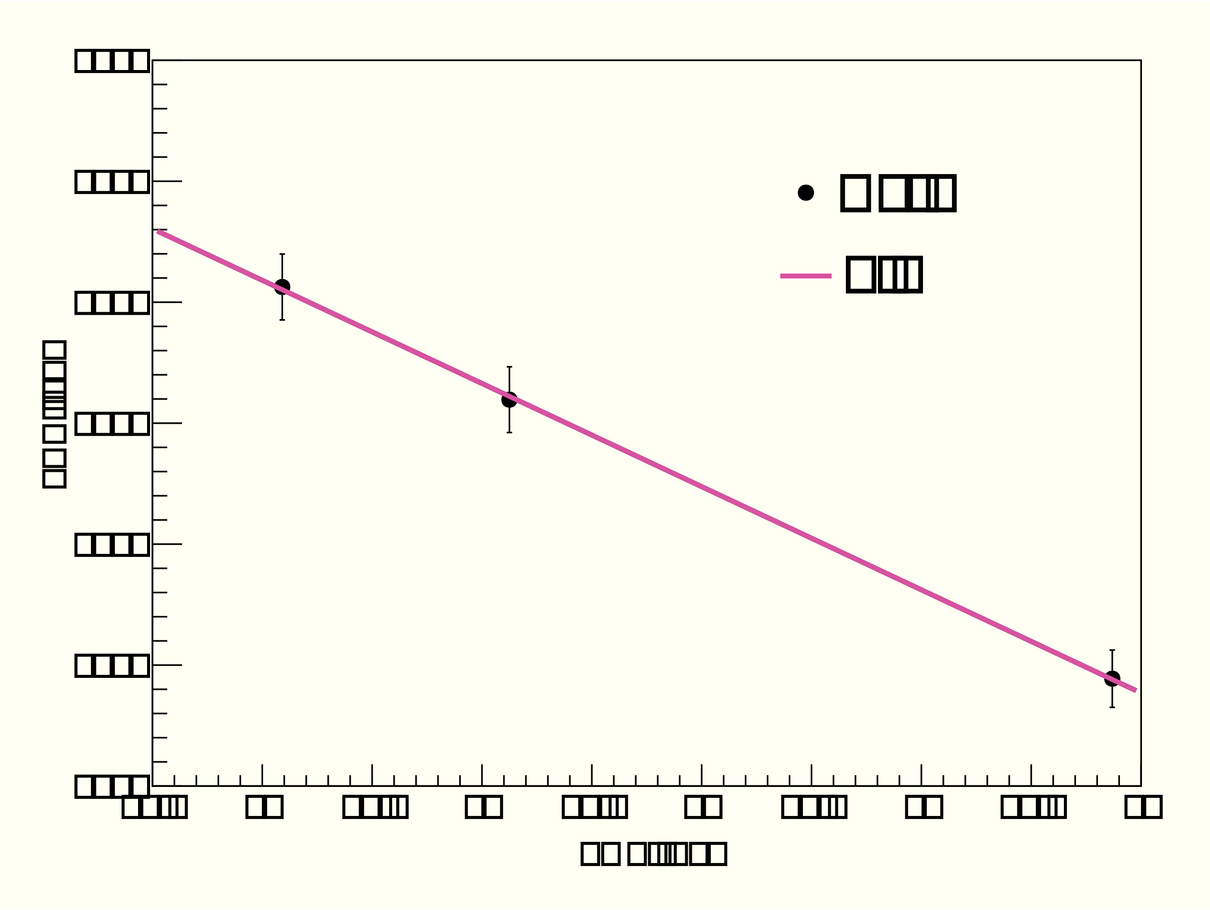

Figure 2.23.: Relation between the TDC channels and the theoretical TOF in ns for 120, 170 and 200 MeV/u beams without target. The line represents the linear fit applied to the data points. The slope is the TDC resolution. The error bars correspond to the FWHM obtained from fitting the TDC spectrum with a Gaussian distribution.

selection (referred in Fig. 2.20 as "cut1" and "cut2") was then applied to the E-TOF scatter plot, where a second hand-drawn contour was made to discriminate the different isotopes, as shown in Fig. 2.21 and Fig. 2.22.

As discussed in Sec. 2.3.2, the largest uncertainty in the particle discrimination method comes from the the graphical selection. As for the attenuation analysis, different contours were drawn to include or exclude events of ambiguous identification [44]. On average, a total error (systematic and statistical contribution) of 10% for ^{4}He ions, 15% for ^{3}He ions, 20% for protons, 30% for deuterons and 25% for tritons were found.

In order to get the kinetic energy distributions of every particle species, the raw TOF specta were time-calibrated. A linear relation is assumed to link the channels of the TDC spectrum with the time in ns of the TOF. For this reason three datasets for 120, 170 and 200 MeV/u ^{4}He beams were recorded without target with the telescope placed at 0°. For each calibration run, the TDC spectrum was fit with a Gaussian distribution from which the mean value and FWHM could be estimated. Knowing the particles velocity, the theoretical TOF was calculated and associated

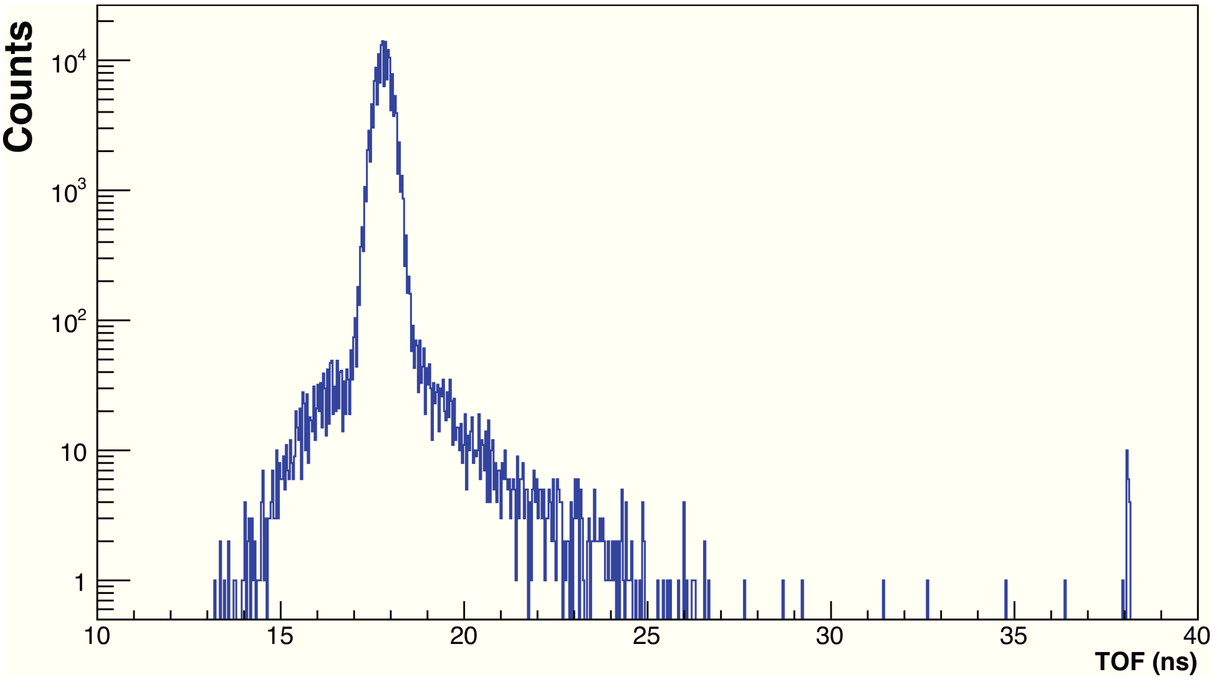

Figure 2.24.: Calibrated TOF spectrum of the target out run for the 120 MeV/u ^{4}He beam.

to the corresponding channel. The calibration function obtained with a linear fit on the data (Fig. 2.23) is:

$$TOF[ns] = 0.023 \pm 0.002 \left[\frac{ns}{ch}\right] \cdot TDC[ch] - 78.5254 \tag{2.5}$$

By applying Eq. 2.5 to the raw TDC spectrum a time of flight spectrum calibrated in ns is obtained (Fig. 2.24).

The graphical selections were then applied to the calibrated TOF spectrum and converted into kinetic energy distributions using Eq. 2.3.

The main uncertainty on the kinetic energy spectra stems from the TOF resolution Δt, calculated through the FWHM of the TOF spectra used for the calibration. Δt were found to be 0.66 ns and 0.74 ns at 120 and 200 MeV/u, respectively. The error propagation for the kinetic energy spectra was calculated as follow:

$$\frac{\Delta E}{E} = -\gamma(\gamma+1)\frac{\Delta t}{t} \tag{2.6}$$

where γ is the relativistic Lorentz term.

2.3.4 Scattering measurements

At energies of several hundred of MeV/u required in ion therapy, ions passing through a medium undergo multiple scattering, which results in a lateral beam spread. Moreover, the nuclear

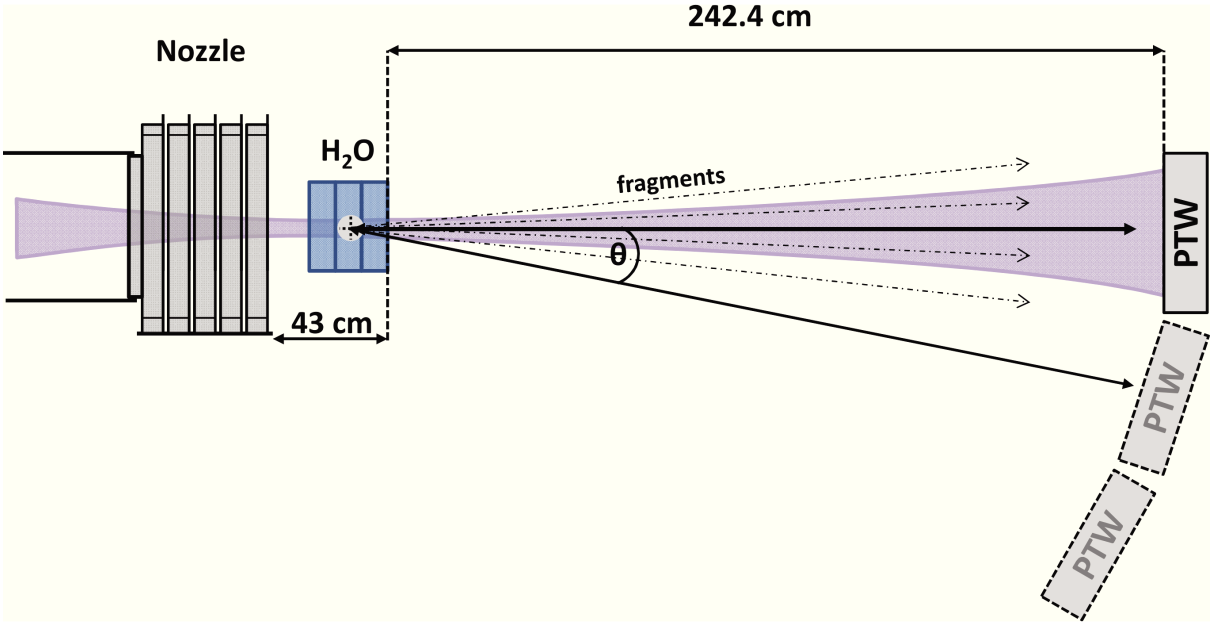

Figure 2.25.: Scheme of the experimental setup for the scattering measurements. The target was placed at 43 cm downstream of the nozzle. At 0°, a film was always placed at the same position of the PTW detector.

process are responsible of scattering at large angles that is described in the halo of the lateral beam profile.

When treating a cancer patient with ions, two different sources contribute to the angular spreading: the material in front of the patient (i.e. the nozzle) and the tissue between the entrance point and stopping depth inside the patient.

A measurement of the beam profile along its path to the tumor site is important because it describes the Coulomb interactions of projectile and target nuclei (beam core) and the nuclear reaction processes (beam halo).

The scattering in water was measured for 120 and 200 MeV/u ^{4}He ions, using 1 large flask and 4 medium ones, respectively. For the same energies and targets the radial dose profile distribution at angles between 0° and 20° with respect to the primary beam direction was acquired, used as comparison measurements for the angular distribution measurements presented in Section 2.3.3.

Detector arrangements

EDR2 films and the PTW 2D array detectors were used for this experiment. The latter is a device commonly used to measure beam profiles from medical linear accelerators and consists of a 1405 ionization chambers matrix (a technical description can be found in Appendix A.2). The setup configuration is shown in Fig. 2.25.

The target was placed at 43 cm after the nozzle and the PTW array or the film was centered to the beam axis at 2.40 m from the target. The distances were chosen to reproduce the configuration used for the angular distribution measurements (Section 2.3.3).

The PTW detector was irradiated with a pencil beam with intensity of $\sim 10^8$ particle per spill until the halo of the distribution was well characterized. For the EDR2 films, instead, the beam intensity was increased in order to oversaturate the detector center and get a higher signal in the halo region.

In addition to the beam profile, the beam lateral dose distribution was measured by moving the PTW detector in arc to cover angles between 0° and 20° with respect to the primary beam direction.

Data analysis

The films, as in the envelope measurements described in section 2.2, were developed immediately after irradiation, scanned and analyzed. Once calibrated, the films were rotated in order to select the longest side of the profile as shown in Fig. 2.26.

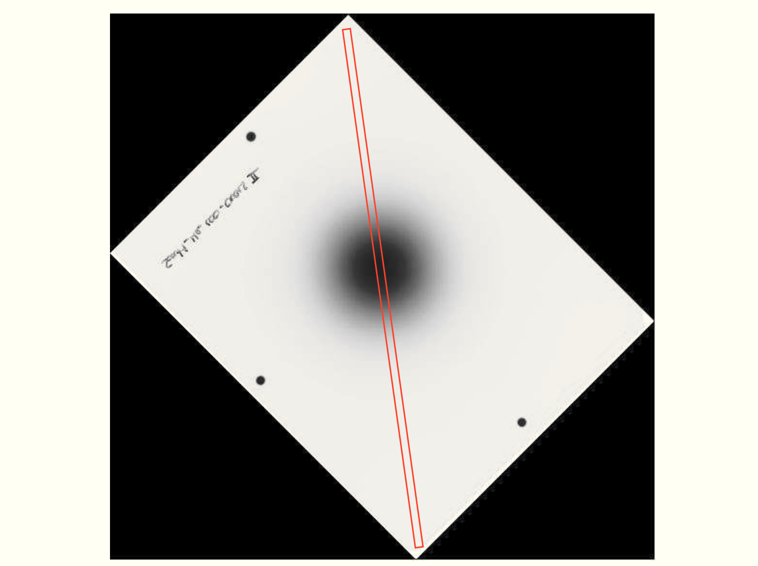

Figure 2.26.: Example of the film analysis procedure for assessing the beam halo.

An example of the beam profile extracted with this method is plotted in Fig. 2.27. The film response showed a high spatial resolution. A slight gradient from right to left can be observed, probably caused by the developing process. In the tails, the jittering of the data is more pronounced because of the low signal from the halo region.

The PTW 2D-array has an in-built software that allows a direct evaluation of the 2D beam dose profile. An example of the detector raw output is shown in Fig. 2.28(a). The dose matrix was then filtered assuming a radial symmetric distribution to reduce the detector noise in the halo region. The filtered distribution is shown in Fig. 2.28(b). A 1D dose profile was extracted

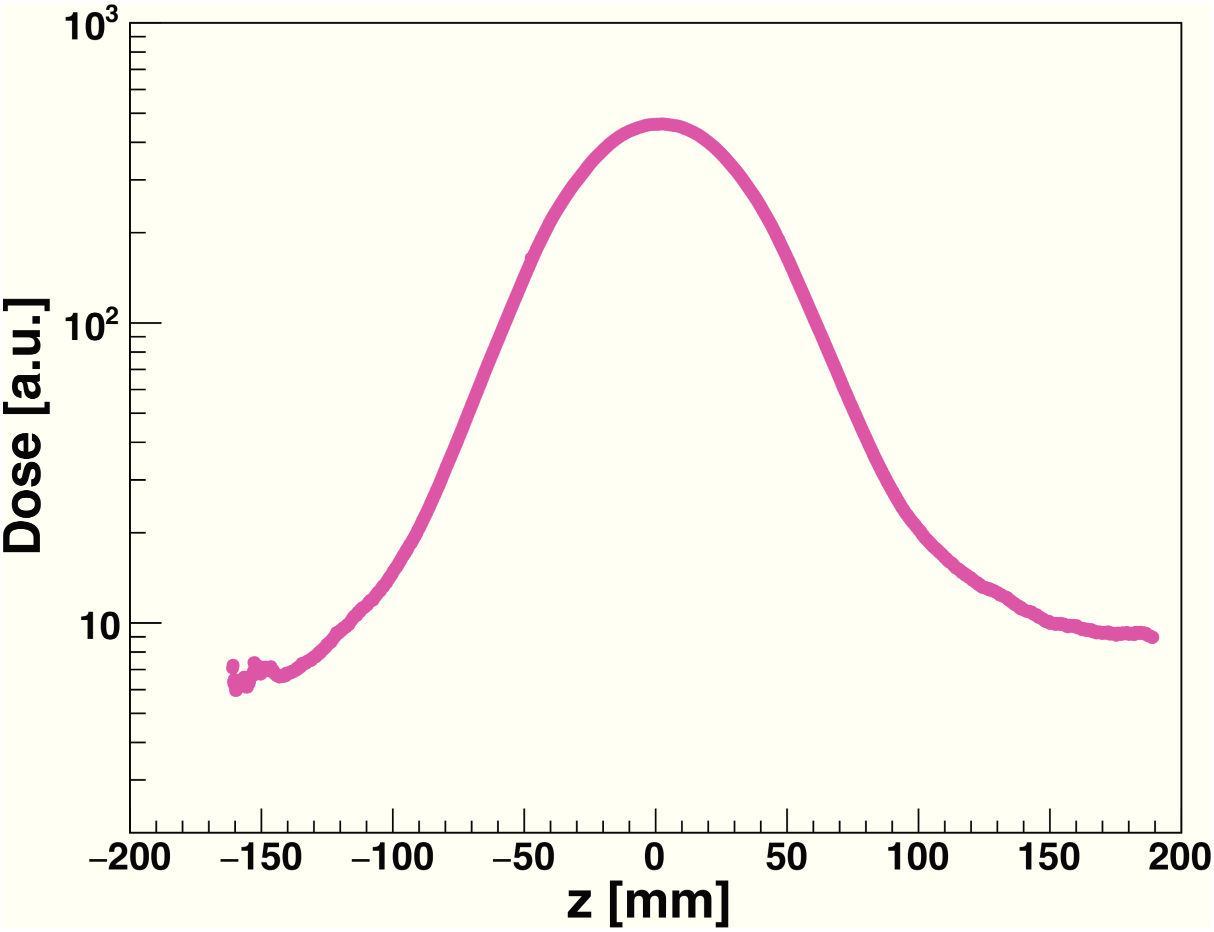

Figure 2.27.: Beam profile measured with the film for 200 MeV/u ^{4}He beam impinging on a 13.96 cm thick water target. The measurement was performed at a distance of ∼2.5 m from the target.

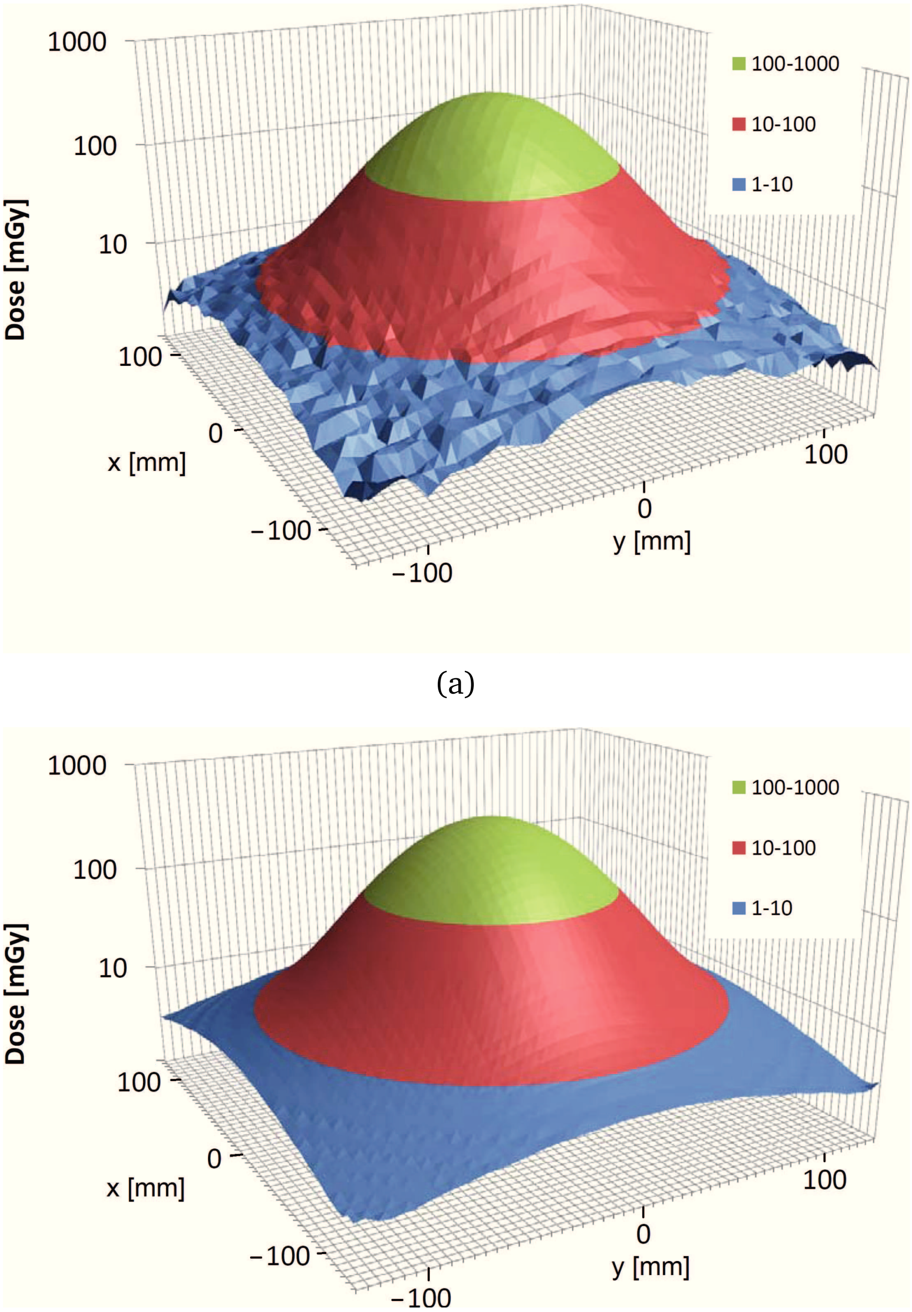

(a)

(b)

Figure 2.28.: Dose distribution given by the PTW 2D-array for 200 MeV/u ^{4}He ions scattered by a 13.96 cm H_2O target. (a) represents the raw matrix and (b) the filtered one.

from the filtered matrix (Fig. 2.29), analyzed and compared to the films response. The filtered distributions of the PTW array proved to be good in terms of noise especially in the tails region.

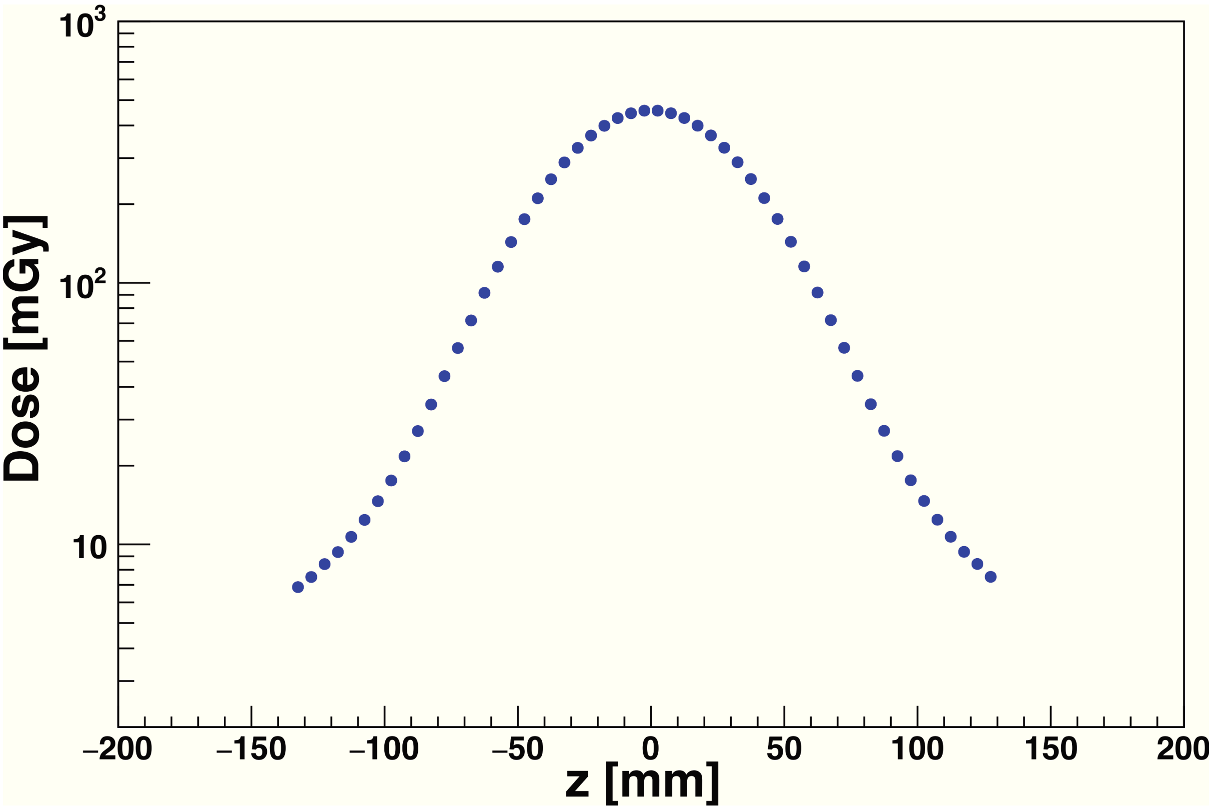

Figure 2.29.: Beam profile evaluated with the 2D-array for 200 MeV/u ^{4}He beam impinging on a 13.96 cm H_2O target. The measurement was performed at a distance of ∼2.5 m from the target.

3 Results and discussion

3.1 Absorption of primary beam flux and secondary fragment production

The results of the primary ions attenuation and secondary fragments build up for a 200 MeV/u ^{4}He beam interacting with water and PMMA are presented in this section.

Using the setup of Fig. 2.8, the yield of the ^{4}He beam (also referred to as survival fraction S.f.) was measured by comparing the amount of primary particles impinging on the target (N_{4He}^{in}) with the number of Helium ions surviving the target (N_{4He}^{out}), so that the yield is given by

$$Yield = \frac{N_{4He}^{out}}{N_{4He}^{in}} \tag{3.1}$$

For the secondary fragments, the yield is given by the ratio between the number of a given particle species N_Z detected behind the target and the incoming primary ions N_{4He}^{in}. This fraction was then corrected by the fragmentation in the nozzle and experimental setup estimated with a target out run.

The mean free path λ can be assessed from the primary beam yield using the formula:

$$Yield = e^{-x/\lambda} \tag{3.2}$$

where N_M is the number of atoms or molecules per unit volume of the absorber material. The mean free path is also linked to the "effective" total fragmentation cross section σ_{tf} as $\lambda = \frac{1}{N_M \sigma_{tf}}$. The notation "effective" reflects the fact that thick absorbers have been used in this work [45].

3.1.1 Primary beam attenuation and fragments build up

The attenuation curve of a 200 MeV/u ^{4}He beam in a water absorber is plotted in Fig. 3.1 together with the ^{3}He fragments build up.

As the ^{3}He fragments build up affects the behavior of the total Helium curve, an accurate separation of the two isotopes has to be achieved to describe also the ^{4}He behavior. ^{3}He is a neutron-deficient isotope, means only a neutron is lost in a nuclear interaction, which is then named a "non charge-changing reaction" [45]. The ^{4}He curve can be described by an

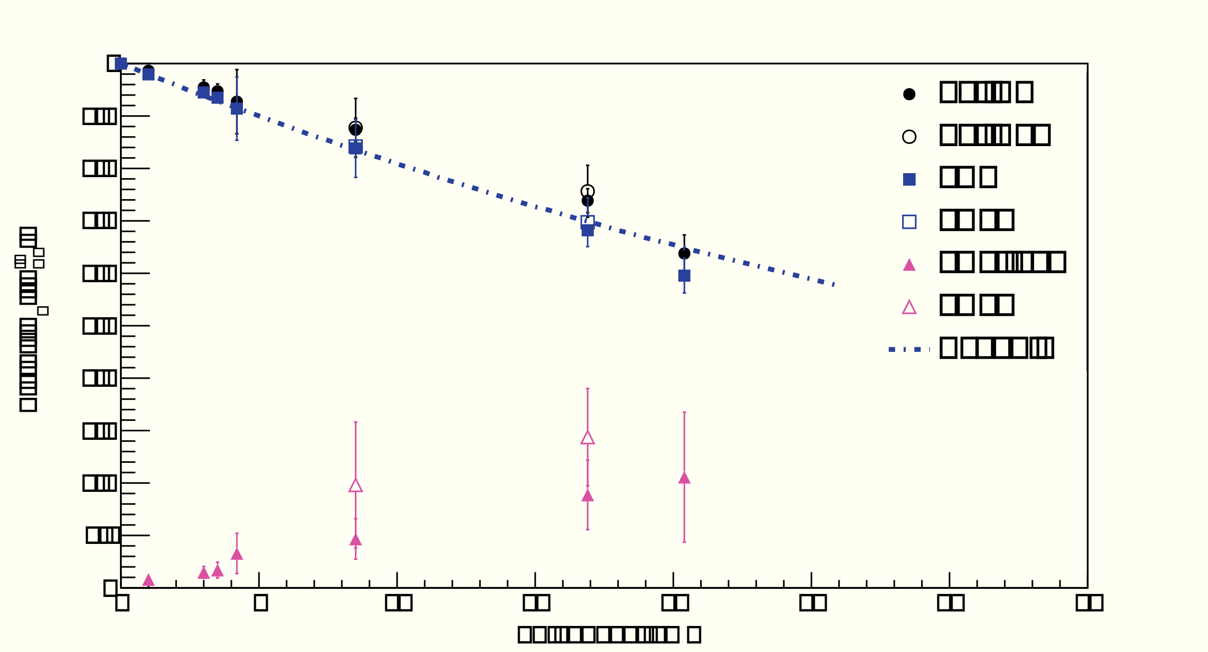

Figure 3.1.: Attenuation curve of a 200 MeV/u ^{4}He beam and build up of ^{3}He fragments as a function of depth in water. The data points plotted with an open symbol and marked with an asterisk in the legend were measured in another experiment with a similar experimental setup. The values for the ^{3}He fragments were multiplied by a factor of 5 in order to have them more visible in a linear scale.The dashed line represents the exponential fit on the primary ions curve. The point measured at around 20 cm water thickness was not included from the fit calculation because of the strong energy dependence of the fragmentation cross section close to the Bragg peak position. The attenuation of Helium ions (sum of the contributions from ^{4}He and ^{3}He particles) is also shown for comparison.

exponential function and the λ calculated from the fit parameters. The results for λ and the corresponding σ_{tf} value are reported in Table 3.1 together with predictions of two theoretical models, Kox et al. [46] and Sihver et al. [47].

	λ (g cm^{-2})	σ_{tf} (mb)
This work	47 ± 6	636±17
Sihver	37	798
Kox	39	767

Table 3.1.: Mean free path λ and "effective" total fragmentation cross section σ_{tf} for 200 MeV/u ^{4}He ions interacting with water. The error on λ was calculated by visually fitting lines with a minimum and maximum slope. This method gives a more conservative error with respect to the fit parameter error given by the standard mathematical program (12% against 5%).

A comparison between the attenuation of Helium ion in water and PMMA is shown in Fig. 3.2. The difference increases slightly with the target thickness. The λ calculated with the exponential fit for PMMA is 45±4 g/cm^2 with a corresponding σ_{tf} of 3698±336 mb. A slight difference in the survival fraction results in a large "effective" total fragmentation cross section variation, the value being higher for PMMA than water due to the much larger molecule of the polymer repeat unit.

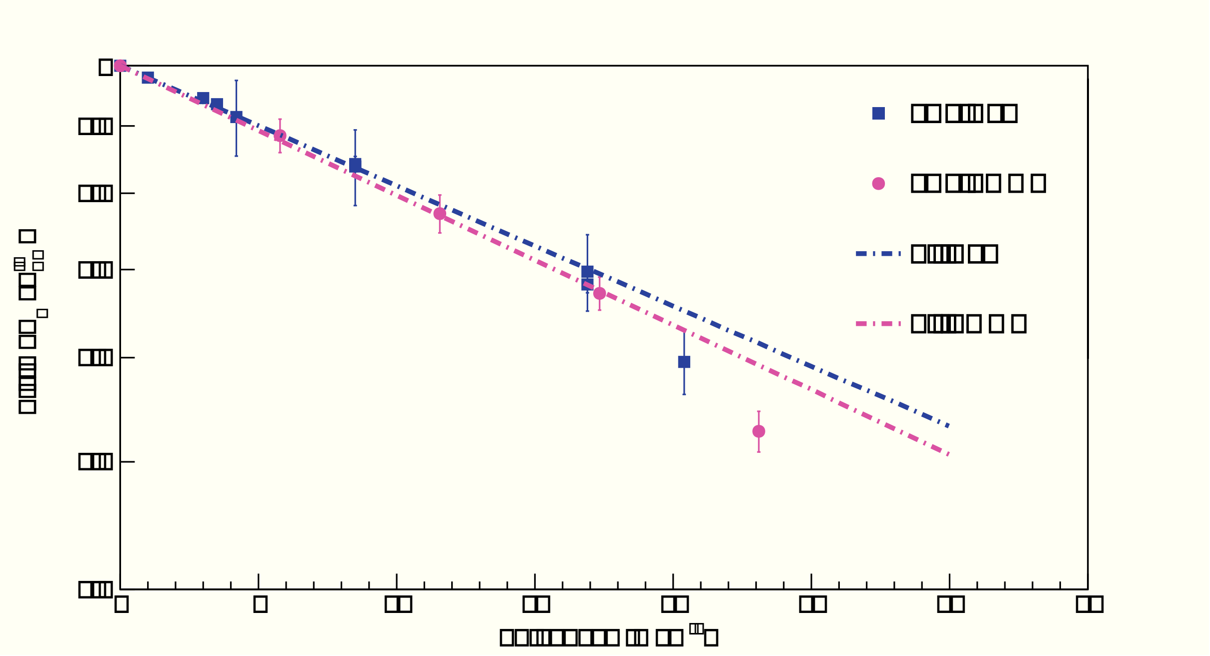

Figure 3.2.: Fit functions of the attenuation curves for a 200 MeV/u ^{4}He beam as a function of depth in water and PMMA targets.

The primary beam flux attenuation gives information on the nuclear fragmentation processes that the ions undergo to when transversing matter. The exponential behavior typically observed in the attenuation curves for carbon beams [44] was not found for Helium particles. The ^{4}He attenuation curve was described by a single exponential function after the ^{3}He contribution had been subtracted (Fig. 3.2) and the mean free path λ and the “effective” total fragmentation cross section σ_{tf} could be calculated accordingly. However, the fragmentation tail observed in the E detector (as shown in Fig. 2.9) did not allow a complete separation of the two isotopes and thus a contamination in both selections is expected.

A collection of the data available in literature reporting total charge-changing and nuclear cross sections for ^{4}He + ^{16}O and p + ^{4}He reactions is shown in Fig. 3.3. The plots indicate that no experimental measurements were ever published in the energy range of interest for this work. Thus, the σ_{tf} presented here could not be compared with any data from literature, aside from the models predictions reported in Table 3.1. Works like those performed by Auce et al. [49] and Ingemarsson et al. [50], measured total reaction cross sections at low primary beam energy (below 100 MeV/u) while values published by Webber et al. [54], Ferrando et al. [48] and Jaros et al. [55], presented total charge-changing cross sections for ions above 500 MeV/u.

The comparison of the "effective" total fragmentation cross section for ^{4}He ions (σ_{tf} = 636 mb) and ^{12}C ions (σ_{tf} = 1424 mb [20]) at the same water depth, indicates a rise with increasing ion charge due to the contribution of different reaction mechanisms (deep inelastic collisions or fusion reactions) [20]. A total of six reaction channels [1] can be listed for the production of light fragments in Helium collisions with Hydrogen and Oxygen, leading to a higher survival fraction with respect to Carbon ions [56]. At 8 cm water depth, 16% more Helium ions survive than Carbon ions [44]. At a depth of 20 cm (slightly before the Bragg peak) (65 ± 5)% of the primary Helium beam does not undergo nuclear fragmentation while only 38% of carbon ions survives [*].

The secondary fragments build up is plotted in Fig. 3.4. The multiplicity issue discussed in Sec. 2.3.2 effects mainly the protons yield. At the Bragg peak position (25.6 cm H_2O) only 15% of the fragments (normalized to the total number of incident ions) are identified as H.

---

[*] The values for ^{12}C were calculated using the λ value from Haettner et al. [44].

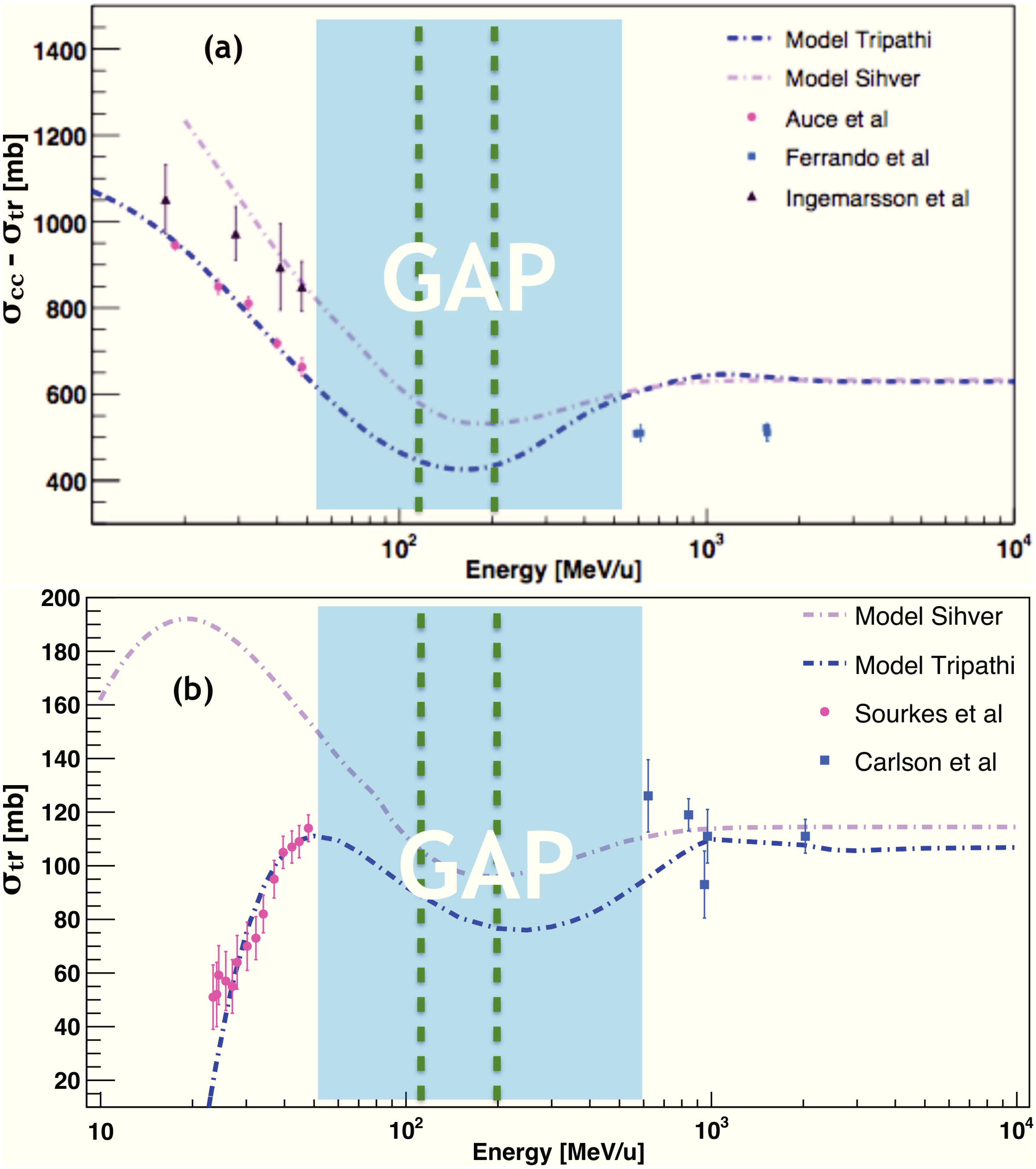

Figure 3.3.: Collection of data from literature to characterize the reactions ^{4}He + ^{16}O (a) and p + ^{4}He (b). The data points plotted in (a) are total charge-changing cross sections (Ferrando et al. [48]) and total nuclear reaction cross sections (Auce et al. [49], Ingemarsson et al. [50]). The data points shown in (b) contain total reaction cross sections measured by Sourkes et al. [51] and Carlson et al. [52]. The dashed lines represent total reaction cross sections calculated with Tripathi [53] and Sihver [47] models (calculation courtesy of M. Krämer and E. Scifoni).

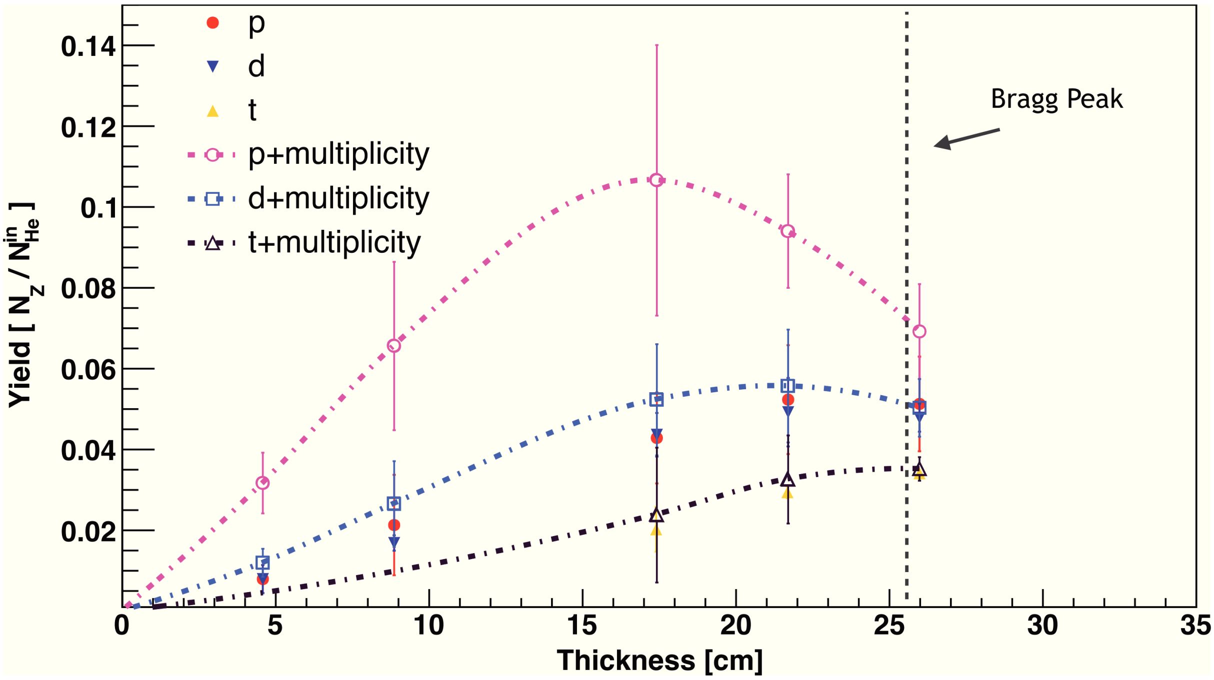

Figure 3.4.: Build up curves of protons, deuterons and tritons produced by a 200 MeV/u ^{4}He beam interacting with water as a function of the target thickness. The open symbols represent the points where the multiplicity states p+p, p+d and p+t were accounted for while the full symbols are data without multiplicity states. The dashed line is a guide for the eye.

3.1.2 Comparison with the transport calculation of TRiP98

Transport calculations performed with TRiP98 [57] are shown in Fig. 3.5. The latest version of TRiP98 [1] features a new model for therapeutic ^{4}He ions. The algorithms for describing the total reaction cross sections are based on Tripathi [53] and Sihver [47] models and the primary beam attenuation in water is calculated by modeling nuclear collisions of ^{4}He ions with protons and oxygen nuclei.

Fig. 3.5(a) shows a good agreement between the primary beam flux attenuation measured in this work and TRiP98 calculations, especially for thin targets. This result is a strong indication that even though no experimental data were available at primary beam energies between 100 and 400 MeV/u, the assumption of two-body dissociation for describing the total fragmentation cross section of light ions works pretty well. The simulated ^{3}He build up is also in good agreement with the measurements, even if the accuracy of the analysis procedure suffers from possibile misidentification in the overlap region with the predominant ^{4}He signal.

Simulated and measured build up curves for secondary H fragments are shown in Fig. 3.5(b). The agreement for protons and deuterons is good especially for target thicknesses up to 17 cm H_2O, but the model seems to significantly overestimate the tritons yield. In the proximity of the Bragg peak position, the protons and deuterons yields are also overestimated by $\sim$ 30%. This difference can be most likely explained by the fact that while TRiP98 counts particles emitted up to 90° with respected to the primary beam direction, the experimental values include only fragments within the solid angles covered by the E detector (see section 2.3.2)

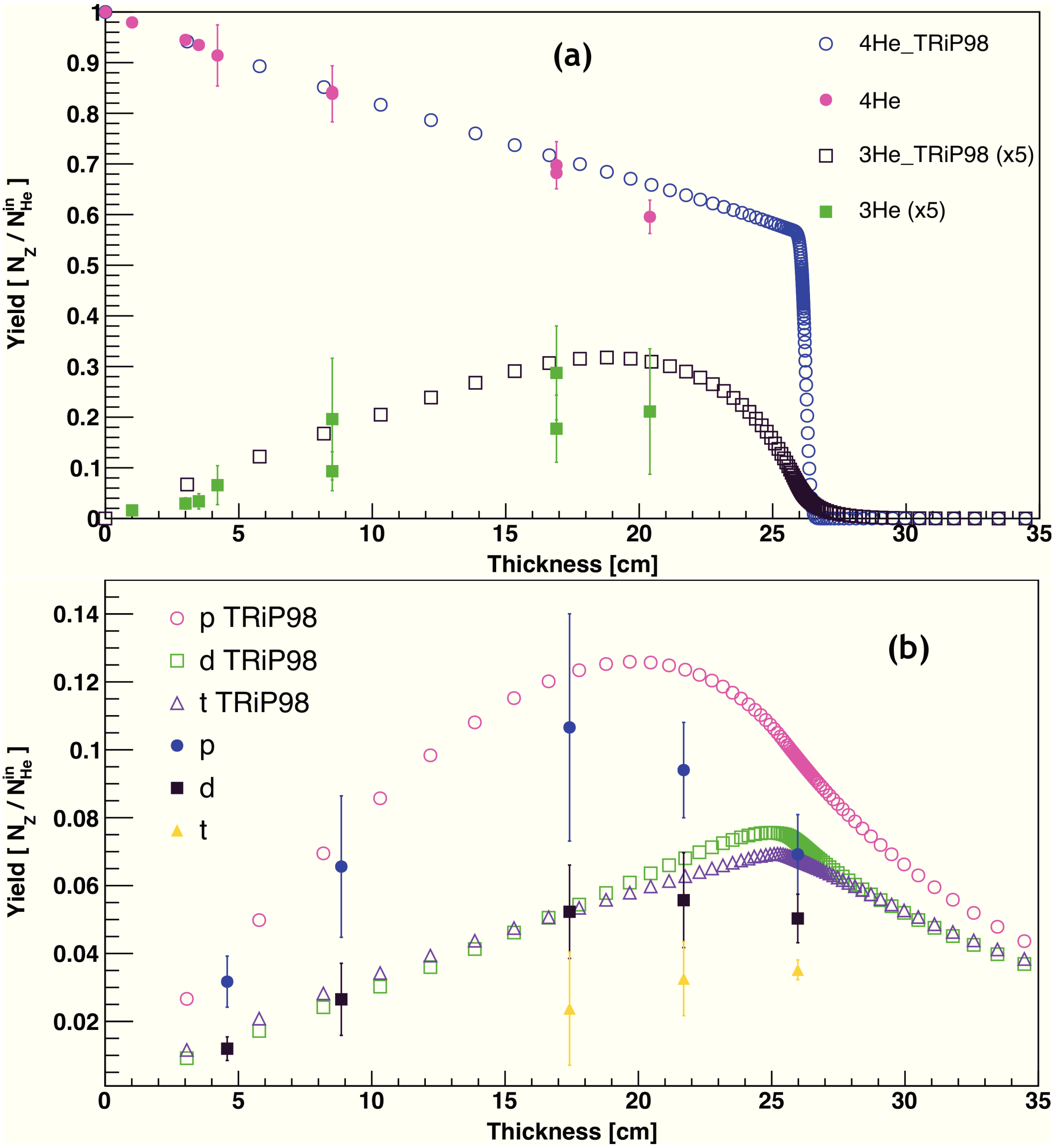

Figure 3.5.: Comparison of ^{4}He beam attenuation (a) and build up of ^{3}He (a), protons (b), deuterons (b) and tritons (b) measured (open symbols) and predicted by TRiP98 (full symbols) . All data have been published [1] but the values for the H isotopes plotted in (b) were not corrected for the multiplicity states.

3.2 Angular distributions and kinetic energy spectra

In this section, the angular distributions and kinetic energy spectra of the surviving primary ions as well as the secondary fragments are presented. An estimate of the total yield for all particle species calculated from the angular distributions is also reported.

3.2.1 Angular distributions

The angular distributions of all particle species produced by the interaction of 120 and 200 MeV/u ^{4}He beams with 4.28 and 13.96 cm H_2O targets, respectively, were measured at 0°, 2°, 4°, 6°, 8°, 12° and 23° (±0.1°). For each angle, the differential yield was calculated using the ratio between the number of a given particle type and the amount of primary ions incident on the target, normalized by the E detector solid angle.

A function $f(\theta)$ was then chosen to describe the angular distributions of each species and the total yield was calculated as:

$$Yield = 2\pi \int_0^{\theta} f(\theta)\, sin(\theta)\, d\theta \tag{3.3}$$

E	120 MeV/u					200 MeV/u				
Ion	^{4}He	^{3}He	p	d	t	^{4}He	^{3}He	p	d	t
FWHM	0.90°	3.32°	3.50°	-	-	0.98°	3.43°	4.47°	3.45°	3.94°

Table 3.2.: Widths obtained from fitting the angular distributions of all particle types with superposition of a Gaussian and exponential function. The values represent the FWHM of the Gaussian contribution.

According to Goldhaber model [58], angular distributions of light fragments are described by a single Gaussian function. However, Golovkov et al. [59] and Greiner et al. [60] proved that the H fragments distribution tails are better described by an exponential function while for Helium ions a combination of two Gaussian functions appears to be the optimal choice [59]. In this work, all angular distributions could be well described by the superposition of a Gaussian and an exponential function [44, 42, 61]. In general, the Gaussian contribution provided a better description between 0° and 4° while the exponential dominates the trend at larger angles. Nevertheless, for deuterons and tritons produced by the 120 MeV/u ^{4}He beam the exponential part appears to describe well the data behavior even at small angles.

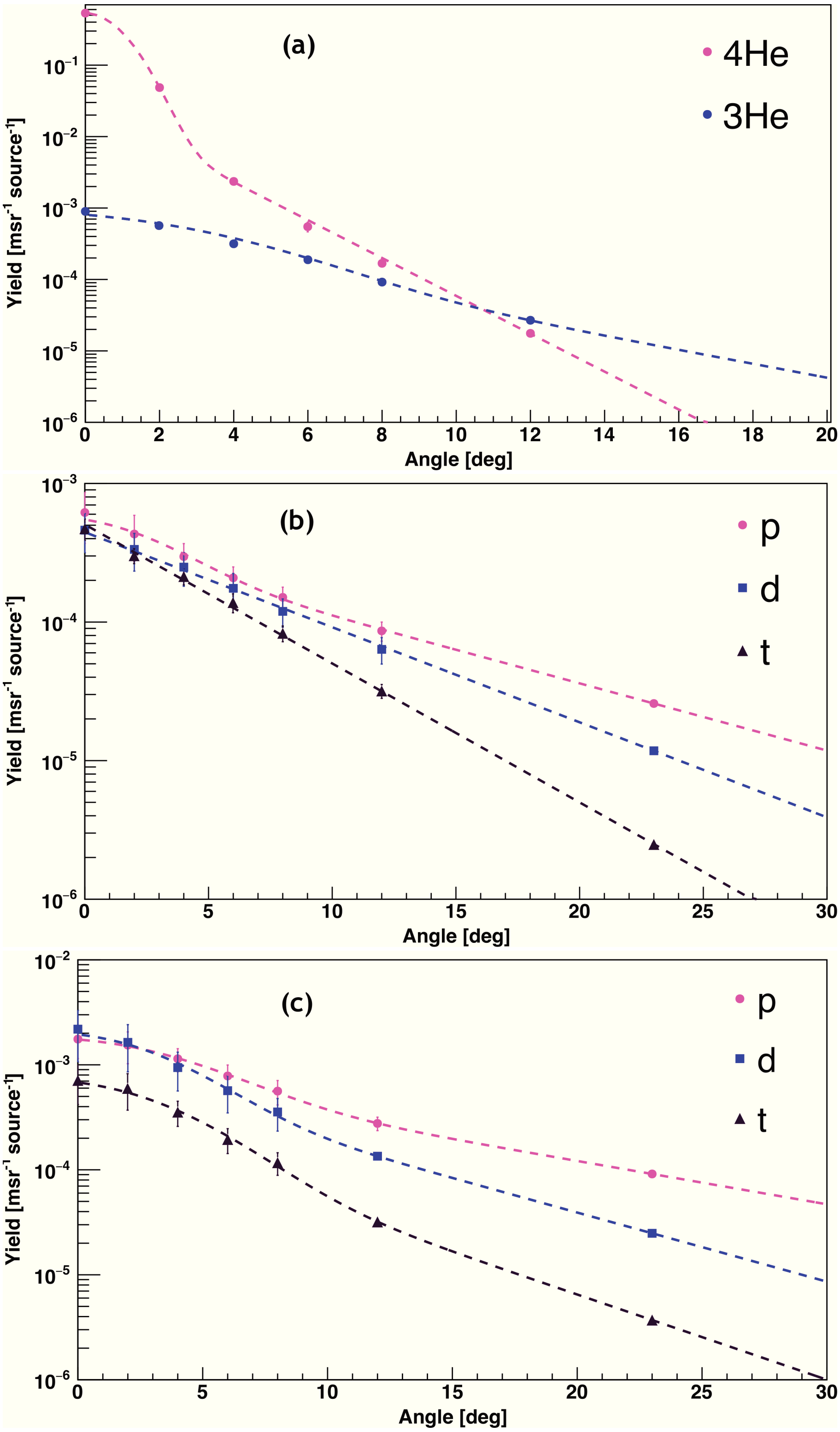

Figure 3.6.: Angular distributions of surviving primary ions and secondary fragments measured for 120 and 200 MeV/u ^{4}He beams impinging on 4.28 and 13.96 cm H_2O targets, respectively. The surviving 120 MeV/u ^{4}He ions and ^{3}He are plotted in panel while protons, deuterons and tritons are presented in panel (b). Distributions for H isotopes produced by the 200 MeV/u ^{4}He beam are shown in panel (c). The dashed lines represent the fit curves using a superposition of a Gaussian and an exponential function.

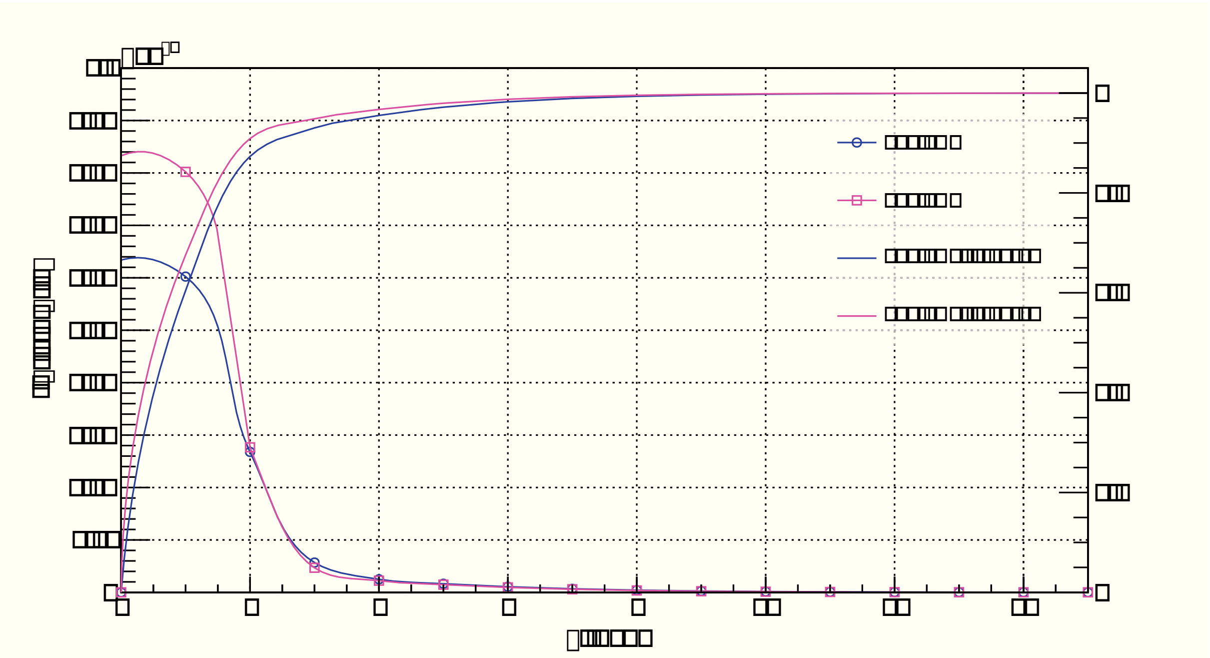

Figure 3.7.: integral function $f(\theta)sin(\theta)d\theta$ as a function of the angle for the primary ions at 120 and 200 MeV/u. The dotted lines represent the integrand (left vertical axis) whereas the dashed lines show the integral value normalized to 1 (right vertical axis)..

The angular distributions measured in this work are plotted in Fig. 3.6 while the corresponding FWHM are presented in Table 3.2.

The angular distributions of all fragments (^{3}He, p, d, t) are much broader than the primary beam. For ^{4}He ions at 200 MeV/u, the secondary protons present the broadest distribution and are the most abundant fragment type at all angles aside from 0°, where the deuteron yield is higher (see Fig. 3.6(c)). Tritons, ^{3}He and deuterons have comparable FWHM, but ^{3}He shows a steeper yield drop at increasing angle. ^{4}He particles can be detected up to 12° from their initial direction mainly because of elastic and quasi-elastic nuclear scattering in the target [32].

3.2.2 Integrated yields

The angular distributions integrals for all particle kinds were calculated using Eq. 3.3. The results are presented in Table 3.3 and the integral functions behavior as a function of the angle are displayed in Figs. 3.7 and 3.8.

The integrals were computed between 0 and two values of θ_{max}: 23° or 90°. The first range contains all data directly measured in this work while the second range includes also values extrapolated from the angular distributions fit functions extended up to 90°.

Fig. 3.7 indicates that the integral contribution for ^{4}He ions becomes negligible above 12° while all secondary particles show a much different behavior. For fragments produced at 120 MeV/u (Fig. 3.8(a)), protons are characterized by the broadest distribution with a significant contribution to the total yield above 20° (Table 3.3). All other fragments present a similar trend,

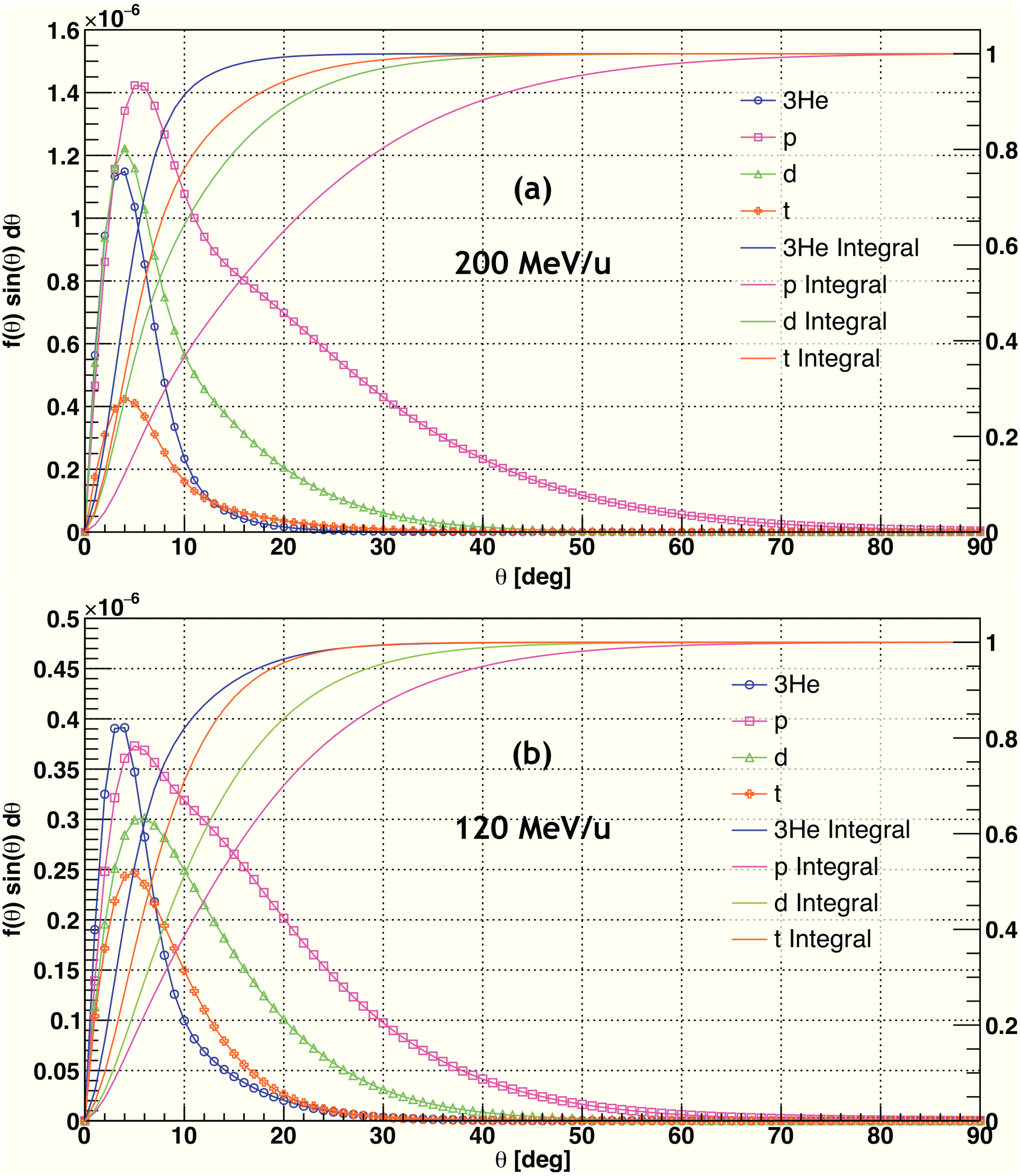

Figure 3.8.: integral function $f(\theta)sin(\theta)d\theta$ as a function of the angle for fragments produced by the 200 MeV/u (a) and 120 MeV/u (b) ^{4}He beams. The dotted lines represent the integrand (left vertical axis) whereas the dashed lines show the integral value normalized to 1 (right vertical axis).

although their yield starts dropping at different angles (30° for tritons and ^{3}He versus 40° for deuterons).

The distribution of the fragments produced by the 200 MeV/u ^{4}He beam (Fig. 3.8(a)) behave in a similar way. Protons have an even broader distribution respect all other fragments types, their yield is always the highest and their contribution between 23° and 90° is 30% of their total yield (Table 3.3). Deuterons, tritons and ^{3}He integrals rise to 1 around 45° and their distributions appear slightly broader than the ones for the 120 MeV/u data set (Fig. 3.8(a)).

The integrals on regions above 23° are clearly affected by the uncertainty on the fitted function slopes. Measurements at larges angles should be performed in future experiments in order to validate these estimate and improve the data accuracy.

E	**120 MeV/u**					**200 MeV/u**				
Ion	**^{4}He**	**^{3}He**	**p**	**d**	**t**	**^{4}He**	**^{3}He**	**p**	**d**	**t**
Yield$_{0°}^{90°}$	0.82	0.024	0.054	0.034	0.018	0.66	0.049	0.20	0.093	0.026
Yield$_{0°}^{23°}$	0.82	0.0238	0.042	0.030	0.017	0.66	0.049	0.14	0.085	0.025
Diff	-	2%	23%	11%	3%	-	-	30%	9%	4%

Table 3.3.: Integrated yield of all angular distributions between 0° and 23° and between 0° and 90°.

Total yield versus integrated yield for 200 MeV/u ^{4}He ions

The integrated angular yield have been compared with the total yield measured from the attenuation and build up experiment (Section 3.1.1). For a correct comparison, the integral was estimated over the same angular range of the attenuation measurement (between 0° and 23°). The results for the H fragments are presented in Table 3.4, where the yield without multiplicity states are reported as well.

	p	d	t
Total yield	0.034	0.032	0.012
Total yield $_{Corr}$	0.095	0.045	0.015
Integrated yield	0.14	0.085	0.025

Table 3.4.: Comparison between the total yield calculated from the attenuation measurements and the integrated yield estimated from the angular distribution integral. Yield$_{Corr}$ is the total yield corrected for the multiple states. The latter and total yield have been calculated from the polynomial function selected for fitting the experimental data.

The comparison between the integrated yield and the total yield indicate that the largest discrepancy between the two approaches stems from the multiplicity problem discussed in Section. 2.3.2. Nevertheless, even when the correction is applied, the differences between total yield$_{Corr}$ and integrated yield are 32%, 47% and 40% for p, d and t, respectively. A possible source of this deviation are the error bars on the attenuation measurements, which are as high as ± 30%. For this reason, the angular distribution method is found to be more accurate for studying the fragments build up.

For the 200 MeV/u primary ^{4}He beam, instead, the integrated yield results to be 10% lower than the survival fraction measured in the attenuation experiment. This discrepancy was associated to the convolution effect [62] coming from the BaF$_2$ detector size, which results in a broadening of the measured distribution compared to the “real one” . In this measurement, the convolution effect of the detector is enhanced because the FWHM of the primary beams profile (see Table 3.2) is comparable to the angular acceptance of the detector (± 1°) itself. Therefore, a de-convolution procedure was applied in order to estimate this effect.

It is assumed that

$$f_{conv}(\theta) = f_{real}(\theta,\phi) \ * \ g(\theta,\phi) \tag{3.4}$$

where $f_{conv}(\theta)$ is the function representing the measured angular distribution, $f_{real}(\theta,\phi)$ is the real distribution without the detector effect - the one that needs to be estimated - and $g(\theta,\phi)$ is a 2D radial symmetric step function used to represent the geometry of the detector. This function can be written as:

$$g(\theta,\phi) = \begin{cases} 0 & \text{if } \theta > 1^{\circ} \\ 1 & \text{if } \theta \geq 1^{\circ} \end{cases} \tag{3.5}$$

However, the presence of ϕ indicates a 2D convolution performed over the area of the detector that was assumed to have a circular shape. Fig. 3.9 shows a schematic drawings for the 2D integration over the detector area.

The function f_{real} is then optimized in a way that f_{conv} best fits the data points. The results of the de-convolution method applied to ^{4}He at 120 MeV/u is represented in Fig. 3.10. For this case an increase of 10% of the integrated yield was calculated. Same procedure was applied to 200 MeV/u ^{4}He beam for which an increase of 8% of the integrated yield was found, decreasing the discrepancy to only 2%. The latter can be associated to a not perfect separation between ^{3}He and ^{4}He, due to the fragmentation process occurring in the BaF$_2$ detector itself. This "pollution" has been estimated to decrease the ^{4}He counts of around 1-2% and thus the agreement of the two independent measurements (attenuation versus angular distribution) can be considered adequate.

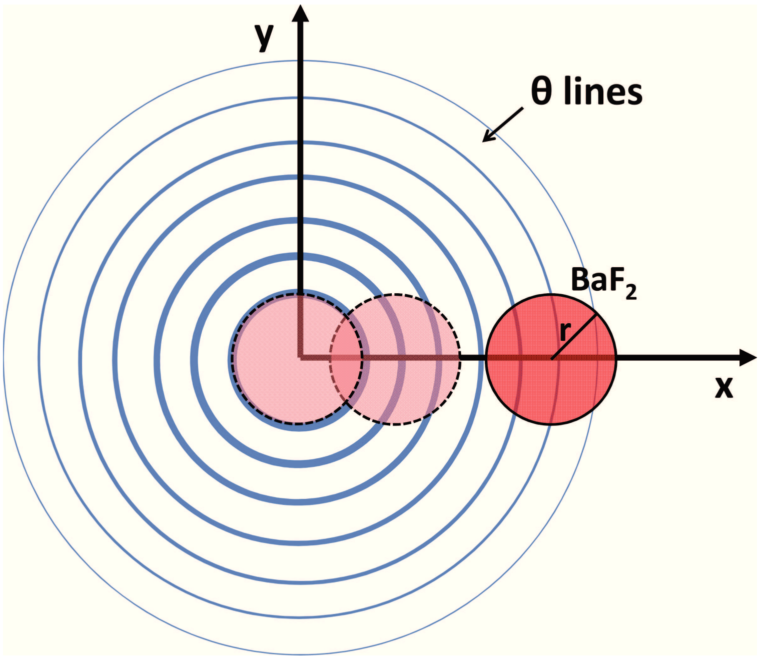

Figure 3.9.: Schematic drawings of the 2D integration over the detector area. The z axis (beam direction) is perpendicular to the paper. The hexagonal shape of the BaF_2 detector was approximated to its inscribed circle of radius (r) 4.5 cm and it is represent by the red circular shape. The θ lines represented the iso-lines of the f_{real} function assuming a symmetric radial distribution. The BaF_2 detector is shifted along the x-axis (dashed circles) at each angle covered during the experiment and the integral over the θ lines is numerically performed.

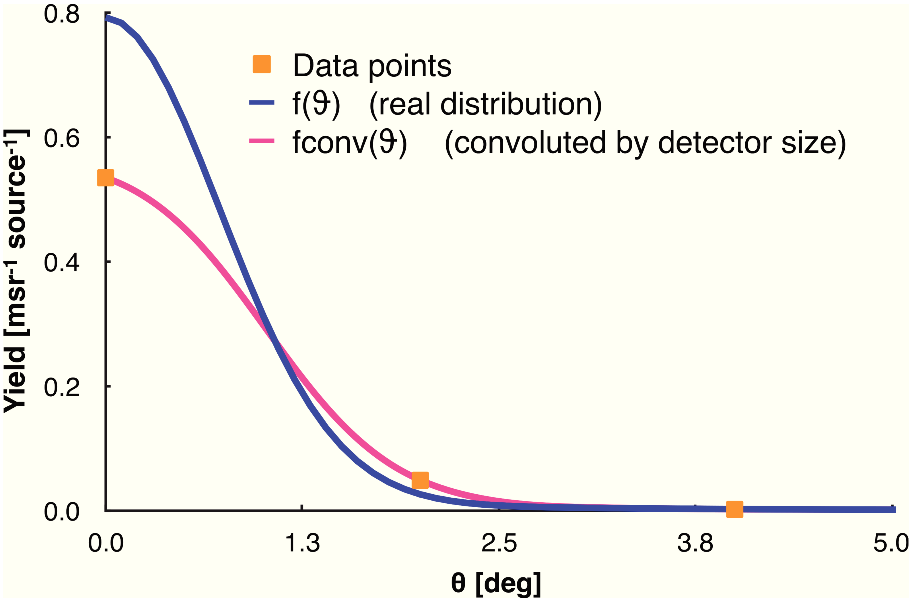

Figure 3.10.: Comparison between the convoluted and de-convoluted distribution of ^{4}He 120 MeV/u. The effect is pronounced at forward angles so that the data points above 5° are not shown. The symbols represents the data points presented in Fig. 3.6(a) together with the fitted function (pink full line). The effect of the convolution for the case represented in this figure was estimated to be 10%.

	200 MeV/u		120 MeV/u	
Ion	Yield	P	Yield	P
p	0.20	20	0.05	5
d	0.10	10	0.03	3
t	0.03	3	0.02	2
^{3}He	0.05	10	0.02	4
Sum		43		14
^{4}He	0.74		0.91	
^{4}He $_{lost}$	0.26	52	0.09	18
Sum		52		18
Difference		9		4
Diff %		20%		13%

Table 3.5.: Comparison between the number of protons leaving the target and the number of protons entering the target for 100 incoming primary ions. P indicates the total number of protons (single or as a part of a heavier fragments). The yield of ^{4}He ions at 200 MeV/u was taken from the attenuation curve, instead the yield of ^{4}He ions at 120 MeV/u was taken by the integral of the angular distribution corrected by the filter function.

Consistency of the integrated yield

A self-consistency method was applied to the integrated yield to understand if the results were reasonable. In order to do so, a rough calculation of the nucleons number conservation before and after a reaction was performed. In particular, all protons (single or part of a heavier fragment) were counted.

The number of protons detected after the target (N_p^{out}) was determined and compared to the number of protons before the target (N_p^{in}), assessed from the survived ^{4}He. N_p^{in} was estimated in the following way: at 13.96 cm H_2O, the S.f. of ^{4}He is 0.7, i.e. if 100 ^{4}He ions entered the target 70 survived and 30 fragment or, in other words, $30*2=60$ protons formed a lighter nucleus (0.3 protons/^{4}He). N_p^{out} was simply counted as the number of protons (singles or as a part of d, t and ^{3}He nuclei) of the produced fragment species. The results of this calculation are reported in Table 3.5. The integrated yield of the fragments seem to be underestimated by 20% and 13% for 200 MeV/u and 120 MeV/u ^{4}He beams, respectively.

3.2.3 Kinetic energy spectra

The kinetic energy spectra for the primary ions as well as secondary fragments were estimated from the TOF measurements. For every particle species and every angle the kinetic energy were calculated through Eq. 2.3 (Section 2.3.3). A selection of the measured spectra is presented in this section while the remaining can be found in Appendix C.

In Fig. 3.11 the energy distributions of 120 (a) and 200 MeV/u (b) ^{4}He ions at different angles are plotted. The distribution at 0° peaks at 130 MeV/u ± 10% for the 200 MeV/u beam and at 84 MeV/u ± 7% for 120 MeV/u beam. The mean values were compared with the predictions from LISE ++ program and found to be in agreement within 1% and 4%, respectively. In Fig. 3.12 the spectra of the fragments produced by 200 MeV/u ^{4}He ions are presented. At small angles (4 ° in Fig. 3.12(a)), ^{3}He are characterized by a peak distribution centered at the residual primary beam energy while all hydrogen isotopes (Fig. 3.12(b)(c)(d)) have much broader spectra extending higher energies than the one of the primary ^{4}He beam. All distributions move to lower energies and become broader with increasing angle. Especially protons have a distinct broad distribution reaching energies up to almost twice the primary beam energy. This phenomenon has been already observed by Hättner et al. [44] and Gunzert-Marx et al. [42] and is associated to the Fermi momentum [63] transferred by a nucleus to a fragment. In Fig. 3.13 the spectra of ^{3}He, p, d and t produced by 120 MeV/u ^{4}He beam are plotted. The data follow a similar behavior as described for the 200 MeV/u dataset. In this case, deuterons and tritons spectra have a more narrowed distribution than protons, for which the Fermi momentum gives a significant energy boost.

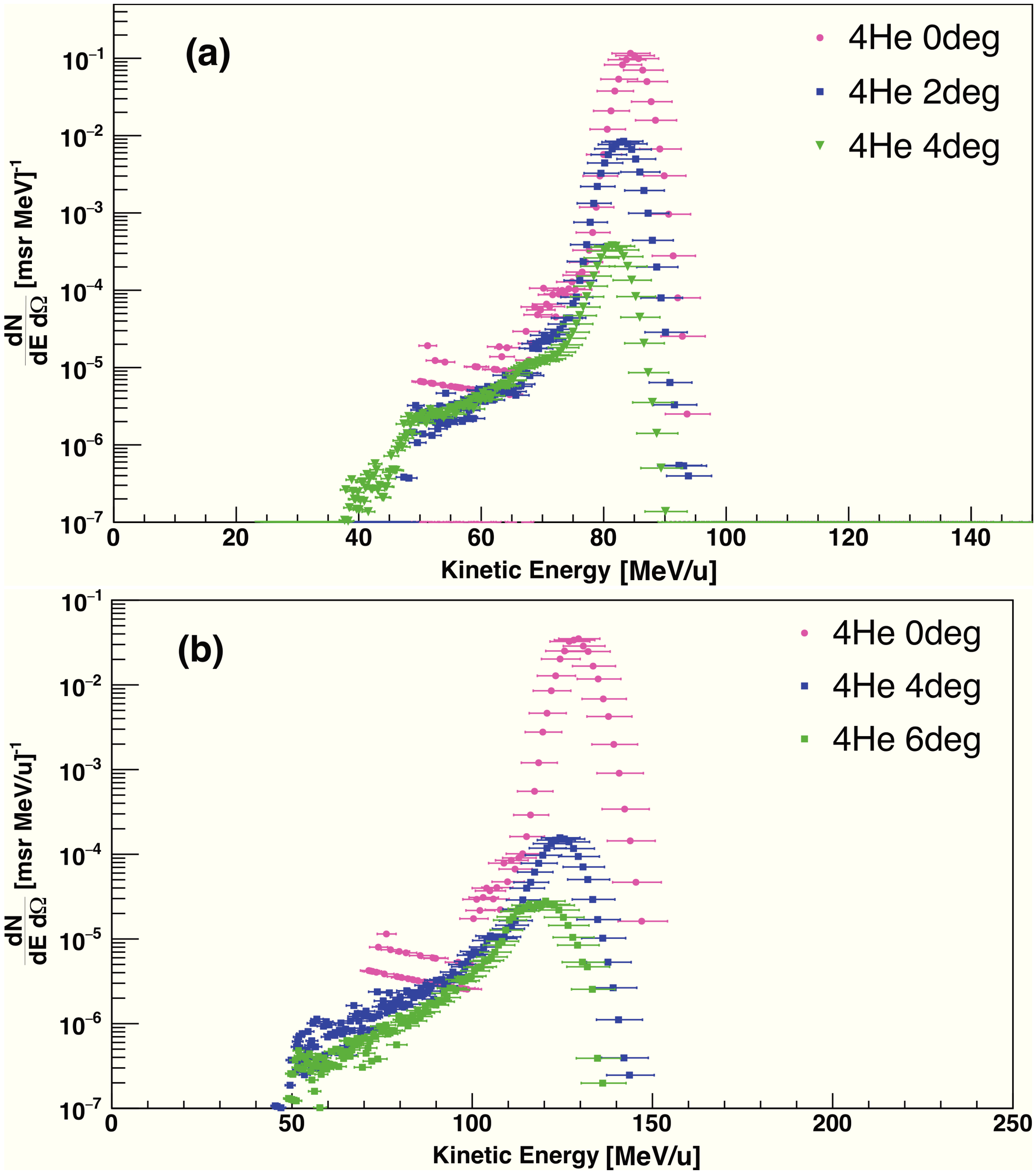

Figure 3.11.: Kinetic energy spectra of ^{4}He ions with initial energy of 200 MeV/u impinging 13.96 cm H_2O (a) and 120 MeV/u impinging on 4.28 cm H_2O (b)

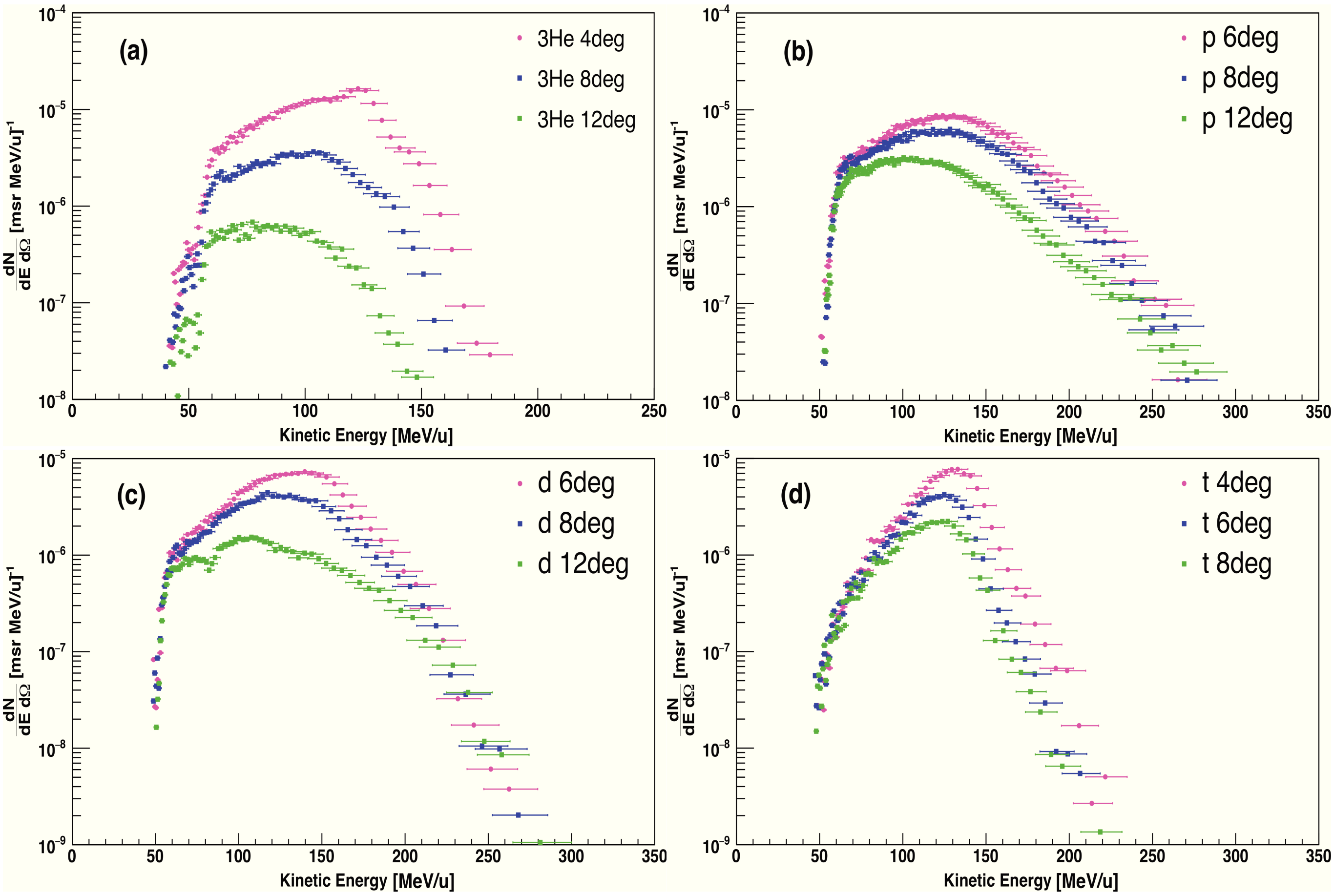

Figure 3.12.: Kinetic energy spectra of secondary fragments produced by ^{4}He ions with initial energy of 200 MeV/u impinging on 13.96 cm H_2O.

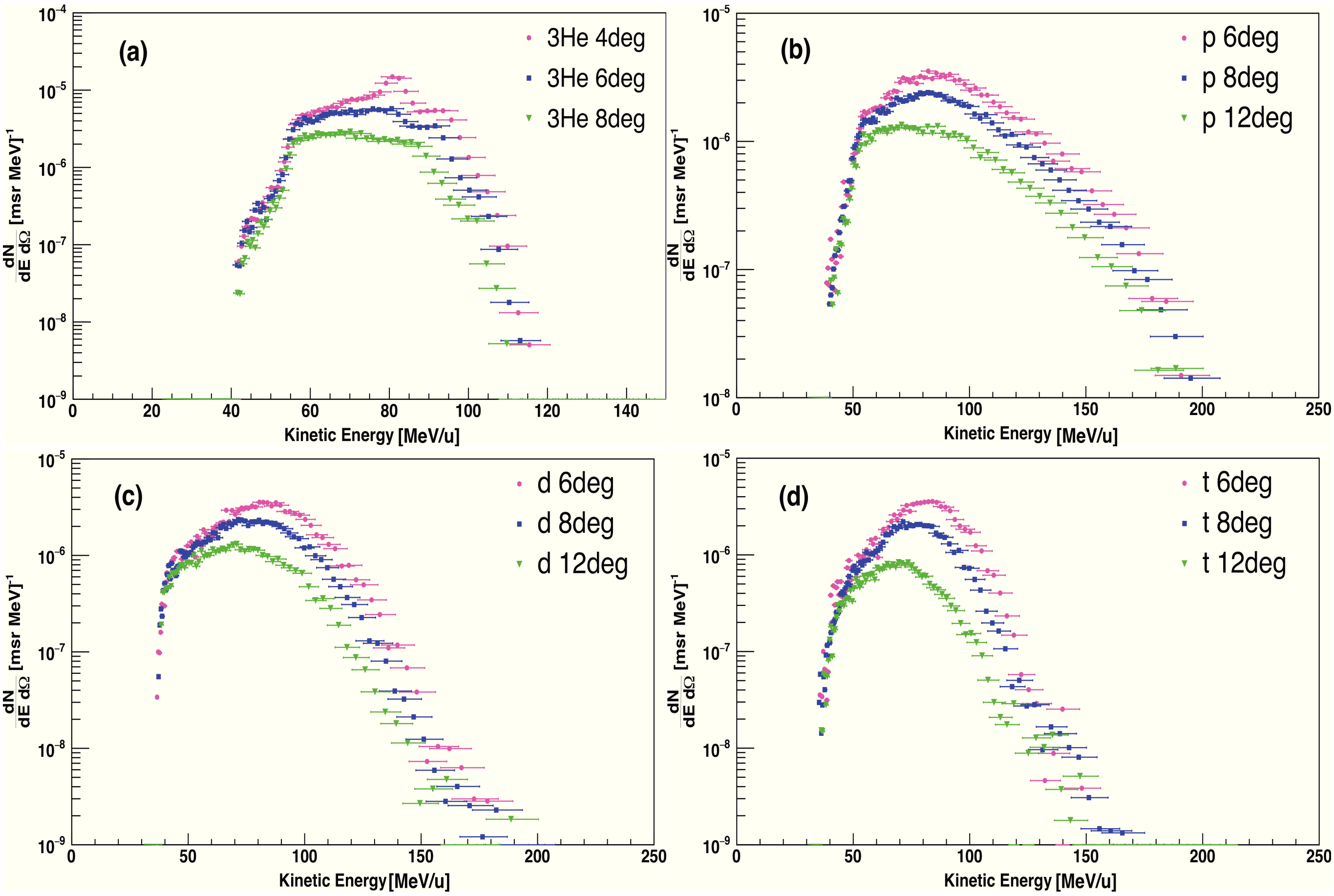

Figure 3.13.: Kinetic energy spectra of secondary fragments produced by ^{4}He ions with initial energy of 120 MeV/u impinging on 4.28 cm H_2O.

3.3 Scattering in water and radial dose distribution of 120 and 200 MeV/u ^{4}He beams

In this section the study on the lateral scattering and the radial dose in water of 120 and 200 MeV/u ^{4}He is presented (see Section 2.3.4).

The lateral dose profile of the scattered beams in water has been fitted with the sum of a Gaussian and a Rutherford function following Bellinzona et al. [64] approach, where the effects of multiple scattering at small angles and of single nuclear scattering at large angles are taken into account. The Gaussian contribution describes multiple Coulomb scattering following Moliére theory while the Rutherford hyperbolic function describes the tail mainly due to nuclear interactions.

The lateral dose measurement was performed at 0° and then angles until 20° have been scanned and the lateral dose profile measured. The results of the radial dose profile was then compared to the angular distribution presented in Section 3.2.1 converted in dose. The radial dose profile was then parametrized with a function that best described the halo of the distribution and a comparison with the proton's radial dose distribution was performed. The latter have been measured at the same time of the measurements presented in this work with the same experimental setup.

3.3.1 Lateral beam profile

Measurements of the lateral beam profile for 120 and 200 MeV/u ^{4}He beams have been performed using EDR2 films and the PTW 2D array detector as described in Section 2.3.4. A comparison of the distributions acquired with the two detectors is shown in Fig. 3.14. The agreement on the halo region is reasonable, even though the film background is higher because of a slight asymmetry in the profile. The latter appears narrower in the film because the 2D array was position 20 cm downstream of it. As the two setups provide very similar values, from now on only the PTW detector results are presented and discussed.

The function used to fit the beam profile is:

$$f(x) = N\left((1-W)\frac{1}{\sqrt{2\pi\sigma}}\left[-\frac{x^2}{2\sigma^2}\right] + W\frac{2b^{3/2}}{\pi}\frac{1}{x^2+b^2}\right) \tag{3.6}$$

where σ is the width of the Gaussian distribution, W a relative weight, N a normalization factor and b represents the horizontal shift of the hyperbolic function [64].

The results reported in Fig. 3.15 prove that a simple Gaussian function cannot fully describe the data behavior, as it underestimates the single scattering contribution in the tails. Adding the hyperbolic Rutherford contribution solves this issue. The fit parameters of the Gaussian-Rutherford function are reported in Table 3.6.

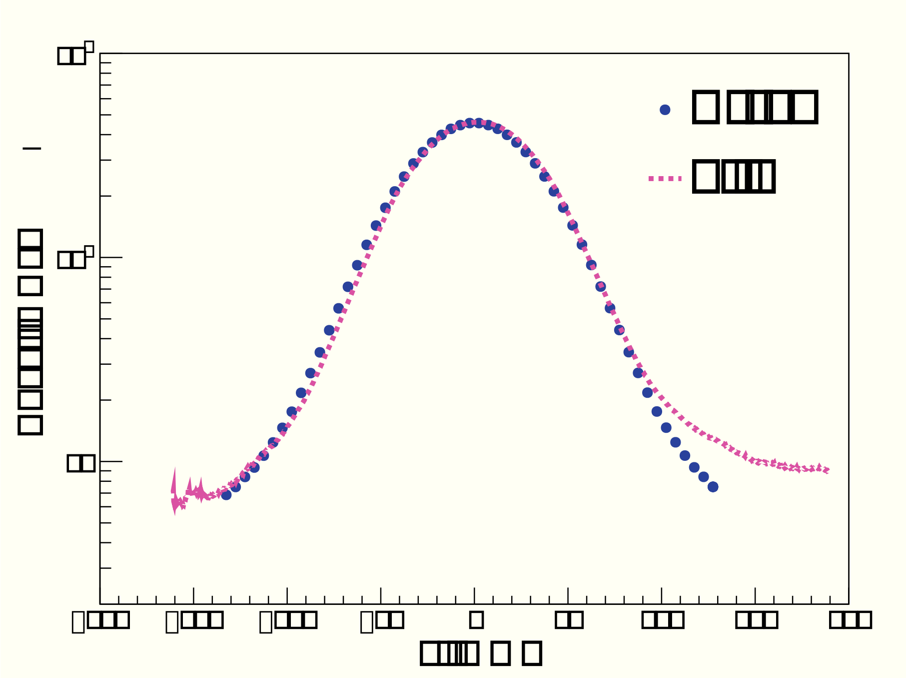

Figure 3.14.: Comparison between EDR2 film and PTW detector measurements for 200 MeV/u ^{4}He impinging on the 13.96 cm H_2O target.

E_{beam}	N	W	σ	b
120 MeV/u	10681	0.90	28.2	5794
200 MeV/u	8242	0.95	32.8	9572

Table 3.6.: Fit parameters of the Gauss-Rutherford function describing the lateral dose profile for 120 and 200 MeV/u ^{4}He beam impinging on 4.28 cm H_2O and 13.96 cm H_2O targets, respectively. N represents a normalization factor, W a relative weight, b the horizontal shift of the hyperbolic function and σ the width of the Gaussian contribution.

FWHM of 65.9 ± 0.2 mm and 77.00 ± 0.04 mm were found for the 120 and 200 MeV/u beams, respectively. For comparison, a measurement with no target at the same distance results in a FWHM of 22.00± 0.03 mm at 120 MeV/u and 13.80±0.03 mm at 200 MeV/u.

The measured lateral beam spreadings were compared with the predictions from the analytical beam transport program Scattmann (see Section 2.2), where all the nozzle components were included and the experimental setup reproduced. The results are reported in Table 3.7.

3.3.2 Conversion of double differential yield to dose

The double differential yields presented in Section 3.2 were converted into dose to assess the contribution to the total dose of all the secondary fragments. To evaluate the accuracy of this approach, measurements of dose distributions at 0°, 2°, 4°, 6°, 8°, 12° and 23° with respect to

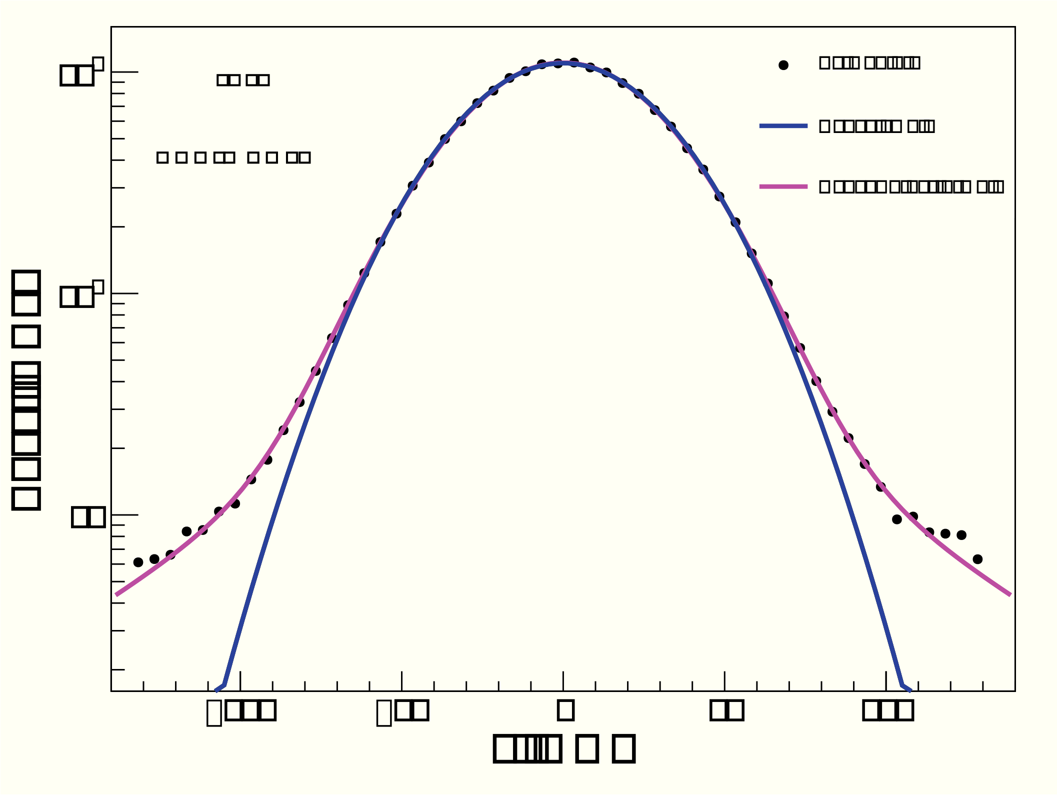

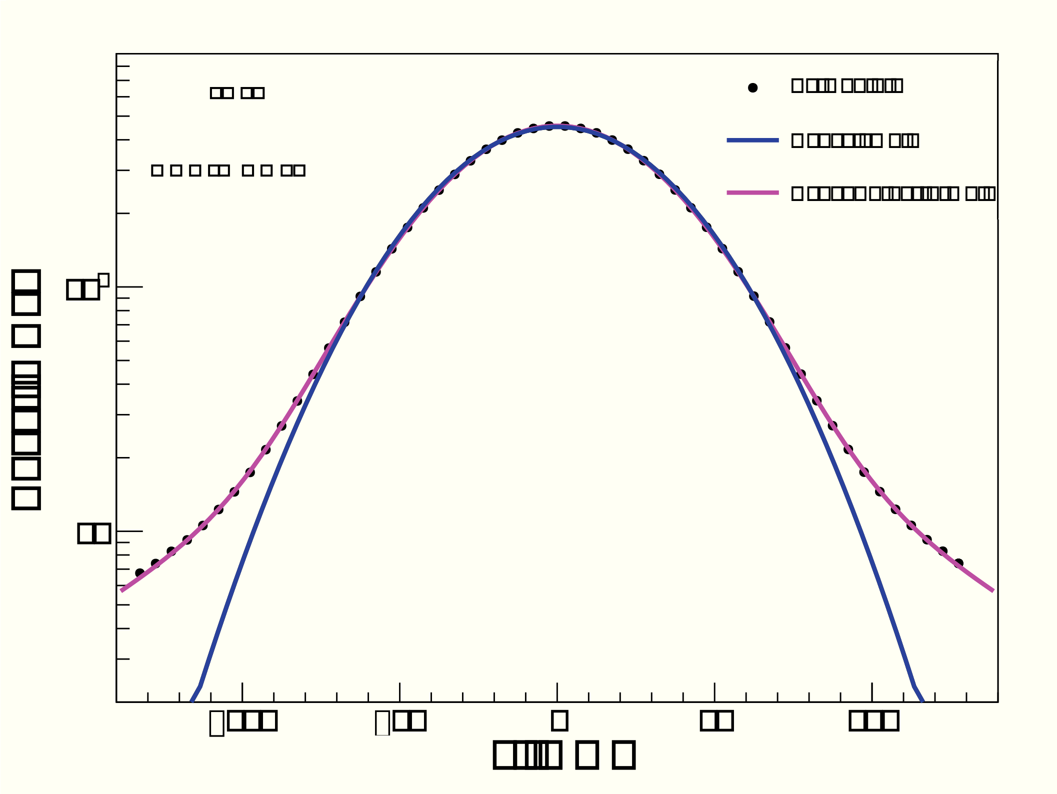

Figure 3.15.: Lateral dose profile measured with PTW detector of ^{4}He beams impinging on water targets described by a simple Gaussian approach and a Gauss+Rutherford function. (a) shows the profile of 120 MeV/u impinging on 4.28 cm H_2O target and (b) the profile of 200 MeV/u impinging on 13.96 cm H_2O target.

	120 MeV/u	200 MeV/u
FWHM_{Exp}	68.93	82.26
FWHM_{Scat}	67.23	85.2

Table 3.7.: Comparison between experimental and calculated widths of the dose profile distribution for 120 and 200 MeV/u ^{4}He beams after transversing 4.28 cm H_2O and 13.96 cm H_2O targets, respectively. The simulated value were obtained with Scattmann. The values are reported in mm.

the primary beam direction were collected with the PTW detector. All experimental conditions set for the double differential yields measurements (beam energy, targets, distances...) were exactly reproduced during this experiment. The fluence of each fragment type was translated into dose according to the following relation:

$$D[Gy] = 1.6 \cdot 10^{-10} \cdot F[cm^{-2}] \cdot \frac{dE}{dx}\left[\frac{MeV}{cm}\right] \cdot \frac{1}{\rho}\left[\frac{1}{gcm^{-3}}\right] \tag{3.7}$$

Every kinetic energy spectrum was converted into energy loss and integrated over the whole range. For a given angle θ, the dose can be expressed as:

$$D(\theta) = \frac{1}{\rho} \cdot \sum_i F(E_i, \theta) \cdot \frac{dE}{dx}(E_i) = \frac{1}{\rho} \cdot \sum_i \frac{d^2N}{dEd\Omega}(E_i, \theta) \cdot \frac{\Delta\Omega}{A} \cdot \Delta E_i \cdot \frac{dE}{dx}(E_i) \tag{3.8}$$

where i is the energy bin, ΔE_i the bin width of the kinetic energy spectra, $\left(\frac{dE}{dx}\right)_i$ the calculated energy loss, $\frac{dN_i}{dEd\Omega}$ the double differential yield and $\frac{\Delta\Omega}{A}$ the ratio between the solid angle and the area of the BaF_2 detector. The quantity $\left(\frac{dN_i}{dEd\Omega} \cdot \frac{\Delta\Omega}{A}\right)$ represents the fluence of each particle type.

The results were compared with the 2D array measurements. The dose was scaled for the distance from the center of the target to the detector (r^2). The results for 120 and 200 MeV/u ^{4}He beams are reported in Fig. 3.16(a) and (b), respectively.

The agreement between the two independent measurements is relatively good. The surviving ^{4}He ions deposit most of the dose between 0° and 4° but become less predominant at larger angles, where the fragments contribution is more significant. The distribution for ^{4}He at 200 MeV/u drops more abruptly than at 120 MeV/u, where at 6° most of the energy is still deposited by the primary ions. The contribution from protons at large angles is more significant at 200 MeV/u than at 120 MeV/u.

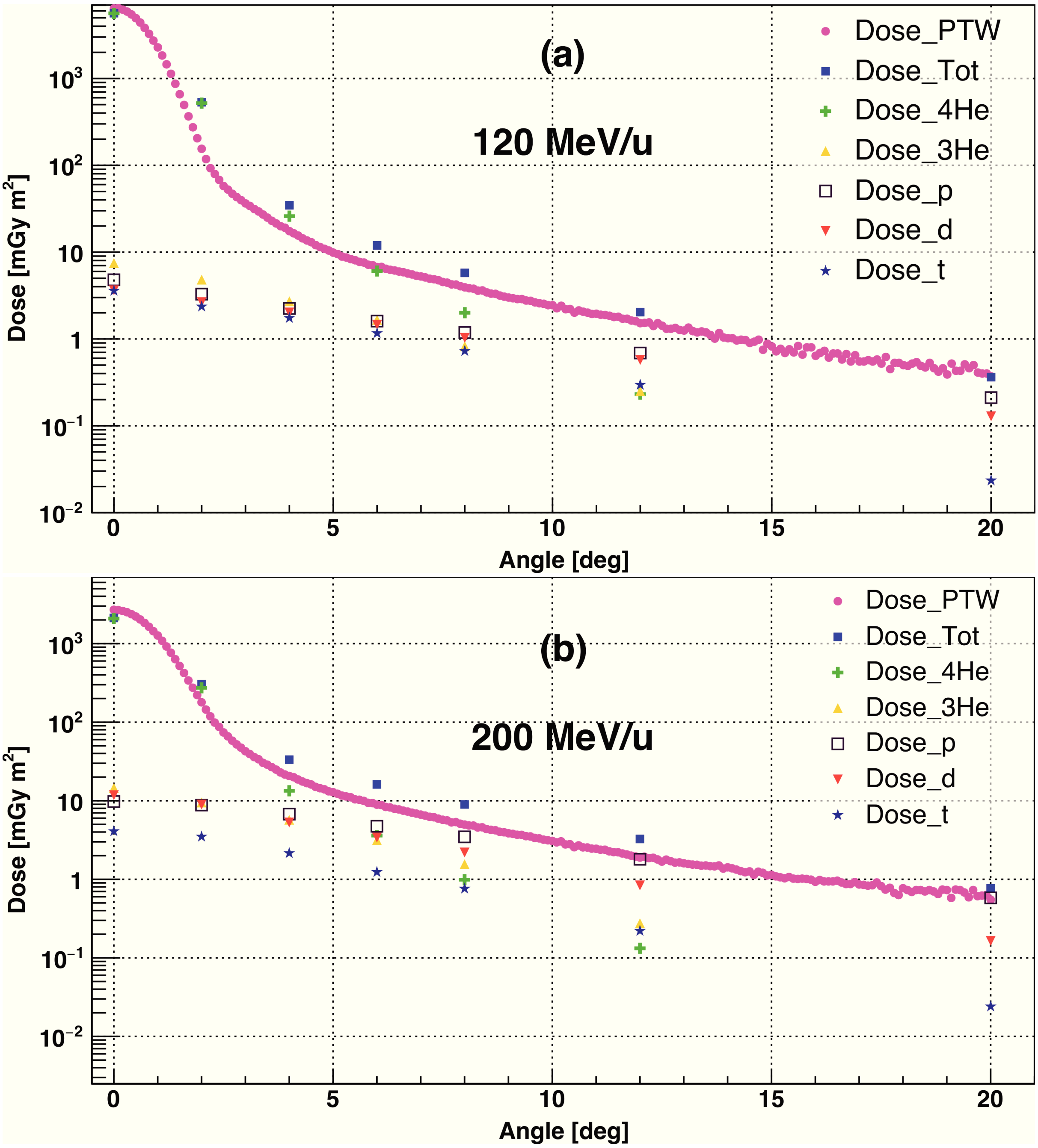

Figure 3.16.: Comparison between the dose measured with the 2D array and estimated from the double differential yield at angles between 0° and 23°. The "Dose_Tot" represents the sum of all fragments contribution at each angle. Results for 120 MeV/u ^{4}He interacting with a 4.28 cm H_2O target (a) and 200 MeV/u ^{4}He interacting with a 13.96 cm H_2O target (b).

3.3.3 Parametrization of the radial dose distribution

In the past, the radial dose distribution of the therapeutic beam was parametrized with a simple Gaussian function. Nowadays, some treatment planning systems use a double Gaussian approach but some still use a simple Gaussian distribution. The latter aims to best describe the core of the distribution up to a maximum 5° of the beam angular aperture, where the most contribution of the dose lays. Recently a great effort is devoted to enhance the accuracy of the parametrization in order to describe the halo of the beam mainly caused by nuclear interactions [64].

In order to understand the importance of a good parametrization for Helium beams a fit of the radial distribution presented in Fig. 3.16 was performed. The same analysis was done for the radial dose distribution of 120 and 200 MeV protons beams, measured in the same manner of the Helium measurements presented in this thesis.

Fig. 3.17(a) and (b) show the fit of the radial dose distribution for 200 MeV/u ^{4}He and protons, respectively. The Gauss-Rutherford approach used in Section 3.3 was replaced by a double Gauss + exponential function (later referred as "Total Fit"), in order to better describe the large halo of the distribution. The simple Gaussian fit was performed for comparison.

Fig. 3.18 shows the integral of the Total Fit function extended up to 50° and the integral of the Gauss fit function. In Fig. 3.18(a) it is possible to observe how Helium ions raise faster than protons at very forward angles (up to 2°), but slower between 5° and 10°. This is because of the contribution of secondary fragments produced by the ^{4}He ions, how can be seen in Fig. 3.16. However at this beam energy, the proton's integral raises to 1 above 40°, while the Helium's integral slightly after 20°. Same discussion can be made for Fig. 3.18(b) where the behavior of the Helium beam is more pronounced. In this case the contribution of the secondary fragments seem to be more significant between 3° and 10°.

It is possible to observe how the single Gaussian approach significantly underestimates the dose distribution for angles already bigger than 1°.

In Appendix D the effect of the shape of the lateral profile on the dose distribution from a scanned field was studied and a comparison between a gaussian beam profile and the real one was made.

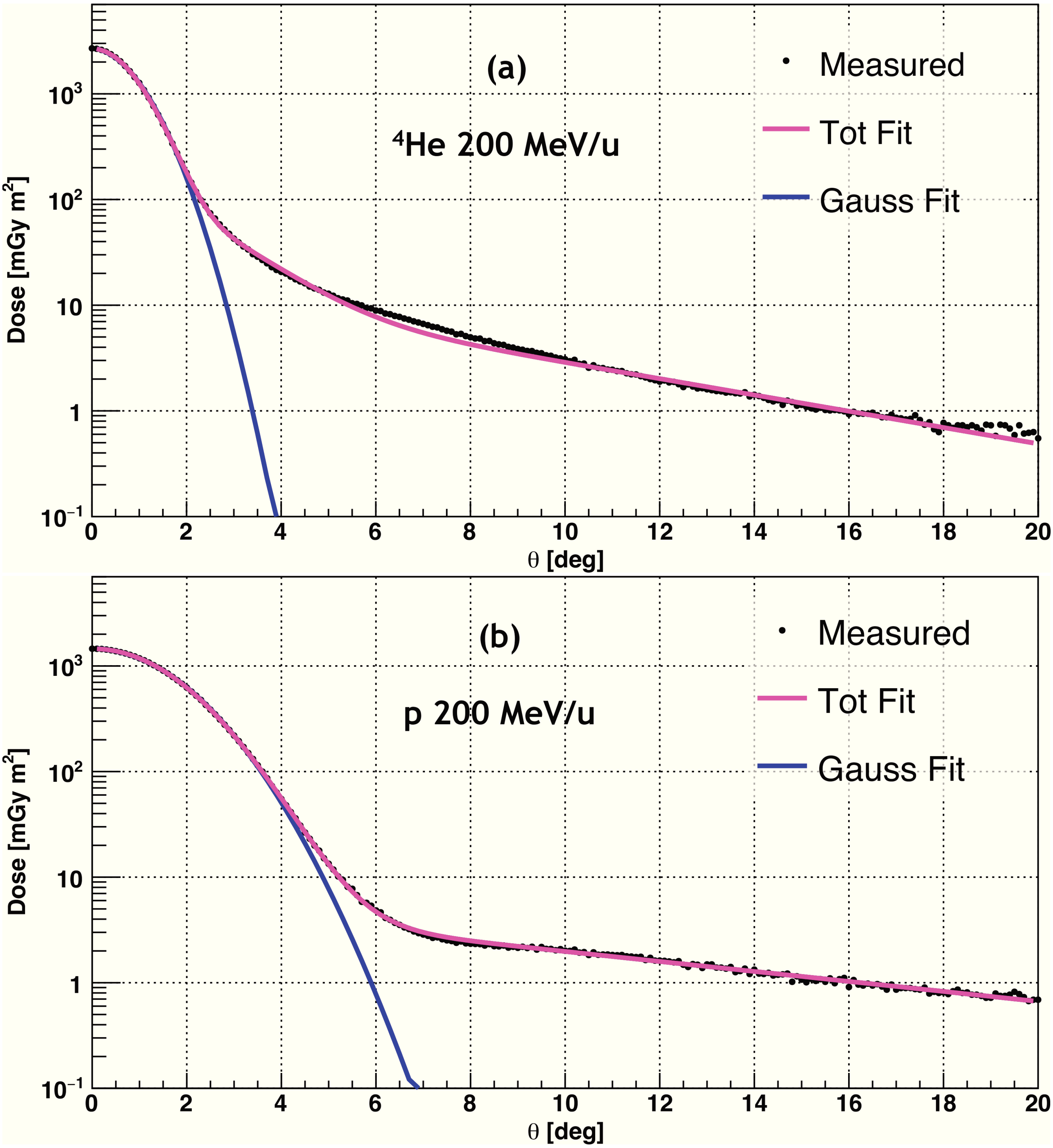

Figure 3.17.: Fit of the radial dose distribution of 200 MeV//u ^{4}He and proton beams impinging on 13.96 cm H_2O. The simple Gaussian fit is shown as comparison.

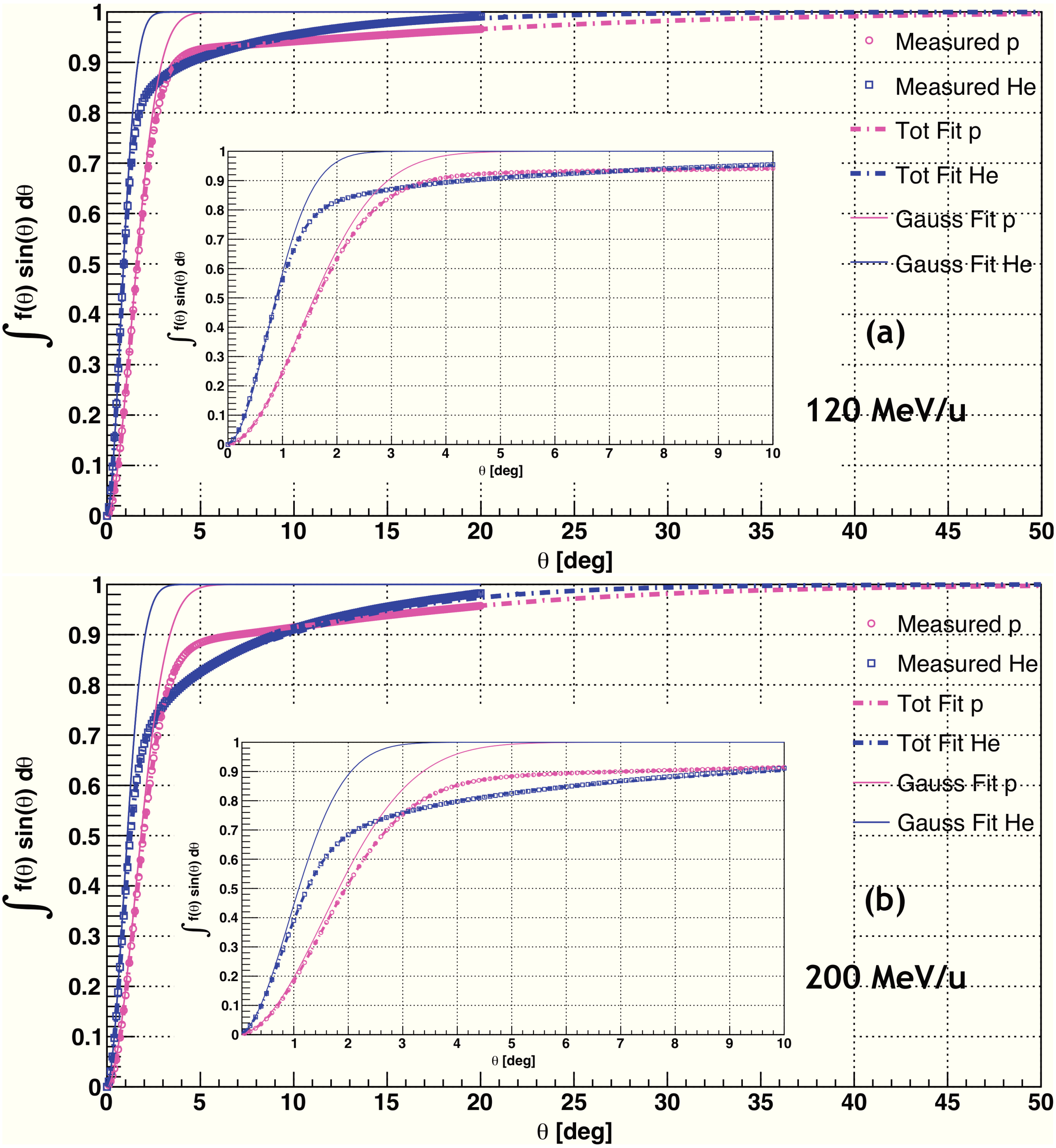

Figure 3.18.: Integral of the radial dose distribution of protons and Helium. The dashed lines represent the integral of the best fit function applied to the measured points. The filled lines represent the integral of the Gaussian fit to the measured points. Open symbols are the integral of the measured points. (a) shows the comparison for 120 MeV/u protons and Helium ions impinging on 4.28 cm H_2O and (b) shows the comparison for 200 MeV/u beam energy impinging on 13.96 cm H_2O.

Conclusion and Future work

In the last years ^{4}He ions have been regaining the attention of the particle therapy community, as they seem a good compromise between protons and ^{12}C ions, which are nowadays the two available options.

To exploit the clinical advantages of ^{4}He ions in particle therapy, among other requirements there is the need of a dedicated treatment planning. To do so, basic information such as a description of the beam lateral scattering distributions, fragmentation cross sections describing the loss of the primary particles and the build up of secondary fragments are required. A collection of cross sections from literature (Fig. 3.3) indicated a gap in the therapeutic energy range. The aim of this work was to provide fragmentation cross section of ^{4}He ions in the therapeutic energy range in order to benchmark the new model developed ad hoc and implemented in TRiP98 [1]. Moreover, the data presented here can validate a benchmark existing beam algorithms [2, 3] and Monte Carlo codes like Geant4 [4] and Fluka [5] .

The experiments presented in this thesis were performed in the clinical accelerator facility HIT, Heidelberg, Germany. ^{4}He beams of 120 and 200 MeV/u have been used to measure:

- Survival Fraction of the primary ions passing through different water depths;
- total yield of all secondary fragments produced by nuclear fragmentation at different water depths (fragments build up);
- angular distributions of the remaining ^{4}He particles and secondary fragments between 0° and 23° with respect to the primary beam direction;
- kinetic energy spectra of all particle species;
- lateral dose distribution after a scatter target, including information on the beam halo at large angles.

The study of the ^{4}He Survival Fraction resulted in an "effective" fragmentation cross section of 636±17 mb and a mean free path length λ of 47±6 cm. A comparison of the total reaction cross section of protons, ^{4}He and ^{12}C at the same depth in water show how the values rises with increasing beam charge due to the contribution of different reaction mechanisms [20]. As described in Section 1.2.4, the reaction channels of light fragments produced by the interaction of ^{4}He particles with H_2O are less then those for ^{12}C ions. This results in a higher Survival Fraction for 390 MeV/u ^{12}C than 200 MeV/u ^{4}He than, reaching 16% more in the plateau region and 27% in the region before the Bragg peak.

The comparison of the attenuation curve and the build up of the secondary fragments with the TRiP98 calculations show a good agreement. No correction factors were needed as for ^{12}C ions [44]. This result suggests that the assumption of a one-step process of direct reaction (Section 1.2.4) included in TRiP98 new version [1] describes well the physics mechanism behind these nuclear reactions.

The integral of the angular distributions show that they are much broader for all secondary fragments than for the surviving primary beam. The latter, in fact, cannot be detected at angles bigger than 12°, while the former are still very abundant up to 23°. Especially for deuterons and protons, the extrapolation of their integral yield up to 90° shows a contribution between 23° and 90° up to 10% and 30% of the total yield, respectively. Tritons and ^{3}He, instead, contribute only a few percent.

The kinetic energy spectra of secondary fragments are broader than the primary beam especially for deuterons and protons, which present a characteristic tail extending up to twice the residual energy of ^{4}He particles. The conversion in dose of the double differential yields presented in Fig. 3.16(a) and (b) highlights the different contribution of each particle species at each angle. ^{4}He dominates up to 8° while the major contributors to the tails of the distribution are the H isotopes, with protons being the most significant.

The lateral profile of scattered ^{4}He ions presented in Fig. 3.15(a) and (b) indicates qualitatively a behavior similar to protons, strongly underestimated by the prediction of the simple Gaussian approach from the multiple scattering theory (Section 1.2.3). The Gauss-Rutherford function describes successfully the tail of the dose distribution in an angular range of ±4°. The ^{4}He total radial dose profile (Fig. 3.17(a)) could be accurately fitted with a double Gauss function plus an exponential function. A comparison of the latter with proton distributions showed that even though the core of the ^{4}He beam profile has a sharper gradient, the contribution from secondary fragments influences significantly the dose distribution between 5° and 10°. Furthermore, because of the fragments the ^{4}He halo appears more pronounced than protons and thus a good parametrization of the dose profile is of extreme importance in the treatment planning systems. This parametrization will, in fact, effect the dose conformity of a scanned pencil beam not only at the border of the target volume but also in its centre (Appendix D).

Consistency tests for checking the dependency of the results on the on the experimental methodology (dose distribution with the 2D PTW detector, attenuation of the primary beam flux and build up of the fragments vs. double differential yields) indicated a good quality of the measured data.

The experimental setups have been optimized in term of target thickness and beam energy. For the attenuation of the primary beam flux, the targets were chosen in order to minimize the thickness of the container material compared to the target itself. Especially for the thin water targets (1, 3 and 3.5 cm H_2O), this issue was important to ensure a good precision of the experimental data. For the double differential yield measurements, the absorber thicknesses were selected to match approximately half of the range in water (4.28 cm compared to the Bragg peak at 10.5 cm for the 120 MeV/u beam and 13.96 cm compare to the Bragg peak at 25.8 cm for the 200 MeV/u beam). These thicknesses are a good compromise between achieving enough statistics for the secondary fragments in a reasonable time and having an average attenuation effect for the primary beam.

The setup used for this work would have to be modified for different beam energy and the target thicknesses. Below 120 MeV/u, a thinner ΔE and E detectors should be used. Moreover, the BaF_2 detector cannot be exposed to high fluxes because of activation, leading to a higher acquisition time. When the telescope is placed at large angles, the beam rate can be raised up to about 10^5 particle/s, which represents the limit for the SC1 plastic scintillator. Using a different beam monitor, such as a diamond detector [65], would allow a higher flux providing also a better signal for the TOF measurements.

Another limitation of the present setup arises from the use of thick absorbers (above ~ 10 g/cm^2), which are not optimal for an accurate measurement of the total fragmentation cross section (σ_{tf}), mainly for two reasons: σ_{tf} has a dependence on the primary beam energy, which becomes very strong below 100 MeV/u, and its value can significantly change if the target is thick enough to allow higher generations of interactions. High precision (error $<$ 0.1%) yield measurements are required for minimizing the uncertainty on the cross section values. The latter have, in fact, a logarithmic dependence on the yields and thus their errors will be extremely sensitive to small variations. In order to improve the measurement precision, setups such as that used in the Fragmentation of Ions Relevant for Space and Therapy (FIRST) experiment [66] are more appropriated. An alternative to a complex setup is to measure the attenuation curve with targets thicknesses between 0.1 and 10 g/cm^2. A fit performed on these data provides a more robust and accurate estimate of the fragmentation cross section avoiding the consequences of using thick absorbers.

In the future, the same study described in this work has to be performed at different beam energies (from 70 to 250 MeV/u) using water or tissue-equivalent targets. For every energy, the attenuation of the primary beam and the double differential yields have to be measured for target thicknesses corresponding to the entrance channel, the Bragg peak region and tail. Moreover, measurements of the total fragmentation cross section in thin elemental target (as graphite) need to be performed in the gap of data available in literature to validate and benchmark the Monte Carlo codes.

Another issue to be considered is that neutrons are an important contributor to the complex radiation field produced by nuclear interactions of the primary beam with the patient's body. To measure their yield, a detector with a good efficiency is required. The BaF_2 crystal used in this work has an efficiency up to 20%, depending on the neutron energy. Thus, an accurate calibration is required before the detector can be used for this purpose [67]. Only three studies investigating the neutron yields produced by ^{4}He beams were found in literature: Kurosawa et al. [68, 69] characterized the neutron field produced by 100 and 180 ^{4}He ions impinging on thick absorbers made of aluminum, copper and lead and Heilbronn et al. [70] used a 155 MeV/u ^{4}He beam stopping in aluminum targets.

The results of this work can be summarized as follow:

- ^{4}He ions are attenuated less than ^{12}C particles when tranversing water;
- ^{4}He ions have a shorter tail than ^{12}C ions in the Bragg curve but the dose contribution from the fragments is more pronounced than for proton beams;
- ^{4}He ions suffer much less lateral scattering than protons.

The results presented in this work indicate that even though a single particle species optimal for cancer treatments does not exist [1, 35], ^{4}He ions exhibit advantageous characteristics for particle therapy, and might be considered a perfect candidate for the treatment of pediatric patients.

Appendices

A EDR2 X-rays Films and PTW 2D array

Since radiotherapy started, the most common tool for radiation imaging has been the silver halide film[71]. However, with the increasing complexity of the radiation treatments, two dimensional detector arrays have gained popularity [72].

The Film is basically used because of its high spatial resolution and rapid handling, its clinical used include localizing disease, aligning the patient for treatment and verifying the dose distribution delivered to the patient. Even if the main use of this detector is with X-rays, nowadays they are widely used with charged particles and they seem to be perfect for envelope and lateral scattering measurements.

However, the detector array has numerous advantages on the Film. It is efficient because it acquires simultaneously many point doses, it is versatile and reliable. Its clinical used is commissioning of Treatment Planning System (TPS), machine Quality Assurance (QA) and individual patient verification in the case of intensity modulated or volumetric modulated arc therapy [72].

A.1 EDR-2 Films

The EDR-2 films were released from Kodak as an extended range film [71]. The film consist of a polyester layer of 25.5 mg/cm^2, coated with an emulsion layer on each side and a packaging of paper of 13.8 mg/cm^2 and 16.4 mg/cm^2, respectively. All together the film has a thickness of 1176 μm. The size of the film is 25 x 30 cm^2 and each film comes in a light-tight ready pack.

The response of a grain in the film is related to its activation probability that depends on the dose deposited in the grain [73]. Studies about the dose response of the films [71] showed the dependency of the curve from the ion species and the dependency from processing conditions, such as temperature, concentration and activity of the developer [73]. The disadvantage for film dosimetry of heavy ion beams is mainly the dependency of the response on the local ionization density that varies with particle energy and atomic number [71]. Fragmentation processes of the primary beam have to be taken into account.

In FigA.1 the dose response of the films for different beam type is presented. Electron, protons, carbon and iron ions have been used at different energies. For electron, proton and carbon beams, the sensitivity of the beam response decreases per unit dose in water as the stopping power of the primary particles increases.

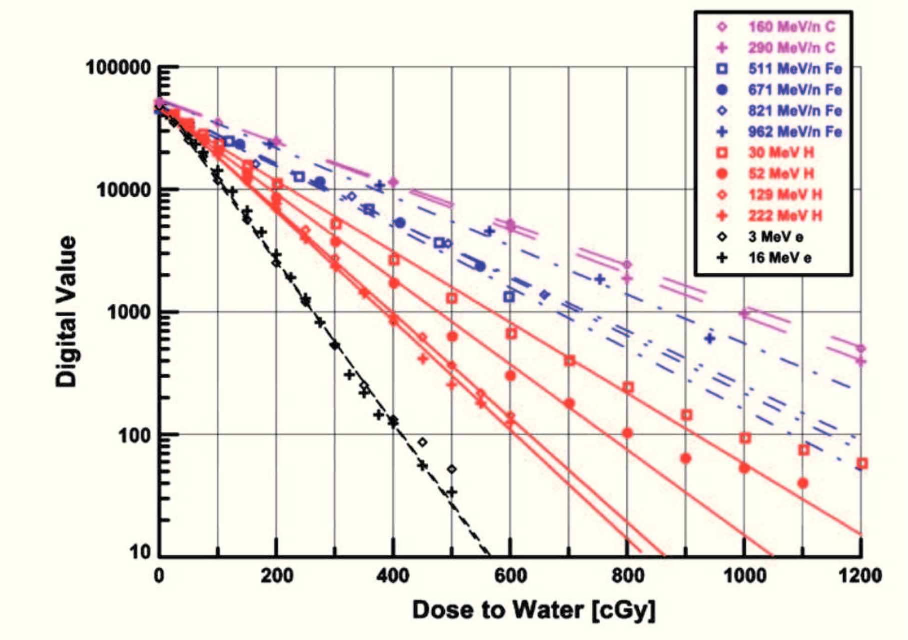

Figure A.1.: Dose-to-water response curves of electrons, protons, carbon and iron beams at different energies. The figure was taken from Moyers et al. [71]

A.2 PTW 2D array

For QA procedure in the radiotherapy clinic with ions, panel device like the PTW Octavius 1500 2D array is used. This detector has an highest detector density and a large field coverage. It consists on a matrix of 1405 gold standard ionization chambers arranged in square of 10 mm side. At the center of each square an additional chamber is placed, nearly doubling the resolution. The size of the array is 27 x 27 cm^2 that allows large field measurements.

The advantage of this detector is that the ionization chambers feature an excellent relative response stability, avoiding the need of frequent recalibration. The device is useful for real-time measurement and it can provide precise measurement even in penumbra regions [74]. Compare to previous version of detector array (Seven29 and Octavius729) it presents some additional advantages: it has twice the detector density and because of its design it has no line without detectors; it has a better shielding of the electronics, can handle higher dose rates and have a faster read out time; it shows a great stability that leads to a good reproducibility of the measurements [72].

The software of the detector provides a response directly in a dose matrix that allows a faster analysis of the data.

The detector resulted suitable for the lateral scattering measurements, giving a noiseless response in the beam halo with a good spatial resolution.

B Scintillator Detectors

The detection of ionizing radiation by scintillation light produced in certain materials is one of the oldest techniques on record. The scintillation process remains one of the most useful methods available for detection and spectroscopy of a wide assortment of radiation. The ideal scintillation material should have the following properties:

- linear conversion of the kinetic energy of charged particles into detectable light with a high scintillation efficiency;
- short decay time of the induced luminescence to generate fast signal pulses;
- the material should be of good optical quality and subject to manufacture in sizes large enough to be of interest as a practical detector.

It is difficult for a material to meet all these criteria and the choice of a scintillator is a compromise of all the factors depending on the use. Scintillators can be grouped in two categories: organic and inorganic. In our setup both of them were used as plastic scintillators belong to the former group while the BaF_2 to the latter. In the following sections the properties of the detectors used for the experiment are described to justify their selection for the measurements.

B.1 Plastic scintillators

The SC1 and the ΔE detectors used in the experiment are NE102 plastic scintillators of 1 mm and 5 mm thickness, respectively. The SC1 detector provides both a signal for the time-of-flight and the total amount of primary particles incident on the target while the ΔE measures the energy loss of the particle passing trough. The choice of different thicknesses is clear: for the SC1 detector is important to minimize the fragmentation of the primary ions in the plastic material, for the ΔE is important to detect particles even close to minimum ionization, gammas and neutrons.

Scintillators respond directly to ionization generated by charged particles. Neutral radiations and gamma rays are detected if they produce a recoil electron or nucleus in the scintillator material.

A relatively small fraction of the ionization energy lost by a charged particle in a scintillator is converted into fluorescent light energy. The rest is dissipated non-radiatively primarily in the form of lattice vibration or heat. The fluorescence light is characteristic of the molecular structure of the scintillator. The fraction of the particle energy that is converted depends on

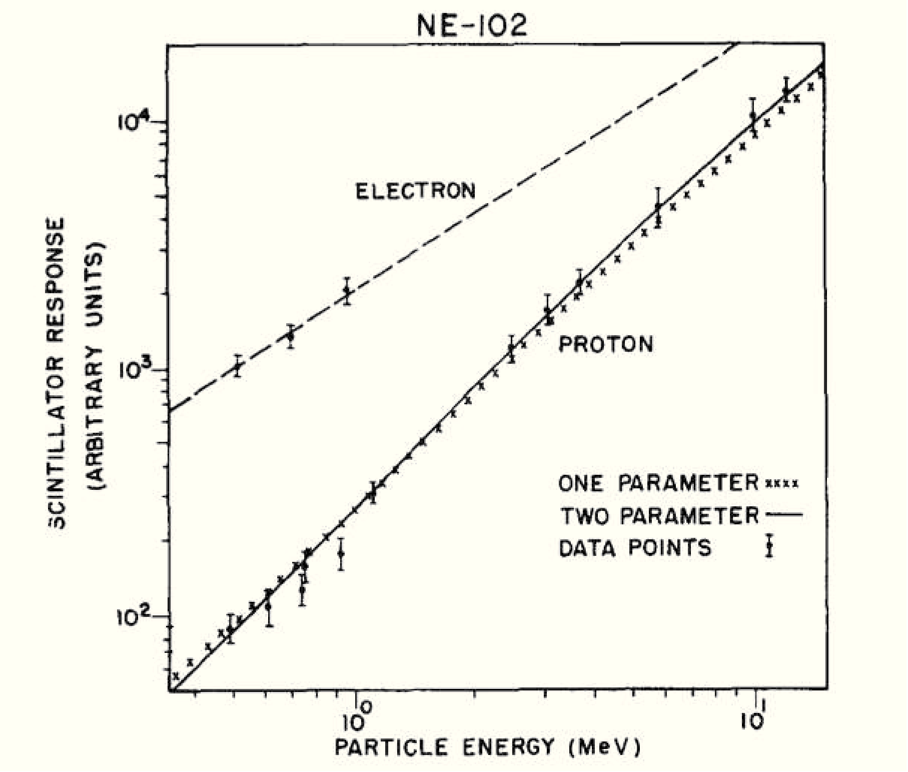

Figure B.1.: Scintillation light yield for a common plastic scintillator NE102 when excited by electrons or protons [75].

both particle type and its energy. The scintillation efficiency, i.e. the fraction of ionization energy converted into fluorescent light, differs for each type of scintillator and also depends on the type of charged particle causing the ionization. For example, electrons generate more light than heavy ions of equal energy when stopped in organic scintillator. The response to electrons is linear for energies above $\sim$ 125 KeV while up to much higher energies for charged particles [75]. The scintillation response of the NE102 is showed in Figs. B.1 and B.2.

The main advantage of using a plastic scintillator is the very short decay time of 2-3 ns that is translated into a high efficiency and short dead time. Its main disadvantage is the limited energy resolution. For the measurements reported in this thesis, the former represents an advantage for improving the TOF, and thus kinetic energy, resolution.In fact, for our setup we need primarily high resolution in time and the energy resolution of the scintillator is enough for us to clearly distinguish the different particles.

B.2 BaF_2 crystal scintillator

The Barium Fluoride detector used for the experiment as *E* detector is an inorganic crystal of 14 cm length, with an hexagonal shape of 4.4 cm inscribed radius. The crystal is directly coupled to a Thorn EMI 9821 QB photomultiplier. The BaF_2 is the only known inorganic crystal scintillator

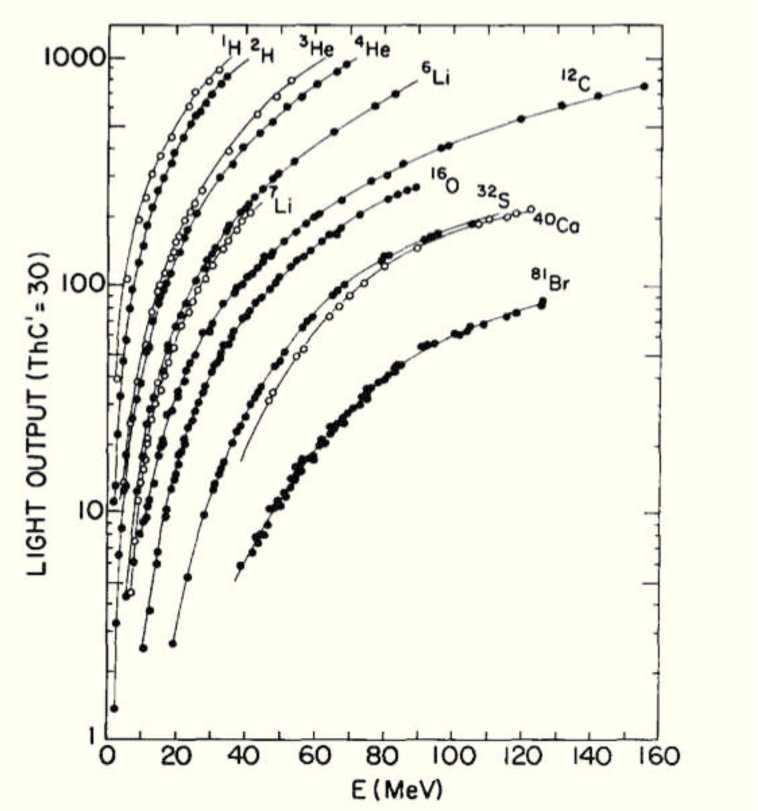

Figure B.2.: Response of a NE102 scintillator to different kinds of ions [76].

with a high atomic number (Z=56). The signal given by the detector can be divided into two components that change depending the radiation species: a short one with a decay time of 0.6 ns and ~30 ns lenght, and a long one with a decay time of 0.63 μ s and ~1.5 μs lenght (Fig. B.3).

The typical signal generated by photons consists only of the short components, while charged particles give a very pronounced long component whose amplitude increases with increasing charge. The signal produced in the BaF_2 by neutrons show a behavior in between ions and photons. Due to the long and short components, it is possible to distinguish incoming photons and neutrons (pulse-shaping discrimination). The latter produce mainly charged particles like protons and deuterons, which results in a signal with a long component, while incoming photons produce only scintillation light of the short component.

These properties indicate this crystal as one of the best choices for measurements requiring high efficiency of all particle types and fast response. The energy resolution is excellent among the scintillation detectors due to the high density of the crystal (ρ = 4.88 g cm^{-3}). With this configuration, length and density, the range of the protons in the detector is up to approximately 250 MeV and for the neutrons around 200 MeV.

The detection efficiency of the BaF_2 for neutrons depends on their kinetic energy. Several studies on the efficiency response of this detector were performed [77], [78]. In the study of

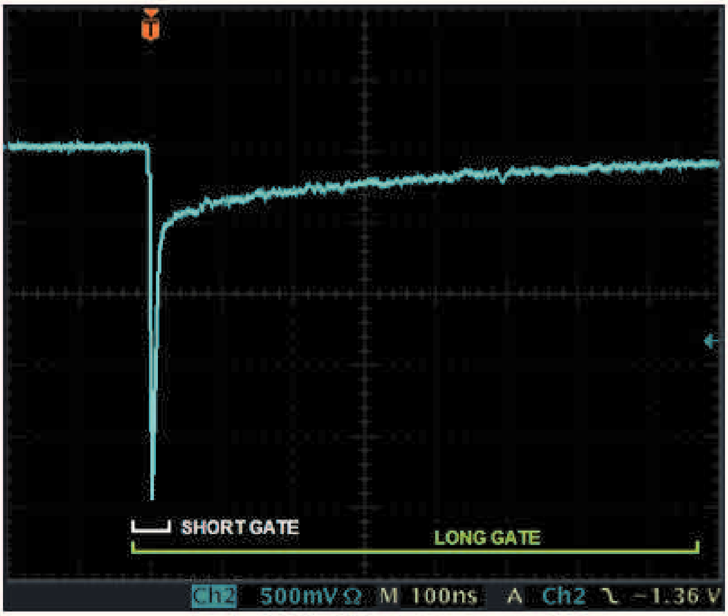

Figure B.3.: Typical signal provided by the BaF$_2$ detector. The length of the gates for acquiring the fast and slow components are indicated.

Gunzert-Marx et al. [42], the detection efficiency for mono-energetic neutrons at five different energies ranging from 45.4 to 198.2 MeV was obtained. The efficiency can be parametrized as

$$\epsilon(E_n) = \epsilon_0 \exp(-\lambda(E_n) \cdot E_{thr}) \tag{B.1}$$

where ϵ_0 denotes the efficiency extrapolated to the limit zero threshold and λ is the slope parameter which depends on the energy of the incident neutrons [42]. In figure (B.4) is shown the neutron detection efficiency of the BaF_2 as a function of the neutron energy for an electronic threshold of 10 MeV$_{pe}$. At low neutron energies the efficiency increases rapidly with energy and reaches above 100 MeV a plateau value of about 20%. This value is high and makes the BaF_2 detector attractive for the detection of high-energy neutrons [42].

Another important feature of this detector is the internal sources, that are impurities in the crystal having different intensity for each detector. Thus in some crystals its not possible to detect the internal source. The impurities are: ^{226}Ra (4.78 MeV), ^{222}Rn (5.49 MeV), ^{218}Po (6.00 MeV), ^{214}Ra (7.69 MeV). The typical spectrum of these sources of our BaF_2 detectors is shown in figure (B.5).

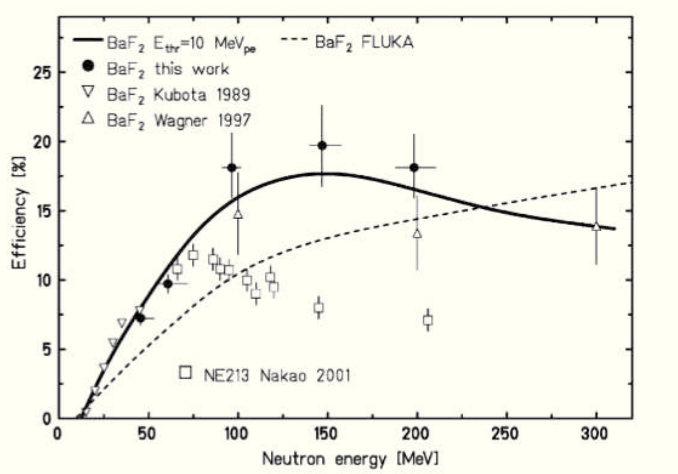

Figure B.4.: Measured neutron efficiency of various BaF_2 detectors vs. neutron energy [42].

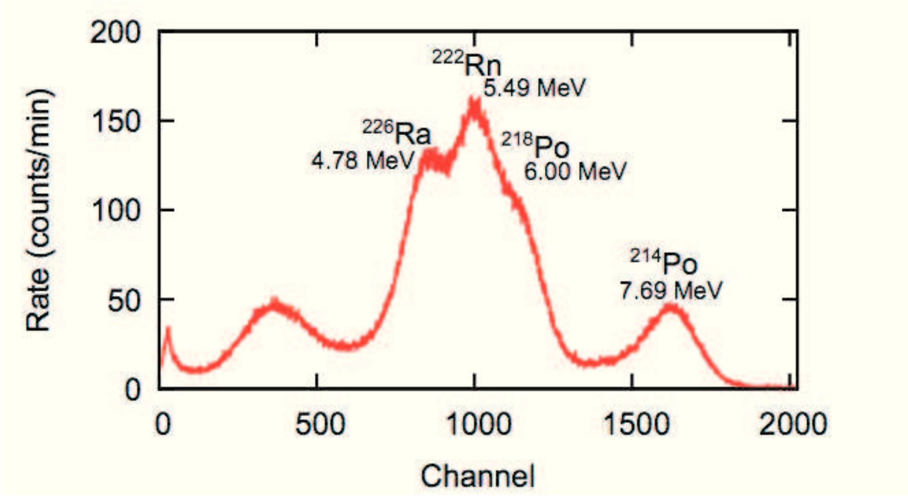

Figure B.5.: Typical spectrum of the internal radioactive sources of a barium fluoride crystal. Courtesy of A. Eichhorn

The presence of the internal sources has two aspects: one positive, because through them it is possible to make an energy calibration of the detector of charged particles; the negative one is the background caused by the internal sources for the measurements.

C Collection of kinetic energy spectra

In this section all the kinetic energy spectra that were not introduced in Section 3.2 are presented.

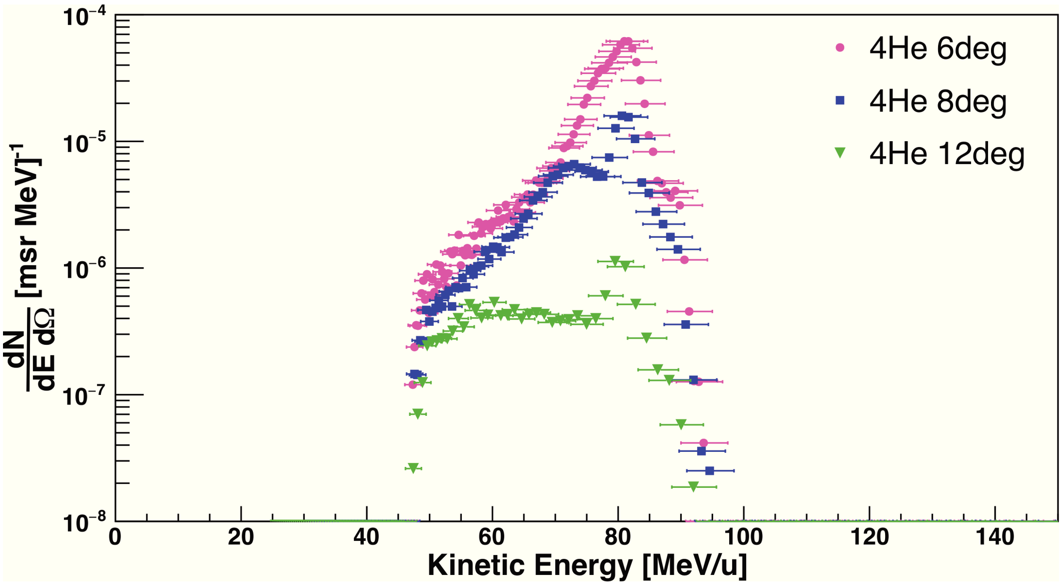

Figure C.1.: Kinetic energy spectra of the primary beam with initial energy 120 MeV/u.

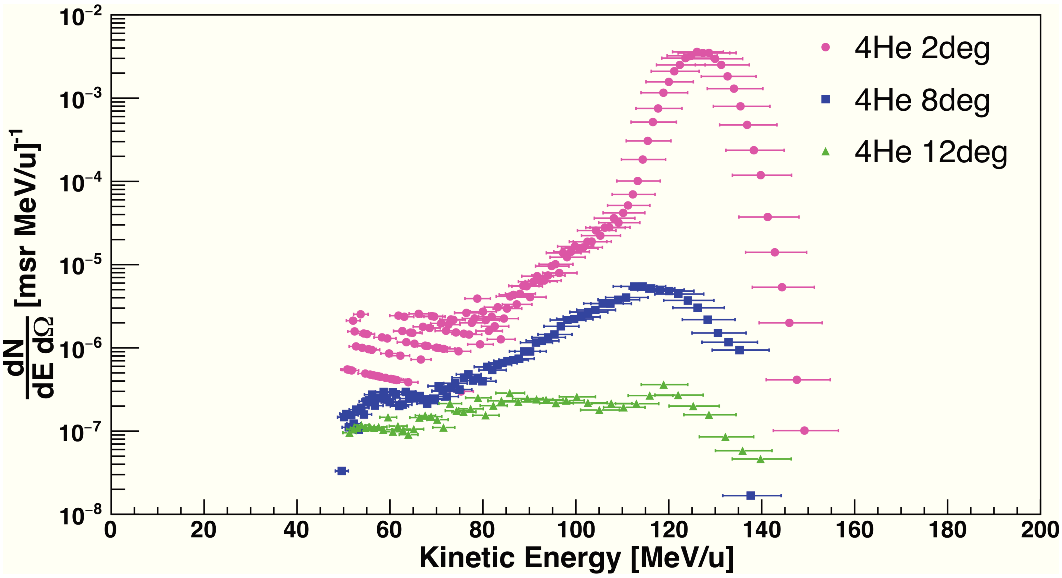

Figure C.2.: Kinetic energy spectra of the primary beam with initial energy 200 MeV/u.

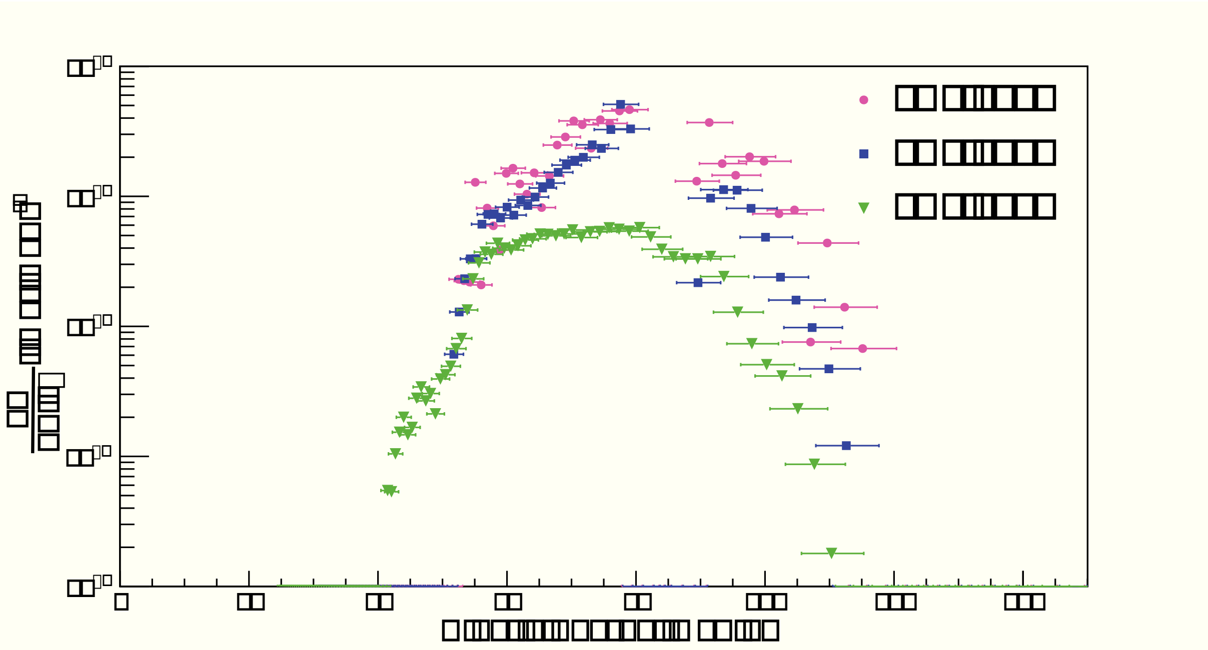

Figure C.3.: Kinetic energy spectra of ^{3}He ions produced by 120 MeV/u ^{4}He beam. At angles of 0° and 2° a full separation of ^{3}He ions from ^{4}He was not possible so that a gap in energy can be observed.

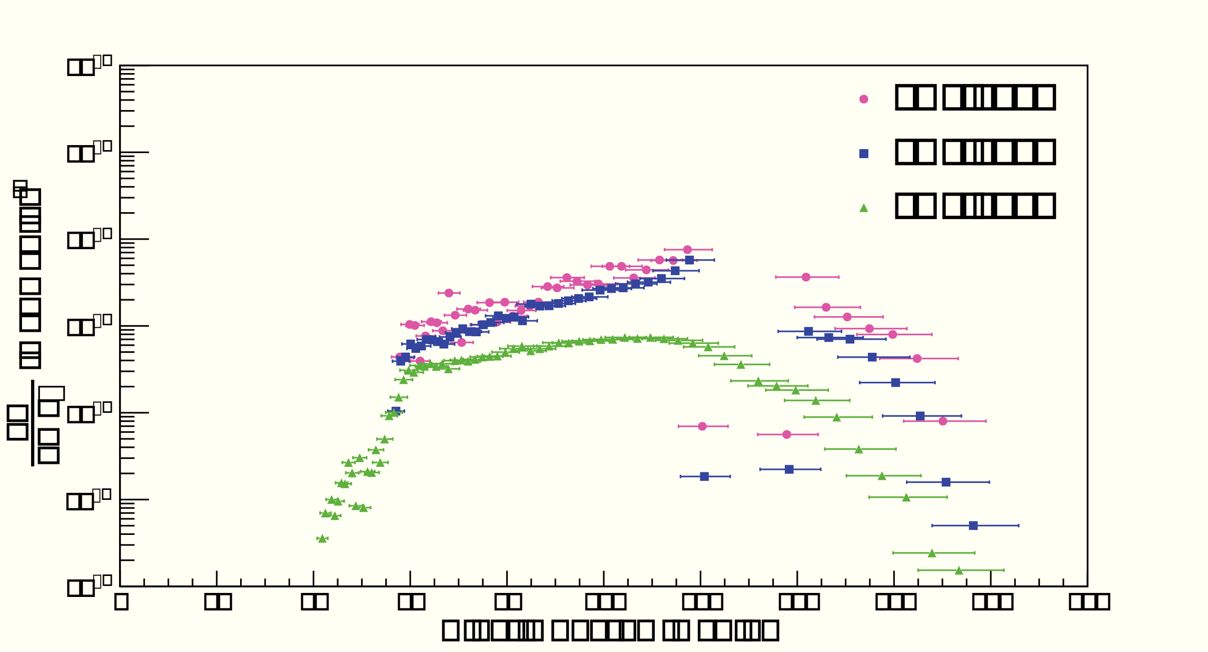

Figure C.4.: Kinetic energy spectra of ^{3}He ions produced by 200 MeV/u ^{4}He beam. At angles of 0° and 2° a full separation of ^{3}He ions from ^{4}He was not possible so that a gap in energy can be observed.

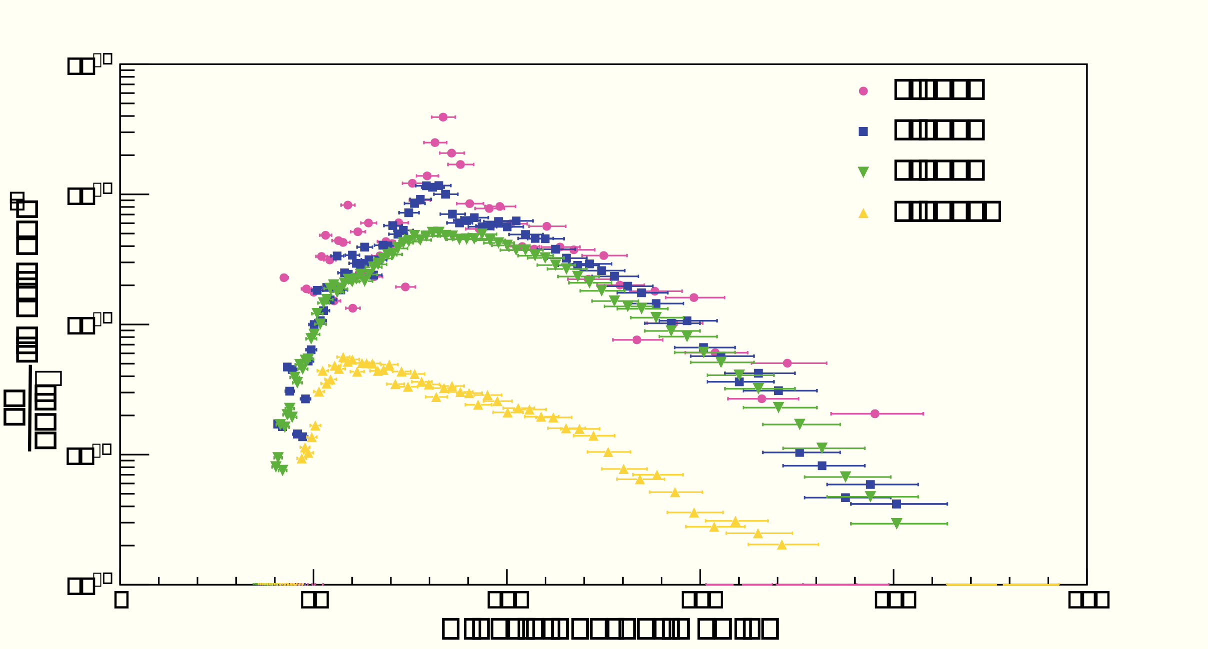

Figure C.5.: Kinetic energy spectra of protons produced by 120 MeV/u ^{4}He beam.

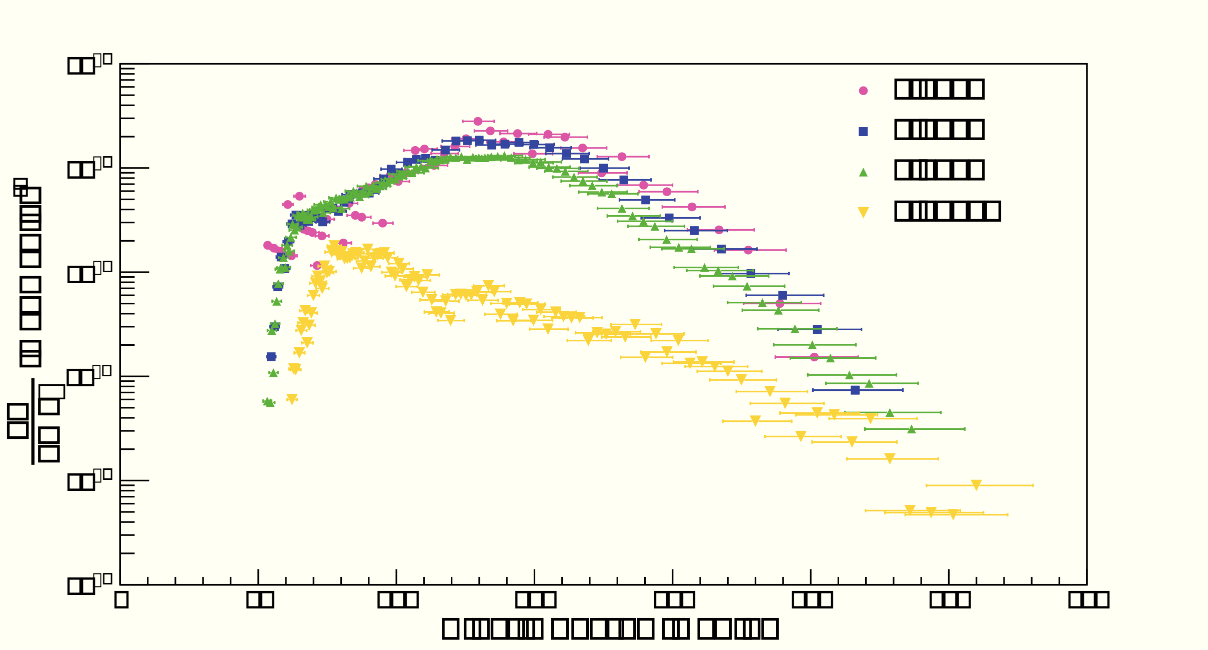

Figure C.6.: Kinetic energy spectra of protons produced by 200 MeV/u ^{4}He beam.

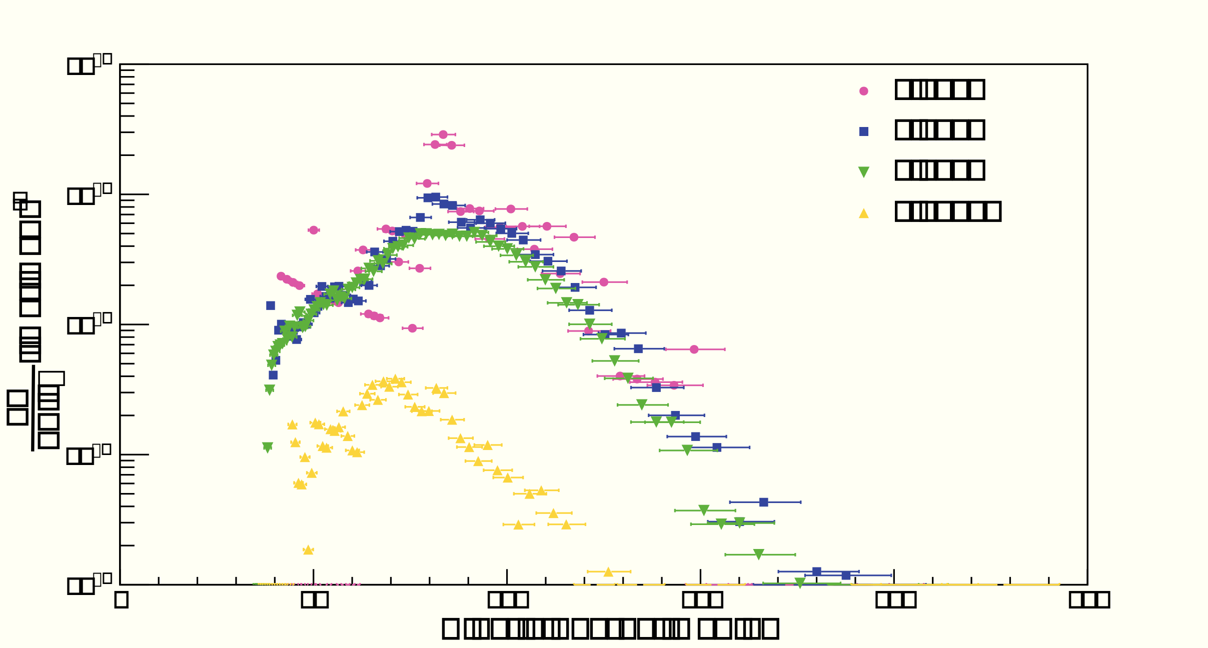

Figure C.7.: Kinetic energy spectra of deuterons produced by 120 MeV/u ^{4}He beam.

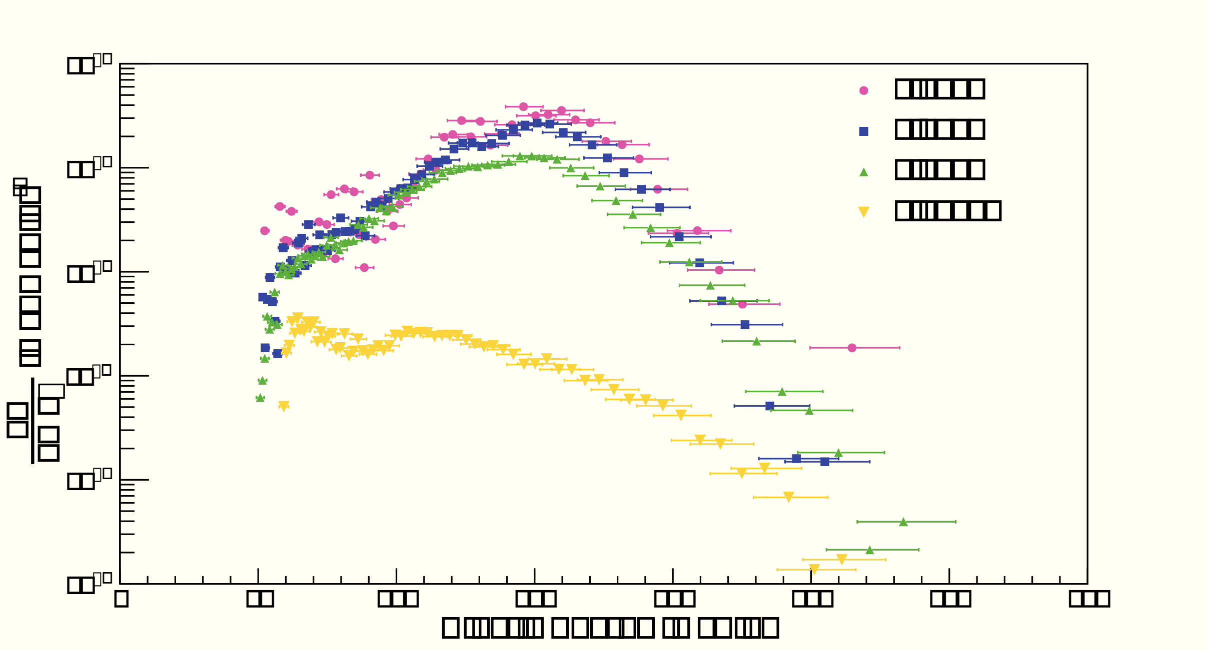

Figure C.8.: Kinetic energy spectra of deuterons produced by 200 MeV/u ^{4}He beam.

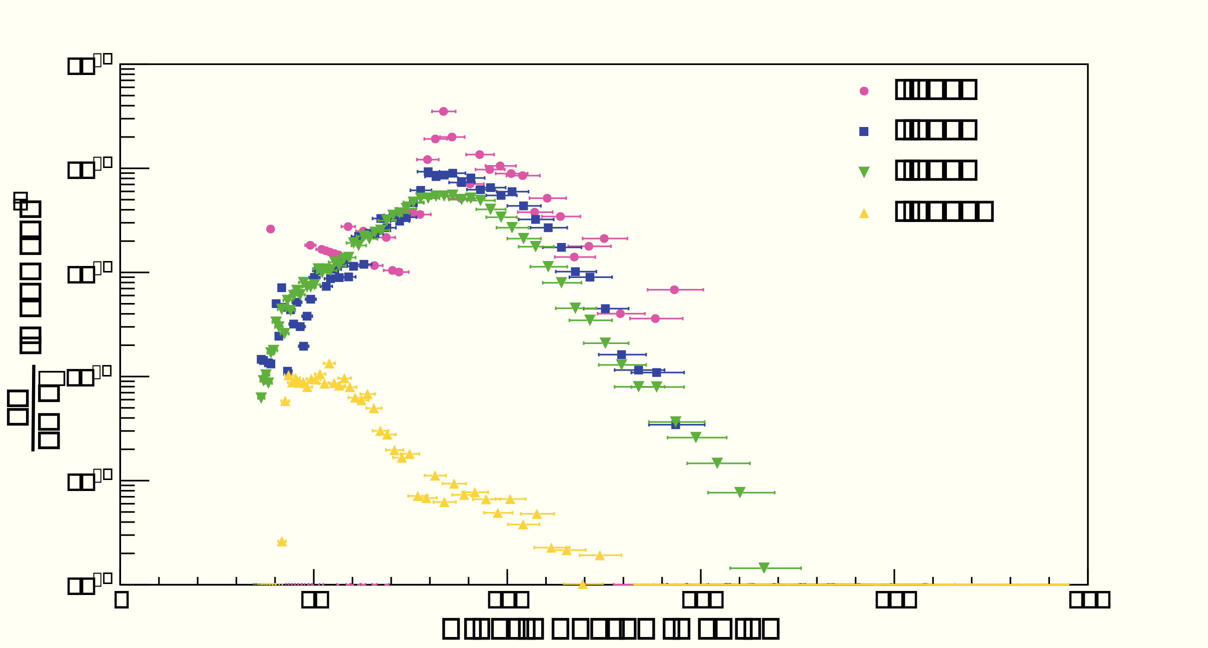

Figure C.9.: Kinetic energy spectra of tritons produced by 120 MeV/u ^{4}He beam.

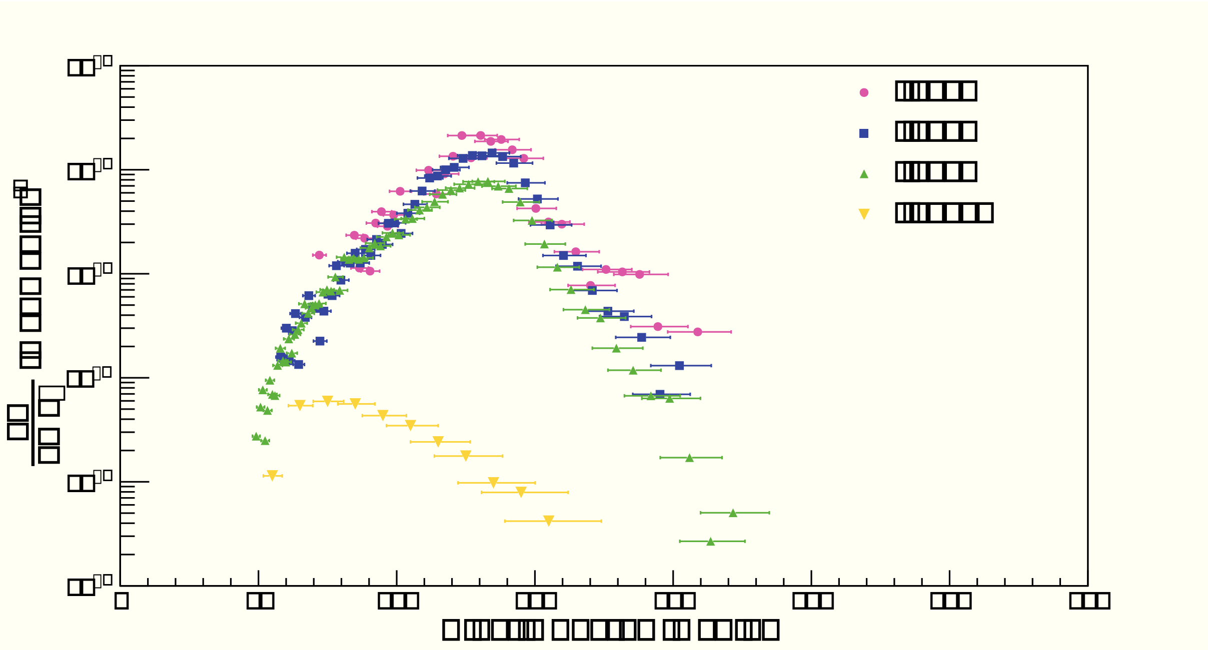

Figure C.10.: Kinetic energy spectra of tritons produced by 200 MeV/u ^{4}He beam.

D Dose distribution of a scanned field

In particle therapy the dose delivery is realized actively by sweeping the narrow pencil beam over a matrix of single positions (raster points). In this section, the effect of the shape of the lateral profile on the dose distribution from the scanned film of a 200 MeV/u ^{4}He and proton beam was studied. In order to do that a target volume was scanned by using two approaches: a superposition of beams with a Gaussian dose profile (Fig. D.1), and a superposition of beams with the measured dose profile presented in Fig. 3.17 (Section 3.3.3). The Gaussian approach was used by all the treatment planning systems and nowadays is still used by some of them.

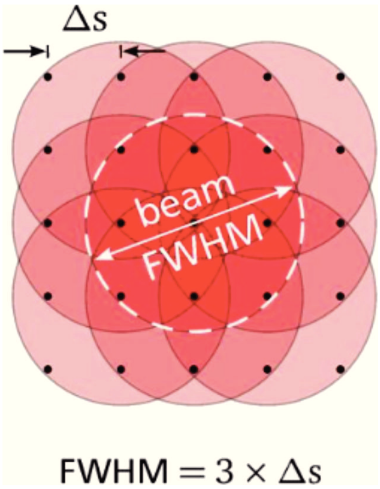

Figure D.1.: Overlap of single Gaussian beams. Generally a grid of 2-3 mm is used in combination with a beam FWHM of about 3 times the grids spacing. Figure from D. Richter [34].

The angular dose distribution of Fig. 3.17 was transferred (projected) on a plane with a distance of 15 cm from the scatter centre, corresponding to a typical drifting distance in the patient's body of scattered particles. This assumption is obviously a simplification of the real situation where the beam is continuously scattered and broadened in the target.

A 2D dose distribution was built by superimposing the beam projection distribution and shifting the beam spot in steps of 2.5 mm in x- and y-direction inside a square (target volume) size of 100x100 mm^2 (±50 mm) and in a smaller square of 60x60 mm^2 (± 30 mm). This provides a simplified estimation for a real scanning procedure in therapy, allowing a qualitatively description of the contribution of dose transported outside the target volume due to the tail of the radial dose distribution of the beam.

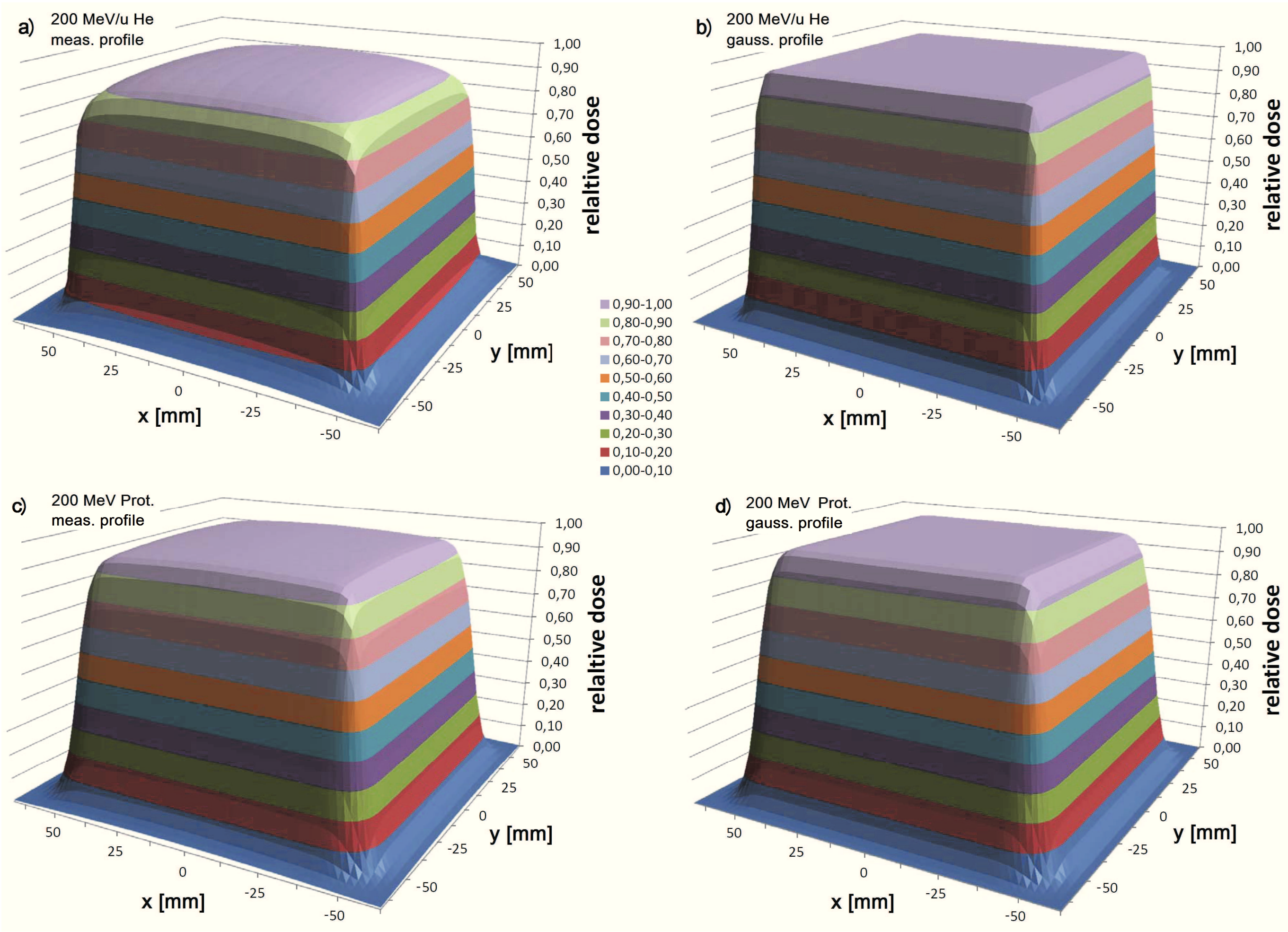

Figure D.2.: 2D dose distribution from a superposition of shifted (scanned) beam spots in a square of ±50 mm. The upper graphs (a+b) show the scanning for 200 MeV/u ^{4}He ion beams, instead the lower graphs (c+d) the ones for 200 MeV proton beams. The left figures (a+c) represent the dose from the measured beam profiles, whereas the right figures show the superposition of the fitted Gaussian profiles (having no dose tails).

In order to be able to compare the Gaussian and the real dose profile, the beam spots were superimposed with the same constant weights. In a real treatment planning system this effect would be compensated by increasing the weights at the border.

The results for a scanned field of 100x100 mm^2 are shown in Fig. D.2. It can be observed how the Gaussian beam profile delivers a flat plateau with a fast dose decreasing at few millimeters before the border. However, the realist profile delivers a “rounded” plateau with a smoother decreasing of dose at the borders.

A dose profile was extracted from the mid plane of the scanned dose distribution shown in Fig. D.2 and of a scanned dose in a target volume of ± 30 mm. The results are presented in Fig. D.3.

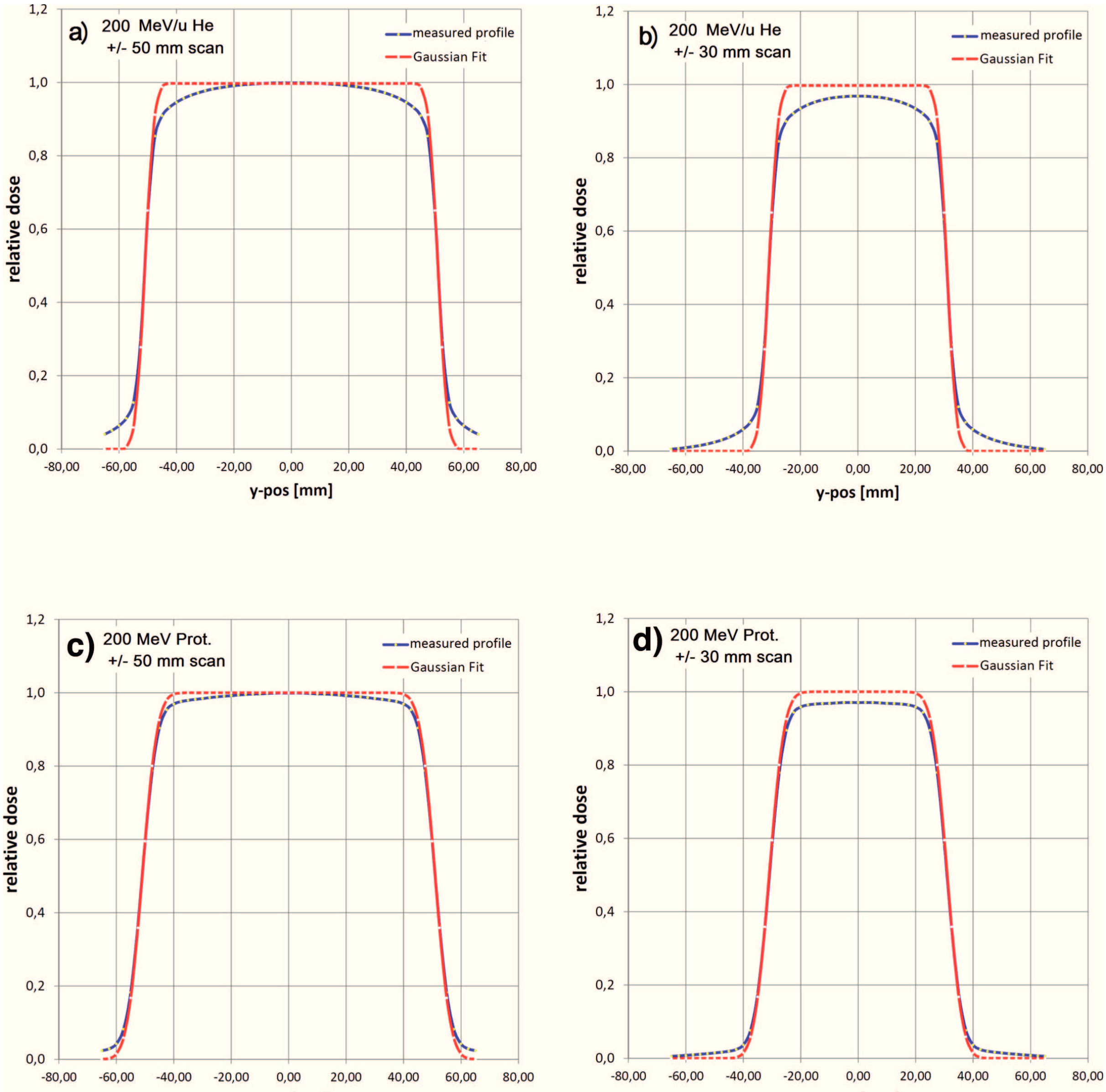

Figure D.3.: Dose profile through the mid plane of the superimposed (scanned) dose distribution for 200 MeV/u ^{4}He beams (a+b) and for 200 MeV proton beams (c+d). Fig. D.3(a) and (c) show the dose profile for a scanned target volume of ± 50 mm (corresponding to Fig. D.2) and Fig. D.3(b) and (d) for a target volume of ± 30 mm.

It can be seen in Fig. D.3(a) and Fig. D.3(c) how the effect of a single gaussian approach affects the border of the distribution, effect more pronounced for the helium dose distribution (Fig. D.3(a)) than for the proton one. By decreasing the target volume (Fig. D.3(b) and (c)) the effect increases also in the core of the distribution, reducing significantly the dose accuracy in the target volume.

Even though the dose fall off at the border of the dose distribution for the proton beam is larger compared to ^{4}He (as aspected), the tail contribution of the ^{4}He beams is higher due to the contribution of secondary fragments, as shown in Fig. 3.18 in Section 3.3.3. Therefore, a good parametrization of the lateral beam profile is of crucial importance for the treatment planning with Helium ions, where a Gaussian parametrization would be absolutely not sufficient.

E Error propagation analysis for statistical uncertainty

In this section the statistical error propagation is presented.

The number of each particle type obtained from the handmade graphical selections is assumed to be poissonianly distributed and thus its uncertainty is:

$$\epsilon_{counts} = \sqrt{counts} \tag{E.1}$$

Hence, the error on the dead time (Eq. 2.4 in Sec. 2.3.3) is calculated with the formula

$$\epsilon_{dt} = dead\ time \cdot \sqrt{\left(\frac{\epsilon_{Free}}{Free\ trig}\right)^2 + \left(\frac{\epsilon_{Acc}}{Acc\ trig}\right)^2} \tag{E.2}$$

where ϵ_{Free} and ϵ_{Acc} are the errors on the Free Trigger and the Accepted Trigger, respectively, calculated with Eq. E.1.

All counts must be corrected for the dead time as

$$counts_{corr} = \frac{counts}{dead\ time} \tag{E.3}$$

and are affected by the following uncertainty

$$\epsilon_{counts_{corr}} = counts_{corr}\ \sqrt{\left(\frac{\epsilon_{dead\ time}}{dead\ time}\right)^2 + \left(\frac{\epsilon_{counts}}{counts}\right)^2} \tag{E.4}$$

In order to get the Total yield the counts have to be divided by the number of incident primaries, therefore

$$\epsilon_{yield} = yield\ \sqrt{\left(\frac{\epsilon_{counts_{corr}}}{counts_{corr}}\right)^2 + \left(\frac{\epsilon_{in}}{incident\ particles}\right)^2} \tag{E.5}$$

where the error ϵ_{in} on the of the amount of incident particles impinging on the target is calculated with Eq.E.1.

For the differential yield obtained from the angular distribution measurements, instead, the counts have to be normalized not only by the number of incident primary ions but also by the solid angle. The uncertainty has to be considered has follow

$$\epsilon_{yield} = yield \sqrt{\left(\frac{\epsilon_{counts_{corr}}}{counts_{corr}}\right)^2 + \left(\frac{\epsilon_{in}}{incident\ particles}\right)^2 + \frac{\epsilon_{\Omega}}{\Omega}} \tag{E.6}$$

where Ω is the solid angle and ϵ_{Ω} the correspondent error. The latter is given by the propagation of the errors on the radius and the distance, equal to the sensitivity of the instrument used to measure them.

As explain in Sec.2.3.2, the largest uncertainty of the yield comes from the systematic error of the hand-drawn graphical contour. Therefore different graphical selections are made by including or excluding different area. Once these selections are made the yield is calculated and a difference with the main graphical selection is estimated. This difference is considered as an uncertainty in the yield and it is quadratically summed to the statistical error mentioned above.

List of Abbreviations

LBL	Lawrence Berkeley Laboratory
NIRS	National Institute of Radiological Sciences
GSI	GSI Helmholtz Center for Heavy Ion Research
PSI	Paul Scherrer Institut
HIT	Heidelberg Ion Beam Therapy Center
RBE	Relative Biological Effectiveness
LET	Linear Energy Transfer
DNA	DeoxyriboNucleic Acid
ICRU	International Commission on Radiation Units and Measurements
PMMA	Polymethylmethacrylate
MWPC	Multi Wire Proportional Chamber
2D	Two dimensional
CT	Computed Tomography
TPS	Treatment Planning System
TRiP98	Treatment Planning for Particles
FWHM	Full Width at Half Maximum
WEPL	Water Equivalent Path Length
IC	Ionization Chamber
TOF	Time of Flight
He	Helium
H	Hydrogen
Z	Nuclear charge
A	Nuclear mass
S.f.	Survival Fraction
QDC	Charge to Digital Converter
ADC	Analog to Digital Converter
TDC	Time to Digital Converter
LED	Leading Edge Discriminator
DT	Dual Timer
GG	Gate Generator
AMP	Amplifier
HIMAC	Heavy Ion Medical Accelerator
MIT	Marburg Ion beam Therapy center
CNAO	National Center of Oncological Hadronterapy
QA	Quality Assurance
FIRST	Fragmentation of Ions Relevant for Space and Therapy

List of Figures

List of Tables

Bibliography

[1] Krämer, M. *et al.* Helium ions for radiotherapy? physical and biological verification of a novel treatment modality. *Med. Phys.* **43** (2016).

[2] Fuchs, H., Strobele, J., Schreiner, T., Hirtl, A. & Georg, D. A pencil beam algorithm for helium ion beam therapy. *Med. Phys.* **39** (2012).

[3] Fuchs, H., Alber, M., Schreiner, T. & Georg, D. Implementation of spot scanning dose optimization and dose calculation for helium ions in hyperion. *Med. Phys.* **42** (2015).

[4] Agostinelli, S. *et al.* Geant4—a simulation toolkit. *Nucl. Instrum. Methods Phys. Res. A* **506** (2003).

[5] Böhlen, T. *et al.* The fluka code: Developments and challenges for high energy and medical applications. *Nuclear Data Sheets* **120** (2014).

[6] Durante, M. & Loeffler, J. S. Charged particles in radiation oncology. *Nat. Rev. Clin. Oncol.* **7** (2010).

[7] Jermann, M. Particle therapy statistics in 2014. *International Journal of Particle Therapy* **2** (2015).

[8] Wilson, R. R. Radiological use of fast protons. *Radiology* **47**, 487–491 (1946).

[9] Tobias, C. A., Anger, H. O. & Lawrence, J. H. Radiological use of high energy deuterons and alpha particles. *Am. J. Roentgenol Radium Ther. Nucl. Med.* **67** (1952).

[10] Castro, J. R., Petti, P. L., Blakely, E. A. & Linstadt, D. E. Particle radiation therapy. Tech. Rep. LBL-36229, PA:W.B. Saunders Company (1994).

[11] Castro, J. Clinical results in heavy particle radiotherapy. *Lawrence Berkley Laboratory Report* (1980).

[12] Castro, J. R. *et al.* Current status of clinical particle radiotherapy at lawrence berkeley laboratory. *Cancer* **46** (1980).

[13] Char, D. H., Kroll, S. M. & Castro, J. Ten-year follow-up of helium ion therapy for uveal melanoma. *Am. J. Ophthalmol* **125** (1998).

[14] Castro, J. R. *et al.* Experience in charged particle irradiation of tumors of the skull base: 1977 - 2013;1992. *Int. J. Radiat. Oncol. Biol. Phys.* **29**.

[15] Blakely, E. A. *et al.* Helium-ion-induced human cataractogenesis. *Adv. Space Res.* **14** (1994).

[16] Hirao, Y. *et al.* Heavy ion synchrotron for medical use —himac project at nirs-japan—. *Nucl. Phys. A* **538** (1992).

[17] Pedroni, E. *et al.* The 200-MeV proton therapy project at the Paul Scherrer Institute: conceptual design and practical realization. *Med. Phys.* **22** (1995).

[18] Eickhoff, H. *et al.* The GSI cancer therapy project. *Strahlenther Onkol.* **175 Suppl 2** (1999).

[19] Knäusl, B., Fuchs, H., Dieckmann, K. & Georg, D. Can particle beam therapy be improved using helium ions? - a planning study focusing on pediatric patients. *Acta Oncol.* (2016).

[20] Schardt, D., Elsässer, T. & Schulz-Ertner, D. Heavy-ion tumor therapy: physical and radiobiological benefits. *Rev. Mod. Phys.* **82** (2010).

[21] Bethe, H. Zur Theorie des Durchgangs schneller Korpuskularstrahlen durch Materie. *Annalen der Physik* **397** (1930).

[22] F., B. Bremsvermögen von Atomen mit mehreren Elektronen. *Zeitschrift für Physik* **81** (1933).

[23] Fano, U. Penetration of protons, alpha particles, and mesons. *Annual Review of Nuclear Science* **13** (1963).

[24] Schardt, D. *et al.* Precision bragg-curve measurements for light-ion beams in water. Annual Report, GSI (2008).

[25] Barkas, W. & Evans, D. *Nuclear Research Emulsions: Techniques and Theory*. Pure and applied physics (Academic Press, 1963).

[26] Comfort, J. R., Decker, J. F., Lynk, E. T., Scully, M. O. & Quinton, A. R. Energy loss and straggling of alpha particles in metal foils. *Phys. Rev.* **150** (1966).

[27] Vavilov, P. V. Ionization losses of high-energy heavy particles. *Sov. Phys. JETP* **5** (1957).

[28] Ahlen, S. P. Theoretical and experimental aspects of the energy loss of relativistic heavily ionizing particles. *Rev. Mod. Phys.* **52** (1980).

[29] Bednyakov, A. A. On the Molière theory of multiple scattering of charged particles (1947–1948) and its critique in subsequent years. *Physics of Particles and Nuclei* **45** (2014).

[30] Bethe, H. A. Molière's theory of multiple scattering. *Phys. Rev.* **89** (1953).

[31] Povh, B., Rith, K., Scholz, C. & Zetsche, F. *Particle and Nuclei* (Bollati Boringhieri, 1998).

[32] Cucinotta, F. L., Towsend, W. & Wilson, J. W. Description of alpha-nucleus interaction cross sections for cosmic ray shielding studies. *NASA technical Paper* **3285** (1993).

[33] Sitenko, A. G. *Theory of Nuclear Reactions* (World Scientific, 1990).

[34] Richter, D. *Treatment planning for tumors with residual motion in scanned ion beam therapy*. Ph.D. thesis, Technischen Universität Darmstadt (2012).

[35] Grün, R. *et al.* Assessment of potential advantages of relevant ions for particle therapy: a model based study. *Med. Phys.* **42** (2015).

[36] Haberer, T. *et al.* The heidelberg ion therapy center. *Radiother. Oncol.* **73** (2004).

[37] EPAC08 (ed.). *The heidelberg ion therapy (HIT) Accelerator Coming into operation*, TUOCG01 (2008).

[38] Schneider, C. A., Rasband, W. S. & Eliceiri, K. W. Nih image to imagej: 25 years of image analysis. *Nat. Meth.* **9** (2012).

[39] PTW. Measurements of spread-out-bragg-peaks with the PEAKFINDER and MP3-P. Technical Note D901.200.00/00 en, PTW-Freiburg.

[40] Carboni, S. *et al.* Particle identification using the (DELTA)e-e technique and pulse shape discrimination with the silicon detectors of the FAZIA project. *Nucl. Instrum. Methods Phys. Res. A* **664** (2012).

[41] Piersanti, L., Schuy, C., La Tessa, C. & Durante, M. Development of a VME data acquisition system. Tech. Rep., GSI (2013).

[42] Gunzert-Marx, K., Iwase, H., Schardt, D. & Simon, R. S. Secondary beam fragments produced by 200 MeV/u ^{12}C ions in water and their dose contributions in carbon ion radiotherapy. *New J. Phys.* **10** (2008).

[43] Tarasov, O. Lise++: Radioactive beam production with inflight separators. *NIM B* **266** (2008).

[44] Haettner, E., Iwase, H., Krämer, M., Kraft, G. & Schardt, D. Experimental study of nuclear fragmentation of 200 and 400 MeV/u ^{12}C ions in water for applications in particle therapy. *Phys. Med. Biol.* **58** (2013).

[45] Schall, I. *et al.* Charge-changing nuclear reactions of relativistic light-ion beams ($5 \leq z \leq 10$) passing through thick absorbers. *Nucl. Instrum. Methods Phys. Res. B* **117** (1996).

[46] Kox, S. *et al.* Trends of total reaction cross sections for heavy ion collisions in the intermediate energy range. *Phys. Rev. C* **35** (1987).

[47] Sihver, L. & Mancusi, D. Present status and validation of {HIBRAC}. *Radiat. Meas.* **44** (2009).

[48] Ferrando, P. *et al.* Measurement of ^{12}C, ^{16}O, and ^{56}Fe charge changing cross sections in helium at high energy, comparison with cross sections in hydrogen, and application to cosmic-ray propagation. *Phys. Rev. C* **37** (1988).

[49] Auce, A. *et al.* Reaction cross sections for 75 - 190 MeV alpha particles on targets from ^{12}C to ^{208}Pb. *Phys. Rev. C* **50** (1994).

[50] Ingemarsson, A. *et al.* New results for reaction cross sections of intermediate energy α particles on targets from ^{9}Be to ^{208}Pb. *Nucl. Phys. A* **676** (2000).

[51] Sourkes, A. M., Houdayer, A., van Oers, W. T. H., Carlson, R. F. & Brown, R. E. Total reaction cross section for protons on ^{3}He and ^{4}He between 18 and 48 MeV. *Phys. Rev. C* **13** (1976).

[52] Carlson, R. Proton-nucleus total reaction cross sections and total cross sections up to 1 GeV. *Atomic Data and Nuclear Data Tables* **63** (1996).

[53] Tripathi, R. K., Cucinotta, F. A. & Wilson, J. W. Accurate universal parameterization of absorption cross sections III–light systems. *Nucl. Instrum. Methods Phys. Res. B* **155** (1999).

[54] Webber, W. R., Kish, J. C. & Schrier, D. A. Total charge and mass changing cross sections of relativistic nuclei in hydrogen, helium, and carbon targets. *Phys. Rev. C* **41** (1990).

[55] Jaros, J. *et al.* Nucleus-nucleus total cross sections for light nuclei at 1.55 and 2.89 GeV/c per nucleon. *Phys. Rev. C* **18** (1978).

[56] Burigo, L., Pshenichnov, I., Mishustin, I. & Bleicher, M. Microdosimetry spectra and RBE of ^{1}H, ^{4}He, ^{7}Li and ^{12}C nuclei in water studied with geant4. *Nucl. Instrum. Methods Phys. Res. B* **320** (2014).

[57] Krämer, M. *et al.* Treatment planning for heavy-ion radiotherapy: physical beam model and dose optimization. *Phys. Med. Biol.* **45** (2000).

[58] Goldhaber, A. Statistical models of fragmentation processes. *Phys. Lett. B* **53** (1974).

[59] Golovkov, M. S., Aleksandrov, D. V., Chulkov, L. V., Kraus, G. & Schardt, D. Fragmentation of 270 AMeV carbon ions in water (1997).

[60] Greiner, D. E., Lindstrom, P. J., Heckman, H. H., Cork, B. & Bieser, F. S. Momentum Distributions of Isotopes Produced by Fragmentation of Relativistic ^{12}C and ^{16}O Projectiles. *Phys. Rev. Lett.* **35** (1975).

[61] Matsufuji, N. *et al.* Spatial fragment distribution from a therapeutic pencil-like carbon beam in water. *Phys. Med. Biol.* **50** (2005).

[62] Chang, K. S., Yin, F. F. & Nie, K. W. The effect of detector size to the broadening of the penumbra–a computer simulated study. *Med. Phys.* **23** (1996).

[63] Bertini, H. W., Santoro, R. T. & Hermann, O. W. Calculated nucleon spectra at several angles from 192-, 500-, 700-, and 900-MeV ^{12}C on ^{56}Fe. *Phys. Rev. C* **14** (1976).

[64] Bellinzona, V. E. *et al.* On the parametrization of lateral dose profiles in proton radiation therapy. *Phys. Med.* **31** (2015).

[65] Tsung, J. W. *et al.* Signal and noise of diamond pixel detectors at high radiation fluences. *J. Instr.* **7**, P09009 (2012).

[66] Pleskac, R. *et al.* The FIRST experiment at GSI. *Nucl. Instrum. Methods Phys. Res. A* **678** (2012).

[67] Gunzert-Marx, K. *et al.* Response of BaF_2 scintillation detector to qausi-monoenergetic fast neutrons in the range of 45 and 198 MeV. *Nucl. Instrum. Methods Phys. Res. A* **536** (2005).

[68] Kurosawa, T. *et al.* Spectral measurements of neutrons, protons, deuterons, tritons produced by 100 MeV/nucleon he ion. *Nucl. Instrum. Methods Phys. Res. A* **430** (1999).

[69] T, K. *et al.* Measurements of secondary neutrons produced from thick targets bombarded by high-energy helium and carbon ions. *Nucl. Sci. Eng. C* **132** (1999).

[70] Heilbronn, L. *et al.* Neutron yields from 155 MeV/nucleon carbon and helium stopping in aluminum. *Nucl. Sci. Eng.* **132** (1999).

[71] Moyers, M. F. EDR-2 film response to charged particles. *Phys. Med. Biol.* **53** (2008).

[72] Van Esch, A. *et al.* The octavius 1500 2D ion chamber array and its associated phantoms: dosimetric characterization of a new prototype. *Med. Phys.* **41** (2014).

[73] Spielberg, B., Krämer, M., Scholz, M. & Kraft, G. Experimental investigations of the response of films to heavy ion irradiation. *Phys. Med. Biol.* **46** (2001).

[74] PTW. Profile measurements at low pulse repetition frequencies. Tech. Rep., PTW-Freiburg.

[75] Craun, R. L. & Smith, D. L. Analysis of response data for several organic scintillators. *Nucl. Instrum. Methods* **80** (1970).

[76] Becchetti, F. D., Thorn, C. E. & Levine, M. J. Response of plastic scintillator detectors to heavy ions, $Z \leq 35$, $E \leq 170$ MeV. *Nucl. Instrum. Methods* **138** (1976).

[77] Kubota, S. *et al.* Response of BaF_2, BaF_2-plastic, and BGO scintillators to neutrons with energies between 15 and 45 MeV. *Nucl. Instrum. Methods Phys. Res. A* **285** (1989).

[78] Wagner, V. *et al.* Detection of relativistic neutrons by BaF_2 scintillators. *Nucl. Instrum. Methods Phys. Res. A* **394** (1997).

Acknowledgements

An important thanks goes to Prof. Marco Durante who gave me the possibility to perform the PhD in the Biophysics group in GSI, offering me a great opportunity for my scientific career. You always appreciated my great enthusiasm and motivation by rewarding me with your trust. I want to also expressed my gratitude to Prof. Thomas Aumann for taking on the co-reference of this work.

I would like to thank Corinna Kausch for the incredible coordination and organization work for the department, the organization of FIAS, that supported my research work, and HGS-HIRe, which do an incredible work for all PhD students allowing a more programmable and structured PhD research environment. Thanks to GSI for exiting and stimulating work atmosphere full of nice and available people. Thanks to the team of HIT, that gave me the opportunity to perform all the experiments of this thesis and especially to Stephan Brons for his support, availability and kindness.

Special thanks to Dieter Schardt, who was always present for me in these years. Your wide experience and continuos interest for my work was of extreme importance for the first interpretation of the results. You are an incredible scientist and an amazing modest person, representing for me an example to imitate and a mentor to follow.

One of the most important “thank you!” goes to my group, Christoph, Uli, Radek and Chiara. People left, people came but me and you Christoph have been always here, as colleagues and as friends. You definitely have the most important contribution on this thesis, such “beautiful” data, as I always say, would not have been presented in this work without your efforts during the experiment and your dedication in following the analysis. Even if Uli was the last “new entry” of the group, he was extremely important for me to reach this goal. In 9 months of working together I learned so many things from and of you, that I was extremely proud to work with such great physicist and person. With you, Radek, we shared a lot of “working moments” and we always supported each other, I always knew I could count on you and I thank you for this. Even though Chiara is not part of the group anymore she always followed my work giving important suggestions and reviewing this thesis very carefully. You were my supervisor and friend in the past and beside the distance of these years you remained the same being always present when support of any kind was needed.

Thanks to the Biophysics group, especially to the persons I worked and interacted more. Thanks to Michael Krämer and Emanuele Scifoni, you gave the whole motivation for my work and you helped me every time I needed to. Thanks to those persons I consider “friends at work”, Anna E., Maria, Olga, Christian G.

Thanks to all my friends the new and the old ones, the ones part of my life in Germany and the ones part of my life in Sicily. These three years have not been always easy but your support, your words, your visits in my office and especially your love, Daria, Enrico, Francesco T., Rebecca, Tugba and Francesco N., was fundamental for me.

Thanks to Rita and Cristina, le mie migliori amiche da sempre che hanno seguito passo passo questo mio viaggio dimostrandomi sempre il loro amore.

A special thanks goes to my love Sebastian...You definitely made my life exceptional during these years leaving me without words to describe it. Every day I learn something new from you, enriching my life with experience. You added a great contribution to this work, offering me all the great skills of the scientist you are.

Vorrei ringraziare la mia splendida famiglia, il modo in cui mi siete stati vicino e mi avete supportato in questa esperienza non ha eguali. Tutto questo non sarebbe mai stato possibile senza di voi e i vostri sacrifici. Grazie al conforto e la forza indescrivibile datomi da mia madre, alla dolcezza regalatami da mio padre, alla comprensione e al coraggio datomi da mia sorella la quale mi ha anche regalato Viola, uno degli amori più grandi al mondo.

Ed infine vorrei anche ringraziare me stessa...Non e' stato facile come credevo, la mia motivazione e volontà sono state messa alla prova diverse volte, la mia autostima e' stata schiacciata, ho cambiato idea su molte cose tra le quali le mie vere priorità, e ho soprattutto testato i limiti di me stessa, i quali sono risultati essere più ‘mortali’ di ciò che pensavo. Nonostante tutto eccomi qua a scrivere i ringraziamenti della mia ennesima tesi, sperando che questa sia l’ultima!

Curriculum Vitae

Marta Rovituso

Personal Informations

Name	Marta Rovituso
Address 1	Viale Stefano Candura n.32, 93100, Caltanissetta (CL), Italy
Address 2	Via S. Bernardino n.30, 38122, Trento (TN), Italy
Telephone 1	0049-176-59691724
E-Mail	m.rovituso@gsi.de,martarovituso@hotmail.it
Date of Birth	June 28th 1986
Place of Birth	Caltanissetta, Italy
Nationality	Italian

Education

2006–2009	**Bachelor in Physics**, *University of Catania*, Catania,Italy, **110/110**.
2009–2012	**Master in Nuclear Physics**, *University of Catania*, Catania,Italy, **110/110 cum laude**.
2013–2016	**PhD in Nuclear Physics**, *Technische Universität Darmastadt*, Darmastadt,Germany, **Magna cum laude**.

BachelorThesis

Title	*The resonant scattering method*
Supervisors	Professor M. Lattuada & Dr. M. Pellegriti

Masters Thesis

Title	*Fragmentation of 200 and 400 MeV/u ^{12}C in bone-like materials*
Supervisors	Professor M. Lattuada & Professor M. Durante & Dr. C. La Tessa

PhD Thesis

Title	*Fragmentation and lateral scattering of 120 and 200 MeV/u ^{4}He ions in water targets*
Supervisors	Professor M. Durante & Professor T. Aumann

Research Fellowships

05/2008-04/2009 **Fellowship**, Laboratori Nazionali del Sud, Catania, Italy.
INFN fellowship to perform research activities for the bachelor degree thesis.

1/08/2011-23/09/2011 **Summer School**, Helmholtzzentrum für Schwerionenforschung, GSI, Darmstadt, Germany.
Participation to the International Student Program at GSI in Darmstadt, Germany

31/01/2012-31/12/2012 **Fellowship**, Helmholtzzentrum für Schwerionenforschung, GSI, Darmstadt, Germany.
GSI fellowship to perform research activities for the master degree thesis.

10/2013-11/2013 **Fellowship**, Brookhaven National Laboratory, BNL, Upton, USA.
Junior research association for research activities at Nasa Space Radiation Laboratory, NSRL.

03/2013-31/05/2016 **Fellowship**, Helmholtzzentrum für Schwerionenforschung, GSI, Darmstadt, Germany.
GSI fellowship to perform research activities for Ph.D.

Laboratories in which the research activities have been performed

- INFN - Laboratori Nazionali del Sud (LNS) - Catania - ITALY
- Helmholtzzentrum für Schwerionenforschung GSI - Darmstadt - Germany
- Heidelberg Ion Therapy Center (HIT) - Heidelberg - Germany
- Brookhaven National Laboratory - Nasa Space Radiation Laboratory (NSRL) - Upton - USA

Communication Skills

04/2014 Poster presentation at the HIC for FAIR review
12/2014 Bioseminar at GSI Helmholtzzentrum für Schwerionenforschung
06/2013 Participation to the shooting "Living in Space" for a french television program

Pubblications

- **"Helium ions for radiotherapy? Physical and biological verifications of a novel treatment modality".** M Krämer, E Scifoni, C Schuy, **M Rovituso**, W Tinganelli, A Maier, R Kaderka, W Kraft-Weyrather, S Brons, T Tessonnier, K Parodi and M Durante. Med. Phys. 43, 1995 (2016)

- **“Prompt-γ production of 220 MeV/u ^{12}C ions interacting with a PMMA target”.** I. Mattei, G. Battistoni, F. Bini, F. Collamati, E. De Lucia, M. Durante, R. Faccini, C. La Tessa, M. Marafini, L. Piersanti, **M. Rovituso**, A. Rucinski, A. Russomando, A. Sarti, C. Schuy, A. Sciubba, E. Solfaroli Camillocci, M. Toppi, G. Traini, M. Vanstalle, C. Voena and V. Patera. Journal of Instrumentation, vol.10, 2015

- **“^{8}Li+α resonant elastic scattering: a tool to study cluster states in ^{12}B”.** D Torresi, L Cosentino, P Descouveont, A Di Pietro, C Ducoin, P Figuera, M Fisichella, M Lattuada, C Maiolino, A Musumarra, M Papa, M G Pellegriti, **M Rovituso**, D Santonocito, G Scalia, V Scuderi, E Strano and M Zadro. Journal of Physics: Conference Series 569 (2014) 012024.

- **“The Inverse Kinematics Thick Target scattering method as a tool to study cluster states in exotic nuclei”.** A Di Pietro, D Torrei, M Zadro, L Cosentino, C Ducoin, P Figuera, M Fisichella, M Lattuada, C Maiolino, A Musumarra, M Papa, MG Pellegriti, **M Rovituso**, D Santonocito, G Scalia, V Scuderi and E Strano. Journal of Physics: Conference Series 366 (2012) 012013.

- **“Alpha structure of ^{12}B studied by elastic scattering of ^{8}Li EXCYT beam on ^{4}He thick target”.** M. G. Pellegriti, D. Torresi, L. Cosentino, A. Di Pietro, C. Ducoin, M. Lattuada, T. Lonnroth, P. Figuera, M. Fisichella, C. Maiolino, A. Musumarra, M. Papa, **M. Rovituso**, V. Scuderi, G. Scalia, D. Santonocito, M. Zadro, Journal of Physics: Conference Series 267 (2011).

- **“Li-alpha CLUSTER STATES IN ^{12}B USING ^{8}Li+ ^{4}He INVERSE KINEMATICS ELASTIC SCATTERING”.**D. Torresi, L. Cosentino, A. Di Pietro, C. Ducoin, P. Figuera, M. Fisichella, M. Lattuada, T. Lonnroth, C. Maiolino, A. Musumarra, M. Papa, M.G. Pellegriti, **M. Rovituso**, D. Santonocito, G. Scalia, V. Scuderi, E. Strano and M. Zadro, International Journal of Modern Physics E, vol. 20, n.4 (2011) 1026-1029.

Reports

- **“Fragmentation of 120 and 200 MeV/u ^{4}He ions in water”**. **M. Rovituso**, C. Schuy, R. Pleskac, D. Izraeli, M. Krämer, M. Durante. GSI, Annual Report 2015

- **“Online monitoring of the Bragg Peak during pig irradiation”**. C. Schuy, **M. Rovituso**, C. Graeff, M. Durante. GSI, Annual Report 2015

- **"Online Bragg Peak monitoring for radiotherapy with ions using pixel sensors"**. **M. Rovituso**, C. La Tessa, C. Schuy, M. Durante. GSI, Annual Report 2014

- **"Online Bragg Peak monitoring for radiotherapy with ions using pixel sensors"**. **M. Rovituso**, C. La Tessa, C. Schuy, M. Durante. GSI, Annual Report 2014

- **"The ROSSINI project at GSI"**. C. Schuy, M. Rovituso, R. Pleskac, C. La Tessa, M. Durante. GSI, Annual Report 2013

- **"Fragmentation of therapeutical carbon ions in bone-like materials".** **M. Rovituso**, C. La Tessa, L. Piersanti, C. Schuy, M. Durante. GSI Annual Report 2013.

- **"Status of the ROSSINI project at GSI"**. C. Schuy, C. La Tessa, **M. Rovituso**, L. Piersanti, E. Tracino, C. Lobascio, M. Durante. GSI Annual Report 2012

- **"Attenuation of a therapeutical carbon beam in bone-like materials".** A. Eichhorn, C. La Tessa, M. Rovituso, and M. Durante. GSI Annual Report 2011.

- **"^{8}Li-α structure in ^{12}B via the resonant scattering method"**. D. Torresi, L. Cosentino, A. Di Pietro, C. Ducoin, M. Lattuada, T. Lonnroth, P. Figuera, M. Fisichella, C. Maiolino, A. Musumarra, M. Papa, M.G. Pellegriti, **M. Rovituso**, V. Scuderi, G. Scalia, D. Santonocito, M. Zadro. LNS Activity Report 2008: 31-33.

Abstracts

- **"Accelerator tests of shielding materials for space travel"**. M. Durante, U. Weber, **M. Rovituso**, C. Schuy, M. Kraemer, C. La Tessa, J.W. Norbury and M. Giraudo

- **"Physical and dosimetrical characterization of ^{4}He, ^{12}C and ^{16}O beams interacting with tissue-like and candidates-shielding materials"**. C. La Tessa, C. Zeitlin, C. Schuy, A. Eichhorn, **M. Rovituso**, A.Rusek, M. Sivertz, and M. Durante, 23rd NASA Workshop.

- **"Interaction of therapeutical ion beams with tissue-like target materials."** C. La Tessa, C. Schuy, **M. Rovituso**, A. Eichhorn, M. Sivertz, M. Durante, A. Rusek, RRS annual meeting.

- **Studying ^{12}B via ^{8}Li-alpha resonant scattering.** D. Torresi, L. Cosentino, A. Di Pietro, C. Ducoin, P. Figuera, M. Fisichella, M. Lattuada, T. Lonnroth, C. Maiolino, A. Musumarra, M. Papa, M.G. Pellegriti, **M. Rovituso**, D. Santonocito, G. Scalia, V. Scuderi, E. Strano and M. Zadro, Proceeding of the 3rd International Conference on Frontiers in Nuclear Structure, Astrophysics and Reactions (FINUSTAR 3), August 23-27, 2010, Rhodos (Greece) accepted for the publication by AIP Conference Proceedings series.